Title
Conjugated Polymer Design and Engineering for Organic Electronics

Author
Woo, Claire Hoi Kar

Publication Date
2011

Conjugated Polymer Design and Engineering for Organic Electronics

By

Claire Hoi Kar Woo

A dissertation submitted in partial satisfaction of the

requirements for the degree of

Doctor of Philosophy

in

Chemical Engineering

in the

Graduate Division

of the

University of California, Berkeley

Committee in Charge:
Professor Jean M. J. Fréchet, Chair
Professor Rachel Segalman
Professor Ting Xu

Spring 2011

Conjugated Polymer Design and Engineering for Organic Electronics

by

Claire Hoi Kar Woo

Abstract

Conjugated Polymer Design and Engineering for Organic Electronics

By

Claire Hoi Kar Woo

Doctor of Philosophy in Chemical Engineering

University of California, Berkeley

Professor Jean M. J. Fréchet, Chair

The molecular structure of a conjugated polymer critically impacts its physical and optoelectronic properties, thus determining its ultimate performance in organic electronic devices. In this work, new polymers and derivatives are designed, synthesized, characterized, and tested in photovoltaic devices. Through device engineering and nanoscale characterization, general structure-function relationships are established to aid the design of the next-generation of high performance polymer semiconductors for organic electronic applications.

Using a prototypical conjugated polymer, the influence of backbone regioregularity is examined and found to highly impact polymer crystallinity, solid state morphology and device stability. The investigation of alternative aromatic units in the backbone also led to new understandings in polymer processability and the development of promising materials for organic photovoltaics.

Besides the backbone structure, the side chain choice of the polymer can significantly affect material properties and device performance as well. In fact, the side chain substitution can influence both the optoelectronic properties and the physical properties of the polymer. A sterically bulky side chain can be used to tune the donor/acceptor separation distance, which in turn determines the charge separation efficiency. The addition of a polar side group increases the dielectric constant of a polymer and improves overall charge separation. Choosing the appropriate solubilizing group can also induce solid state packing of the polymer and considerably enhance device efficiency. Finally, the influence of post-fabrication processing techniques on the crystallinity and charge transport properties of a polymer is highlighted.

TABLE OF CONTENTS

To Dad and Mum,

For their continuous support and unlimited patience

Acknowledgements

My five years in graduate school have been tremendously fun and fulfilling. I have loved living in Berkeley and working in the Fréchet group. This journey would not have been the same without the company and support of my family, friends and colleagues.

First and foremost, I must thank Professor Fréchet for everything that he has taught me. I have greatly admired his high regards for scientific integrity and academic excellence. Perhaps one of the most useful lessons I have learnt is the importance of earning the respect and trust of your peers. Effective teamwork can achieve far more than individuals working independently. Of course, Professor Fréchet is always the experienced chief who has extraordinary skills in managing and encouraging the entire team.

Special mention should be made to my collaborators: Biwu Ma, Mike Toney, Alan Sellinger, and Alberto Salleo. Portions of this work would not have been possible without these individuals' generous support and intellectual contributions.

My teammates and colleagues have made my graduate school experience full of surprises and excitement. I have learnt and gained so much from everyone here that I could never thank them enough. I had the incredible fortune to have been mentored by four great scientists - Kevin Sivula, Bumjoon Kim, Barry Thompson, and David Kavulak - all of whom contributed immensely to putting me on the right track to getting a PhD. My graduate career probably would have been mediocre without Tom Holcombe - a great friend and colleague - whose inexhaustible enthusiasm and continued belief in me encouraged me to reach beyond my limits. I would also like to thank two very special friends and colleagues who have made every day in lab enjoyable. To Claudia Piliego, for being such a strong and generous person. And to Jill Millstone, for the many lessons in life, and whom I believe will go on to do many great things. Also, many thanks to other members in the solar team, both past and present: Paul Armstrong, Pierre Beaujuge, Mark Chen, Tabitha Clem, Jessica Douglas, Olivia Lee, David Unruh, Alan Yiu, and Xiaoyong Zhao. I would also like to say a big thank-you to Cezar Ramiro and Chona de Mesa for all their help and for always keeping spirits high.

I am grateful for all my friends who have been with me during good times and bad. Special thanks to my best friend, Ma'ayan Bresler, for listening and for always putting a smile on my face. My fellow classmate, Albert Keung, for all the exciting adventures we had together and the enlightening discussions on topics ranging from the mundane to the exotic. I would also like to thank Sara Asrat, who has touched my life in a wonderful way.

Lastly, I would like to express my sincere gratitude and love for my family. Without them, I would not be who I am today. Dad and Mum, thank you for everything that you have taught me and for being supportive in many ways. My two beautiful sisters, Cheryl and Jackie, with whom I wish I could spend more time. To my grandmother (Mama), thank you for being generous and understanding always. And to Sivan Eldar, for all the happiness she brings.

Chapter 1

Overview of Organic Electronics – The Operation and Material Design Requirements of Organic Photovoltaics

1.1 Motivations and State of the Technology

Under the threat of global warming and rising oil prices, there is a growing need for carbon-free renewable energy resources. Solar energy is a particularly attractive form of clean and renewable energy, as the total energy of incoming solar irradiation in one hour is equivalent to the world's energy consumption in a year.[1] While silicon solar cells have dominated the commercial solar market, conjugated polymers is a promising alternative material for several reasons.[2-4] The applicability of solution processing techniques under ambient temperature and pressure makes this class of solar cells especially attractive in the search for low-cost methods of harvesting solar energy.[5,6] Another advantage of polymers is the tunability of their electronic and optical properties by molecular design.[7,8] For these reasons, there has been a huge effort to understand the properties of conjugated polymers in order to establish structure-function relationships for designing next-generation electronic materials.

The performance of polymer-based organic photovoltaics (OPVs) has improved dramatically in the past two decades.[9] The current state-of-the-art in polymer photovoltaics is a device consisting of a blend of a light-absorbing conjugated polymer acting as the electron donor and a fullerene derivative acting as the electron acceptor (see Figure 1.2), where the two components form a nanoscale interpenetrating network termed the "bulk heterojunction" (BHJ) morphology.[10,11] Despite recent advances that have achieved 6-7% efficiencies in polymer solar cells,[12-15] much progress is still needed towards large-scale, cost-effective commercial production. Another critical challenge is the stability of polymers, including their thermal stability, air stability, and photo stability.[16-18] This dissertation describes my research efforts in the design, synthesis, and characterization of conjugated materials that are easily processable, stable, and exhibit high performance in OPV devices. Through device engineering and nanoscale characterization techniques, this research has improved fundamental understanding in how molecular structure affects the optical, electronic and physical properties of conjugated polymers. With these new understandings, we can develop design principles for the next-generation of high performance polymer semiconductors.

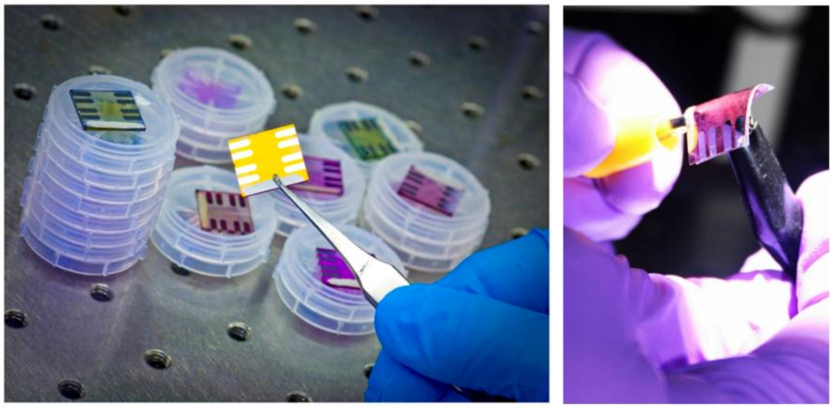

Figure 1.1. (left) Polymer-based organic photovoltaic devices fabricated on glass substrates. (right) Devices fabricated on flexible plastic substrates under simulated sunlight.

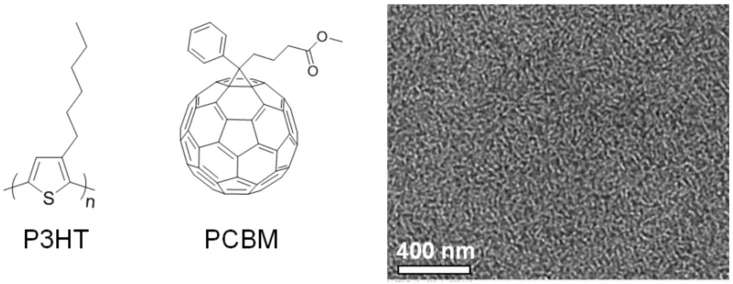

Figure 1.2. (left) The model conjugated polymer P3HT (commonly used as a donor) and popular fullerene derivative PCBM (commonly used as an acceptor). (right) A TEM image of a blend of P3HT and PCBM forming an interpenetrating nanoscale network termed the "bulk heterojunction" (BHJ) morphology.

1.2 The Operation of an Organic Photovoltaic Device

The goal of a solar cell is to convert light (photons) into an electric current (charges). Conventional inorganic (e.g. silicon) solar cells generate free charges upon photoexcitation, and these devices utilize a p-n junction to generate an internal electric field to drive the electrons and holes towards the electrodes.[19] Organic solar cells, on the other hand, are excitonic in nature and operate through an entirely different mechanism.[20,21] The absorption of a photon in organic semiconductors leads to the excitation of an electron from a lower energy level to a higher energy level. However, this excited electron remains coulombically bound to its corresponding hole, leading to the formation of the so-called exciton (i.e. a Coulomb-bound electron-hole pair). The excitonic nature of OPVs is a result of the low dielectric constant of organic semiconductors ($\varepsilon \sim 3\text{-}4$) and the localization of excited states in organic materials due to the non-covalent interactions between neighboring molecules.[22,23] The Coulomb attraction energy of the electron-hole pair is:

$$E_{Coulomb} = \frac{e^2}{4\pi\varepsilon_0\varepsilon R} \qquad (1)$$

where e is the charge of the electron, ε_0 is the permittivity of vacuum, ε is the dielectric constant of the medium, and R is the electron-hole separation distance. For $\varepsilon = 3$ and R = 4 Å, the attraction energy of the exciton is 1200 meV, which is more than an order of magnitude larger than the thermal energy available at room temperature ($k_B T$ at 25°C = 28 meV). The large exciton binding energy of organic semiconductors led to the development of the donor/acceptor heterojunction concept,[21,24] where the energy level offsets between two organic semiconductors provide the thermodynamic driving force for exciton separation. For this reason, a typical organic solar cell consists of an active layer that is made up of two materials, an electron donor and an electron acceptor, which are sandwiched between two electrodes.

Figure 1.3 illustrates the photoinduced charge generation process of an organic solar cell that makes use of the donor/accepter (D/A) heterojunction for exciton separation. This process is generally divided into four main steps, and the energetic transitions associated with each step are also shown in Figure 1.3. The charge generation process can happen via photoexcitation of the donor or the acceptor. For simplicity, we only illustrate the process taking place in the donor material. First, as mentioned above, light absorption in an organic semiconductor leads to the formation of an exciton. Once it is formed, the Coulomb-bound exciton can diffuse by random thermal motion over a distance called the exciton diffusion length. The extremely short lifetime (on the order of nanoseconds) and the localization of the excited state result in a short exciton diffusion length, which is typically ~5-10 nm for most conjugated polymers. The exciton must reach a D/A heterojunction within its lifetime for charge separation to happen. Therefore, for efficient charge generation, the ideal domain sizes of donor phases and acceptor phases in the active layer should be on the order of the exciton diffusion length for a given semiconductor.

The third step of the charge generation process happens when an exciton reaches the D/A interface. At this interface, the LUMO/LUMO offset between the donor and the acceptor makes it energetically favorable for the excited electron to be transferred from the donor to the acceptor. However, in most organic solar cells, electron transfer from the donor to the acceptor does not necessarily lead to free charges. Instead, the electron that has been transferred to the LUMO of the acceptor is still coulombically bound to the hole remaining in the donor, and this intermediate state has been called various names, including "charge-transfer (CT) state", "charge-transfer exciton", and "geminate pair".[25-27] More importantly, the recombination of the electron-hole pair at this intermediate and intermolecular CT state has been found to be one of the major loss mechanisms in OPVs.[28-31] There are other possible pathways for energy loss during the process of charge separation. Figure 1.4 shows the energy level diagram of the energy states involved in charge separation and the potential loss mechanisms in the process. Although significant progress has been made in the past few years, our understanding of the dynamics of these interconnected energy pathways and the physics of the overall charge separation process remains incomplete.[21] Many questions are yet to be answered: What controls the separation and decay dynamics of the CT state? What determines whether charge separation originates from a hot CT state (CT*) or the ground state CT state (CT_1)? How does CT state separation compete with intersystem crossing to form triplet states? How do interfacial molecular interactions of the donor and the acceptor affect the thermodynamics and kinetics of the charge separation process?

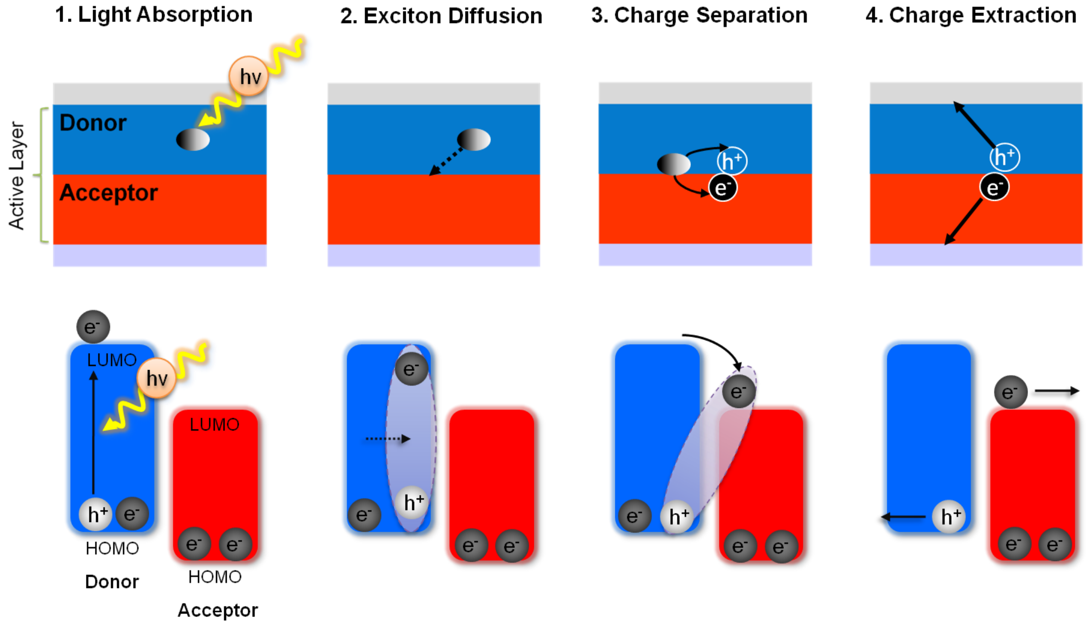

Figure 1.3. A schematic of the four-step operation of an organic solar cell and the corresponding energetic transitions of each step are illustrated below. 1. Light absorption, leading to the excitation of an electron and the formation of an exciton. 2. Exciton diffusion to the donor/acceptor interface. 3. Separation of the exciton into a free hole and a free electron at the donor/acceptor interface. 4. Charge extraction to the respective electrodes.

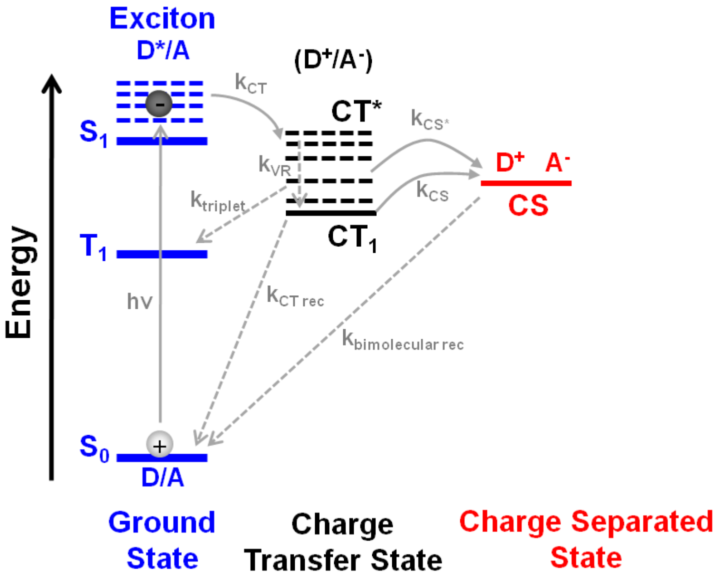

Figure 1.4. Energy level diagram showing some of the main processes and energy states involved in charge separation. Solid arrows illustrate the desirable transitions: *hv* is the photoexcitation from ground state (S_0) to singlet exciton (S_1); k_{CT} is exciton dissociation to form either a hot charge transfer state (CT*) or a ground-state charge transfer state (CT_1); k_{CS*} is the dissociation of a hot CT state into the charge separated (CS) state; and k_{CS} is the dissociation of a ground state CT state into the CS state. Dashed arrows show potential energy loss pathways: k_{VR} is the vibrational relaxation of a hot CT state to lower energy CT states; $k_{triplet}$ refers to intersystem crossing from a CT state to the triplet state (T_1); $k_{CT\ rec}$ is the recombination of the CT state back to the ground state; $k_{bimolecular\ rec}$ is the bimolecular recombination of the hole and electron in the CS state.

Once the CT state has successfully separated into free charges, the last step in the operation of an OPV device is charge extraction. The hole must travel through the donor while the electron travels through the acceptor (step 4 in Figure 1.3). Charge transport in organic semiconductors can proceed either through a hopping mechanism (from one localized state to another) or through band-like conduction through conjugated regions. The energy level offset between the donor and the acceptor creates an internal electric field that helps to drive free charges towards the respective electrodes. Another more significant driving force for the movement of free charges is the chemical potential gradient that is a result of the high concentration of localized holes and electrons formed at the donor/acceptor interface. However, charge extraction in these devices is also heavily dependent on the charge mobility of the organic semiconductors.[32] The charge mobility of the active layer is determined by many factors, including the intrinsic mobility of the semiconductors used, their solid state packing, the 3D morphology of the active layer, and impurities.

The overall power conversion efficiency (PCE) of an organic solar cell is determined by the efficiency of each of the four steps in the charge generation process. This dependence is illustrated by equation (2). Each step is in turn affected by the choice of organic semiconducting materials, the processing of these materials, the device architecture, and the morphology of the active layer.

$$PCE = \eta = \eta_{absorption} \times \eta_{diffusion} \times \eta_{separation} \times \eta_{transport} \qquad (2)$$

1.3 Device Architecture and the Importance of Morphology

The previous section described the operation of an OPV device in a simple bilayer architecture where the donor and the acceptor are separate layers sandwiched between two electrodes (Figure 1.5a). However, bilayer heterojunctions are limited in terms of their maximum performance because of two reasons.[33,34] First, the short exciton diffusion length (~5-10 nm) limits the thickness of each layer as excitons that are formed far away from the D/A interface will not reach the interface within its lifetime and thus will be wasted. A thin active layer reduces the number of photons that can be absorbed. Second, there is only a limited amount of D/A interfacial area for charge separation. To circumvent this problem, the bulk heterojunction (BHJ) architecture is commonly used. The concept was first demonstrated by Yu et al in 1995,[35] and Figure 1.5b illustrates a schematic of the BHJ morphology where the donor and the acceptor materials form an intimate mixture. Typically, this morphology is achieved by mixing the donor and the acceptor in a single solution and then kinetically trapping a nanoscale separated morphology during film casting.[5,36] Ideally, the domain sizes should be on the order of the exciton diffusion length so that all the excitons can reach a D/A interface within its lifetime. In addition, the donor and acceptor should form an interpenetrating network so that there are pathways for efficient charge extraction. Figure 1.2 shows a TEM image of the BHJ morphology with nanoscale phase separation between the two components, P3HT and PCBM, which are a donor/acceptor combination that has shown efficient performance up to 5%.[37] Unfortunately, this ideal nanoscale phase separated and interpenetrating morphology is not always attainable with different material combinations. Moreover, the BHJ morphology is often not thermally stable and may evolve over time as the donor and acceptor molecules phase separate from each other, leading to decreasing D/A interfacial area and device degradation.[38-40] A lot of work has been done in the past decade on how to use processing techniques to manipulate as well as stabilize the BHJ morphology of different donor/acceptor combinations.[41-47]

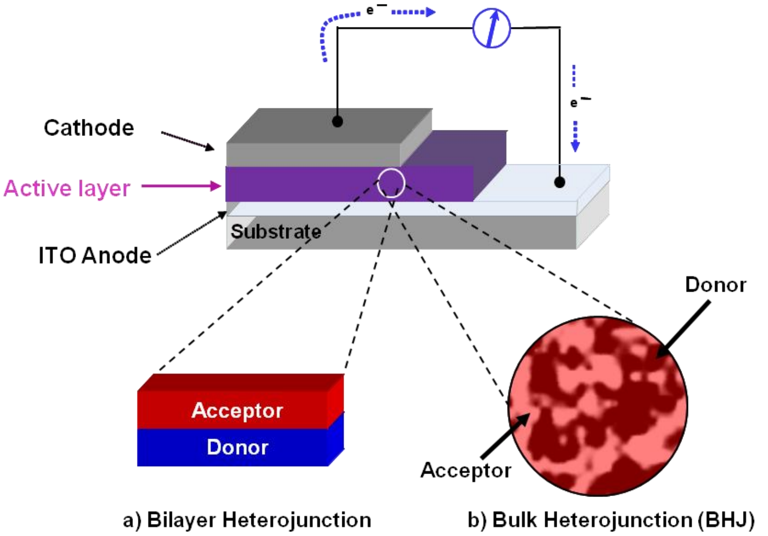

Figure 1.5. Two common types of device architectures used in OPVs. a) Bilayer heterojunction where the donor and acceptor are deposited sequentially to form separate layers. b) Bulk heterojunction (BHJ) where the donor and acceptor are an intimate mixture that forms interpenetrated, percolating pathways for charge extraction.

1.4 Device Testing and Characterization

To test the performance of a solar cell, the device is placed under simulated sunlight and the current density (J) is measured as a function of applied bias (V). The standard spectrum used for device testing is the Air Mass 1.5 global (AM 1.5G) spectrum, which is the incoming solar flux that has interacted with different air masses.[48] The AM 1.5G spectrum, as shown in Figure 1.6, represents the amount of incoming photons at an incidence angle of 48° from the normal and has an overall intensity of 100 mW/cm^2.

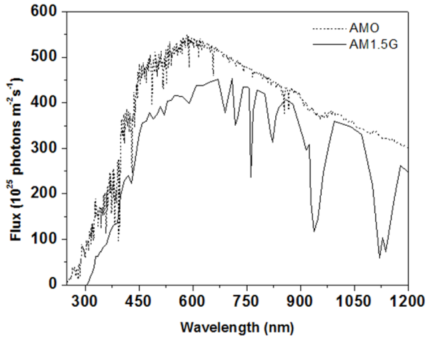

Figure 1.6. The standard AM 1.5G spectrum is used for testing solar cells under simulated sunlight. The AM0 spectrum is also shown for reference.

A typical J-V curve output of a solar cell is shown in Figure 1.7. There are a few main parameters of interest as highlighted in the figure. The open-circuit voltage (V_{oc}) is where the light current (J_{light}) intersects the x-axis and represents the maximum load that can be applied to the solar cell to get work. The current density at zero bias is called the short-circuit current (J_{sc}) and represents the current generated by the device without any externally applied bias. The maximum power point (max. power = V_{mpp} x J_{mpp}) lies somewhere along the J-V curve and is the point where the power conversion efficiency is determined. The curving shape of the J-V plot is caused by non-idealities and losses in the device and is usually represented by the fill-factor (FF). FF is defined as the ratio between the maximum power point (V_{mpp} x J_{mpp}) and the absolute power point (V_{oc} x J_{sc}). The power conversion efficiency (PCE or η) at a given incident light intensity is often calculated from the V_{oc}, J_{sc}, and FF using equation (3).

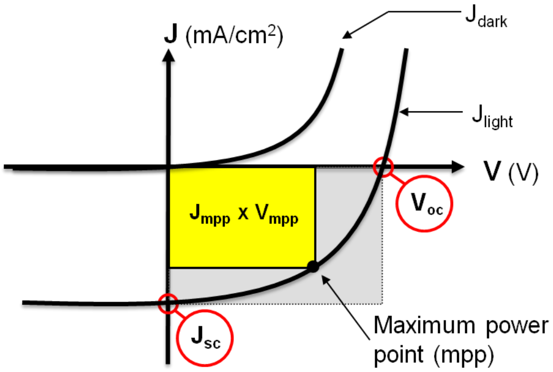

Figure 1.7. Typical J-V curve of a solar cell under dark (J_{dark}) and under illumination (J_{light}). The main device parameters of interest are open-circuit voltage (V_{oc}), short-circuit current density (J_{sc}), and the maximum power point (V_{mpp}, J_{mpp}).

$$\eta = \frac{P_{out}}{P_{in}} = \frac{V_{MPP} \times J_{MPP}}{P_{in}} = \frac{V_{OC} \times J_{SC} \times FF}{P_{in}}, \quad FF = \frac{V_{MPP} \times J_{MPP}}{V_{OC} \times J_{SC}} \qquad (3)$$

1.5 Conjugated Polymer Design

This dissertation mainly focuses on the design of conjugated polymers for use as electron donors, but the same principles apply to polymeric acceptors. For OPV applications, both the optoelectronic properties and the structural properties (e.g. crystallinity, solubility, viscosity, miscibility etc.) of the conjugated polymers are equally important.[8,49,50] On the one hand, the ideal polymer should have the appropriate energy levels for charge separation with the acceptor of choice, a small optical band gap for abundant light absorption, and a high hole mobility for efficient charge transport. On the other hand, the polymer should be easily processable by organic solvents and miscible with the acceptor for the realization of nanoscale BHJ morphology. Although there have been a lot of efforts centered upon modifying the molecular structure of conjugated polymers to obtain favorable properties, the design process is complicated because changes in the molecular structure tend to affect both the optoelectronic properties and the structural properties of the polymer.[7,51,52] Moreover, there is still a lack of understanding in how the molecular structure of the polymer affects the final OPV device performance. Despite the development of several important design rules for OPV materials, current models still cannot predict the performance of a conjugated polymer without the actual fabrication and testing of the device.[7,8,10] Therefore, establishing structure-function relationships for conjugated polymers is critical for the design of next-generation high performance materials for OPVs. The following Chapters describe several studies in correlating the molecular structure of conjugated polymers to their optoelectronic and structural properties and ultimately their device performance. Here, we will provide a brief introduction to the principles of conjugated polymer design.

To effectively design conjugated polymers for semiconductor applications, we have to first understand their electronic band structure and band gap formation. The band structure of conjugated polymers can be explained by molecular orbital theory.[53] When two or more aromatic units (e.g. thiophene rings) couple with each other, hybridization of their HOMO (π) and LUMO (π^*) levels lead to a decrease in the energy between the two states (Figure 1.8). Orbital hybridization allows the π electrons in the system to be delocalized over all the aromatic rings that are in conjugation. The energy spacing between the HOMO and the LUMO level decreases upon each ring addition, until full delocalization of the π electrons is achieved. At this point, the discrete energy levels can be approximated as continuous bands similar to that of the conduction band and the valence band in inorganic semiconductors (Figure 1.8). When additional rings to the polymer chain do not reduce the energy gap further, it means the polymer has reached its conjugation length. The conjugation length varies for different polymers, but it is typically 5-20 repeat units. The energy gap between the HOMO and LUMO levels, called the band gap E_g, determines the optical absorption of the polymer.[54] Since there are no electronic states in between the HOMO and LUMO levels, E_g represents the minimum energy that a photon must have in order to promote an electron from the HOMO to the LUMO of a conjugated polymer.

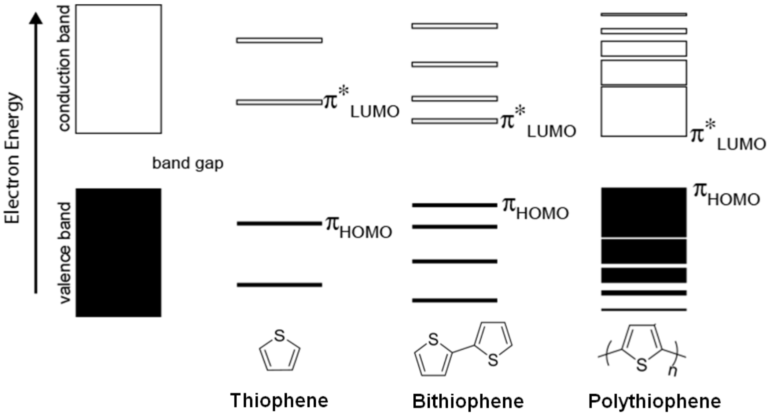

Figure 1.8. (left) The band structure of an intrinsic inorganic semiconductor. (right) The molecular orbital hybridization process during the polymerization of the conjugated backbone. Each additional ring reduces the energy gap between the HOMO and LUMO levels, until eventually the energy levels can be approximated as continuous band structures and a conjugated polymer is formed.

In addition to energy levels and band gap, another important electronic property is the charger carrier mobility of the polymer. Although current models still cannot completely explain or predict charge transport in organic semiconductors, it is clear that charge mobility is a complex function of molecular structure, molecular geometry, system environment, intermolecular distance, and molecular packing.[32] Figure 1.9a shows the two main mechanisms for charge transport in a conjugated material: 1. band-like conduction through the conjugated backbone or 2. hopping from chain to chain through the π-stacking network, which is formed by intermolecular overlapping of the π-orbitals of neighboring polymer chains. Clearly, both mechanisms depend heavily on the solid state structure of the conjugated polymer. More specifically, highly ordered and crystalline polymer domains are favorable for charge mobility. Besides crystallinity, another consideration is molecular geometry. Figure 1.9b shows the solid state packing motif of P3HT thin film on a substrate. P3HT usually adopts an edge-on orientation where the polymer chains are oriented perpendicular to the substrate and the π-stacking direction (axis c) is parallel to the substrate. In this geometry, charges can move rather quickly in the direction parallel to the substrate. However, this is in fact not ideal for OPV devices, which require charge transport in the vertical direction and thus favoring a face-on orientation.

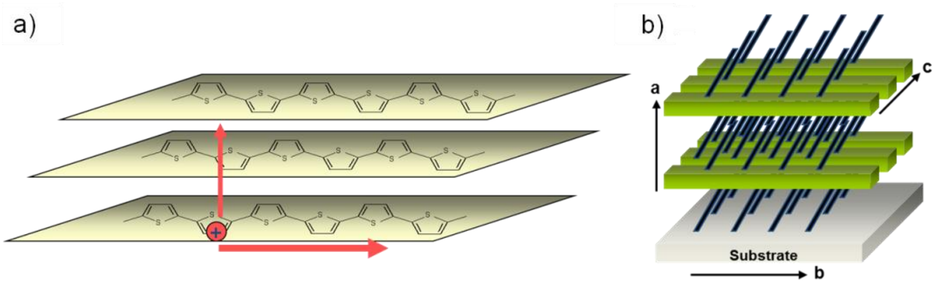

Figure 1.9. a) Two mechanisms of charge transport in a conjugated polymer: 1. band-like conduction through the conjugated backbone, 2. hopping from one chain to another through the π-stacking network formed by intermolecular π-orbital overlap. b) The solid state packing motif of a P3HT thin film where the lamellar spacing (a) is perpendicular to the substrate and the π-stacking distance (c) is parallel to the substrate.

Although charge transport is generally superior in more ordered materials, a higher degree of crystallinity is not necessary favorable for OPVs. Chapter 2 demonstrates an example where lowering the driving force for crystallization of the polymer is favorable. In this case, we studied P3HTs with different regioregularities, and we discovered that polymer samples with lower regioregularities exhibit superior thermal stability in bulk heterojunction devices with a fullerene acceptor. The enhanced thermal stability of the device is caused by a lower driving force for polymer crystallization in the less regioregular polymer samples, leading to increased miscibility with the acceptor.

Besides the primary structure of the polymer backbone, the side chain choice can also significantly influence the structural properties and device performance of a polymer. Chapter 3 outlines a comparative study between the model polymer P3HT and a structurally-similar polythiophene, poly[3-(4-n-octyl)-phenylthiophene] (POPT). We found that the addition of a phenyl ring on the side chain of POPT can facilitate charge separation. The phenyl ring on POPT prefers to twist out-of-plane from the conjugated backbone, resulting in a larger donor/acceptor (D/A) separation distance due to steric hindrance at the interface. This larger D/A separation distance leads to a destabilized charge transfer state during the charge separation process, thus lowing the energetic barrier for complete charge dissociation into free charges. This study is the first example of using sterics to control D/A separation distance for charge separation.

Side chain can also be used to tune the electronics of the system. Chapter 4 describes the use of a polar side group to modify the dielectric constant of P3HT. As discussed in Section 1.2, the low dielectric constant of organic semiconductors is the major factor contributing to the excitonic nature of OPVs. If we can increase the dielectric constant of a conjugated polymer such that it mimics an inorganic semiconductor, then we can lower the exciton binding energy and improve overall charge separation. A higher dielectric constant can also stabilize free charges and reduce losses through bimolecular recombination.

Although P3HT is an attractive polymer for OPV applications, its non-ideal optical band-gaps of ~1.9 eV does not efficiently blanket the solar spectrum. To achieve even higher solar cell efficiencies, recent research efforts have focused on the development of low band gap donor polymers with broad absorption spectra.[50,55,56] Interestingly though, all high performance polymers reported so far rely on thiophene-based aromatic units.[13,15,46,57-60] On the other hand, only a limited number of studies have examined furan, which is a very similar aromatic unit to thiophene.[61,62] Chapter 5 explores the use of furan in conjugated polymers and their OPV device performance. This study on furan is also an interesting example where modifying the backbone structure affects the microstructural order and solubility of the polymer.

In parallel to the development of high performance polymer semiconductors, there are research efforts towards realizing small molecule OPVs.[63] However, the efficiencies of solution processed OPVs using small molecules have lagged behind the performance level of polymer-based devices. Chapter 6 investigates the use of a solution processable small molecule, Subnaphthalocyanine, that has shown promising OPV performance.

Finally, in Chapter 7, we describe a fundamental study on the correlation between charge transport and crystallinity in a photo-crosslinkable P3HT derivative. Using newly developed X-ray diffraction analysis techniques, we were able to quantitatively compare the degrees of crystallinity of polymer thin films. This study confirms that a higher degree of crystallinity is beneficial for charge transport. Furthermore, we explored the effect of crosslinking on the charge mobility and solid state order of a conjugated polymer.

1.6 References

(1) Morton, O. *Nature* **2006**, *443*, 19-22.
(2) Green, M. A. *Prog. Photovolt.* **2009**, *17*, 183-189.
(3) Swanson, R. M. *Prog. Photovolt: Res. Appl.* **2006**, *14*, 443-453.
(4) Green, M. A. *Solar Energy* **2004**, *76*, 3-8.
(5) Peet, J.; Senatore, M. L.; Heeger, A. J.; Bazan, G. C. *Adv.Mater.* **2009**, *21*, 1521-1527.
(6) Arias, A. C.; MacKenzie, J. D.; McCulloch, I.; Rivnay, J.; Salleo, A. *Chem. Rev.* **2010**, *110*, 3-24.
(7) Bredas, J. L.; Norton, J. E.; Cornil, J.; Coropceanu, V. *Acct. Chem. Res.* **2009**, *42*, 1691-1699.
(8) Scharber, M. C.; Wuhlbacher, D.; Koppe, M.; Denk, P.; Waldauf, C.; Heeger, A. J.; Brabec, C. L. *Adv. Mater.* **2006**, *18*, 789-794.
(9) Spanggaard, H.; Krebs, F. C. *Sol. Energy Mater.& Sol. Cells* **2004**, *83*, 125-146.
(10) Dennler, G.; Scharber, M. C.; Brabec, C. J. *Adv. Mater.* **2009**, *21*, 1323-1338.
(11) Thompson, B. C.; Fréchet, J. M. J. *Angew. Chem., Int. Ed.* **2008**, *47*, 58-77.
(12) Chen, H. Y.; Hou, J. H.; Zhang, S. Q.; Liang, Y. Y.; Yang, G. W.; Yang, Y.; Yu, L. P.; Wu, Y.; Li, G. *Nat. Photon.* **2009**, *3*, 649-653.
(13) Piliego, C.; Holcombe, T. W.; Douglas, J. D.; Woo, C. H.; Beaujuge, P. M.; Fréchet, J. M. J. *J. Am. Chem. Soc.* **2010**, *132*, 7597-7597.
(14) Price, S. C.; Stuart, A. C.; Yang, L.; Zhou, H.; You, W. *J.Am.Chem.Soc.* **2011**, *133*, 4625-4631.
(15) Qin, R.; Li, W.; Li, C.; Du, C.; Veit, C.; Schleiermacher, H. F.; Andersson, M.; Bo, Z.; Liu, Z.; Inganas, O.; e; Wuerfel, U.; Zhang, F. *J. Am. Chem. Soc.* **2009**, *131*, 14612-14613.
(16) Manceau, M.; Bundgaard, E.; Carle, J. E.; Hagemann, O.; Helgesen, M.; Sondergaard, R.; Jorgensen, M.; Krebs, F. C. *J. Mater. Chem.* **2011**, *21*, 4132-4141.
(17) Jorgensen, M.; Norrman, K.; Krebs, F. C. *Sol. Energy Mater.& Sol. Cells* **2008**, *92*, 686-714.
(18) Krebs, F. C.; Norrman, K. *Prog. Photovolt.* **2007**, *15*, 697-712.
(19) Green, M. A. *Solar Cells: Operating Principles, Technology, and System Applications*; University of New South Wales: 1986.
(20) Blom, P. W. M.; Mihailetchi, V. D.; Koster, L. J. A.; Markov, D. E. *Adv. Mater.* **2007**, *19*, 1551-1566.
(21) Clarke, T. M.; Durrant, J. R. *Chem. Rev.* **2010**, *110*, 6736-6767.
(22) Gregg, B. A. *J. Phys. Chem. B* **2003**, *107*, 4688-4698.
(23) Gregg, B. A.; Hanna, M. C. *J. Appl. Phys.* **2003**, *93*, 3605-3614.
(24) Tang, C. W. *Appl. Phys. Lett.* **1986**, *48*, 183-185.
(25) Zhu, X. Y.; Yang, Q.; Muntwiler, M. *Acct. Chem. Res.* **2009**, *42*, 1779-1787.
(26) Loi, M. A.; Toffanin, S.; Muccini, M.; Forster, M.; Scherf, U.; Scharber, M. *Adv. Funct. Mater.* **2007**, *17*, 2111-2116.
(27) Muntwiler, M.; Yang, Q.; Tisdale, W. A.; Zhu, X. Y. *Phys. Rev. Lett.* **2008**, *101*, 196403.
(28) Lenes, M.; Morana, M.; Brabec, C. J.; Blom, P. W. M. *Adv. Funct. Mater.* **2009**, *19*, 1106-1111.
(29) Hwang, I. W.; Moses, D.; Heeger, A. J. *J. Phys. Chem. C* **2008**, *112*, 4350-4354.

(30) Ohkita, H.; Cook, S.; Astuti, Y.; Duffy, W.; Tierney, S.; Zhang, W.; Heeney, M.; McCulloch, I.; Nelson, J.; Bradley, D. D. C.; Durrant, J. R. *J. Am. Chem. Soc.* **2008**, *130*, 3030-3042.
(31) Zhou, Y.; Tvingstedt, K.; Zhang, F. L.; Du, C. X.; Ni, W. X.; Andersson, M. R.; Inganas, O. *Adv. Funct. Mater.* **2009**, *19*, 3293-3299.
(32) Coropceanu, V.; Cornil, J.; da Silva, D. A.; Olivier, Y.; Silbey, R.; Bredas, J. L. *Chem. Rev.* **2007**, *107*, 926-952.
(33) Coakley, K. M.; McGehee, M. D. *Chem. Mater.* **2004**, *16*, 4533-4542.
(34) Hoppe, H.; Sariciftci, N. S. *J. Mater. Res.* **2004**, *19*, 1924-1945.
(35) Yu, G.; Gao, J.; Hummelen, J. C.; Wudl, F.; Heeger, A. J. *Science* **1995**, *270*, 1789-1791.
(36) Yang, X. N.; Loos, J.; Veenstra, S. C.; Verhees, W. J. H.; Wienk, M. M.; Kroon, J. M.; Michels, M. A. J.; Janssen, R. A. J. *Nano Lett.* **2005**, *5*, 579-583.
(37) Ma, W. L.; Yang, C. Y.; Gong, X.; Lee, K.; Heeger, A. J. *Adv. Funct. Mater.* **2005**, *15*, 1617-1622.
(38) Nguyen, L. H.; Hoppe, H.; Erb, T.; Gunes, S.; Gobsch, G.; Sariciftci, N. S. *Adv. Funct. Mater.* **2007**, *17*, 1071-1078.
(39) Sivula, K.; Luscombe, C. K.; Thompson, B. C.; Fréchet, J. M. J. *J. Am. Chem. Soc.* **2006**, *128*, 13988-13989.
(40) Verploegen, E.; Mondal, R.; Bettinger, C. J.; Sok, S.; Toney, M. F.; Bao, Z. A. *Adv. Funct. Mater.* **2010**, *20*, 3519-3529.
(41) Jo, J.; Kim, S. S.; Na, S. I.; Yu, B. K.; Kim, D. Y. *Adv. Funct. Mater.* **2009**, *19*, 866-874.
(42) Chen, L. M.; Hong, Z. R.; Li, G.; Yang, Y. *Adv. Mater.* **2009**, *21*, 1434-1449.
(43) Rajaram, S.; Armstrong, P. B.; Kim, B. J.; Fréchet, J. M. J. *Chem. Mater.* **2009**, *21*, 1775-1777.
(44) Campbell, A. R.; Hodgkiss, J. M.; Westenhoff, S.; Howard, I. A.; Marsh, R. A.; McNeill, C. R.; Friend, R. H.; Greenham, N. C. *Nano Lett.* **2008**, *8*, 3942-3947.
(45) Li, G.; Shrotriya, V.; Huang, J. S.; Yao, Y.; Moriarty, T.; Emery, K.; Yang, Y. *Nat. Mater.* **2005**, *4*, 864-868.
(46) Peet, J.; Kim, J. Y.; Coates, N. E.; Ma, W. L.; Moses, D.; Heeger, A. J.; Bazan, G. C. *Nat. Mater.* **2007**, *6*, 497-500.
(47) Clarke, T. M.; Ballantyne, A. M.; Nelson, J.; Bradley, D. D. C.; Durrant, J. R. *Adv. Funct.Mater.* **2008**, *18*, 4029-4035.
(48) National Renewable Energy Laboratory. Reference Solar Spectral Irradiance: Air Mass 1.5.http://rredc.nrel.gov/solar/spectra/am1.5/.
(49) Boudreault, P. L. T.; Najari, A.; Leclerc, M. *Chem. Mater.* **2011**, *23*, 456-469.
(50) Chen, J. W.; Cao, Y. *Acct. Chem. Res.* **2009**, *42*, 1709-1718.
(51) Heremans, P.; Cheyns, D.; Rand, B. P. *Acct. Chem. Res.* **2009**, *42*, 1740-1747.
(52) Zhou, H. X.; Yang, L. Q.; Liu, S. B.; You, W. *Macromolecules* **2010**, *43*, 10390-10396.
(53) Nalwa, H. S. *Handbook of Organic Conductive Molecules and Polymers, Volume 2, Conductive Polymers: Synthesis and Electrical Properties*; Wiley: 1996.
(54) Turro, N. J. *Modern Molecular Photochemistry*; University Science Books: 1991.
(55) Cheng, Y. J.; Yang, S. H.; Hsu, C. S. *Chem. Rev.* **2009**, *109*, 5868-5923.
(56) Roncali, J. *Macromol. Rapid Comm.* **2007**, *28*, 1761-1775.
(57) Zou, Y.; Najari, A.; Berrouard, P.; Beaupre, S.; Reda Aich, B.; Tao, Y.; Leclerc, M. *J. Am. Chem. Soc.* **2010**, *132*, 5330-5331.

(58) Park, S. H.; Roy, A.; Beaupre, S.; Cho, S.; Coates, N.; Moon, J. S.; Moses, D.; Leclerc, M.; Lee, K.; Heeger, A. J. *Nat. Photon.* **2009**, *3*, 297-2U5.

(59) Liang, Y.; Feng, D.; Wu, Y.; Tsai, S. T.; Li, G.; Ray, C.; Yu, L. *J. Am. Chem. Soc.* **2009**, *131*, 7792-7799.

(60) Hou, J.; Chen, H. Y.; Zhang, S.; Li, G.; Yang, Y. *J. Am. Chem. Soc.* **2008**, *130*, 16144-16145.

(61) Bunz, U. H. F. *Angew. Chem., Int. Ed.* **2010**, *49*, 5037-5040.

(62) Yamamoto, T.; Zhou, Z. H.; Kanbara, T.; Shimura, M.; Kizu, K.; Maruyama, T.; Nakamura, Y.; Fukuda, T.; Lee, B. L.; Ooba, N.; Tomaru, S.; Kurihara, T.; Kaino, T.; Kubota, K.; Sasaki, S. *J. Am. Chem. Soc.* **1996**, *118*, 10389-10399.

(63) Lloyd, M. T.; Anthony, J. E.; Malliaras, G. G. *Materials Today* **2007**, *10*, 34-41.

Chapter 2

The Influence of Polymer Regioregularity on Bulk Heterojunction Solar Cell Performance[1]

Abstract

The comparison of three samples of poly(3-hexylthiophene) (P3HT) with regioregularities of 86%, 90%, and 96% is used to elucidate the effect of regioregularity on polymer-fullerene bulk heterojunction (BHJ) solar cell performance. It is observed that P3HTs with lower regioregularities are capable of generating BHJ solar cells that exhibit superior thermal stability. The enhanced thermal stability of the active layer blend is attributed to a lower driving force for polymer crystallization in the less regioregular polymer samples, which is supported by two-dimensional grazing incidence X-ray scattering (2D-GIXS) and differential scanning calorimetry (DSC) measurements. Furthermore, it is demonstrated that all three polymer samples are capable of generating solar cells with equivalent peak efficiencies of ~4% in blends with fullerene derivative [6,6]-phenyl-C61-butyric acid methyl ester (PCBM). While it may be non-intuitive that polymers with lower regioregularity can exhibit high efficiency, it is observed that the charge carrier mobility of the three polymers is of the same order of magnitude (10^{-4} cm^2 V^{-1} s^{-1}) when measured from the space charge limited current (SCLC), suggesting that highly regioregular and crystalline polythiophenes are not required in order to effectively transport charges in polymer solar cells. These results suggest a design principle for semicrystalline conjugated polymers in BHJ solar cells with fullerenes where crystallization-driven phase separation can be dramatically suppressed via the introduction of a controlled amount of disorder into the polymer backbone.

---

[1] Reproduced in part with permission from , J. M. J. *Journal of the American Chemical Society* **2008**, *130*, 16324-16329. Copyright 2008 American Chemical Society.

2.1 Introduction

Polymer-fullerene composite solar cells (bulk heterojunction solar cells) define the state-of-the-art in organic photovoltaics (OPVs), with reported efficiencies as high as ~5%.[1-4] The applicability of solution processing techniques under ambient temperature and pressure make this class of solar cell especially attractive in the search for low-cost methods of harvesting solar energy.[5] While several new high performing polymer-fullerene combinations have been recently reported,[6,7] the combination of poly(3-hexylthiophene) (P3HT) and [6,6]-phenyl-C_{61}-butyric acid methyl ester (PCBM) still gives among the highest reported power conversion efficiencies (PCEs).[3,4] This is despite the non-ideal band gap of P3HT (~1.9 eV), preventing effective overlap with the solar spectrum, which peaks at ~1.8 eV. Numerous polymers have been synthesized that exhibit more optimal band gaps and blanket the solar spectrum more effectively,[8,9] but almost none have exceeded the performance of P3HT.[6] This can be attributed to an incomplete set of design principles for an ideal donor polymer for fullerene-composite solar cells, which is currently, exclusively based on the electronic interaction of the polymer and fullerene[1,8,10] and ignores the features of the polymer primary structure that influence the formation of active layers with bicontinuous and thermally stable morphologies.

Towards this end, P3HT is targeted as a model semicrystalline polymer from which general relationships between primary structure and function can be extrapolated. The key variables of polymer primary structure in P3HT are molecular weight, polydispersity, and regioregularity (RR). In each case, efforts toward elucidating the effect of each individual variable on photovoltaic performance have been pursued.[11-14] The developing picture suggests that high molecular weight (M_n >20,000 g/mol), broad polydispersity (PDI), and high RR (>95%) are optimal for solar cell performance as can be supported via both observed increases in efficiency when these parameters are satisfied and by extrapolating from structure-function relationships observed in pristine samples of P3HT.[15-18]

However, all of these conclusions come with a caveat. First, while high molecular weight has been shown to improve charge carrier mobility and optical properties in pristine, highly RR P3HT films, solar cells using P3HT of significantly lower molecular weight (~11,000 g/mol) have been reported to give efficiencies over 4% under optimized processing conditions.[13] Second, a systematic study on the effect of polydispersity of P3HT has not been reported, although it does appear that a broad mix of high and low molecular weight P3HT in a given sample improves the performance of P3HT-PCBM composite solar cells.[12] Finally, the only systematic study of the effect of P3HT RR, which points to increasing efficiency with increasing RR, is based on a comparison of devices for which the processing conditions had not been optimized.[13] Based on the enormous effects that are known for variations in solvent,[19,20] blend ratio,[21,22] spin speed,[20,23] annealing conditions,[4,24,25] and electrode structure,[26,27] such unoptimized results are not necessarily definitive. The study by Kim *et al*[13] examines the range of RR from 90.7-95.4%, showing that samples in the 90.7-93.0% range have efficiencies of under 2%, which is lower than the 4-5% efficiencies reported in the literature using P3HT from Rieke Metals (RR ~92%).[3,28] It has also been shown that a copolymer analogue of P3HT with an effective RR of 91% was capable of producing solar cells with 4.5% power conversion efficiencies.[28] It is therefore clear that the definitive effect of P3HT RR on fullerene-composite solar cells is not yet known.

Here we examine three samples of P3HT of similar molecular weight and PDI polymerized by the same polymerization method, in which the RR is varied from 86-96%. This RR range is selected in order to look at a highly RR P3HT (96%), a sample with similar RR to Rieke P3HT (90%), and a sample with a significantly lower RR than has been reported in most P3HT-PCBM solar cells (86%). The lowest RR value was attained via a copolymerization of 2-bromo-3-hexylthiophene and 5-bromo-3,3'-dihexyl-2,2'-bithiophene (see Experimental section). Solar cell performance and long term thermal stability are examined within the context of variations in the fundamental properties of the polymers induced via changes to the primary structure in the form of non head-to-tail "defect" linkages.

2.2 Results

2.2.1 Solar Cell Performance

The performance of each polymer was independently optimized according to annealing conditions while the polymer:PCBM blend ratio was kept constant at 55:45 by weight and the devices all had similar thicknesses (~100nm). Figure 2.1 shows the *I-V* characteristics of the most efficient P3HT:PCBM bulk heterojunction devices made from 86% RR, 90% RR, and 96% RR P3HT, which achieved 3.9%, 3.8%, and 3.8% peak PCE respectively at AM 1.5G with an intensity of 100mW cm^{-2}. First, it is noteworthy that P3HT with as low as 86%RR can still achieve close to 4% PCE. A second observation is that the optimized annealing time is different for the three polymers. At an annealing temperature of 150^{o}C, the device with 96% RR P3HT requires the shortest annealing time of 30 min to reach the highest efficiency whereas the devices with 90%RR P3HT and 86%RR P3HT require longer annealing times of 60 min and 120 min respectively. The slightly lower J_{sc} in the device with 90%RR may be due to the lower molecular weight of the polymer which may influence the parameters of device performance,[29.30] but the high fill factor of this device compensates for this reduction in current to attain an efficiency comparable to that of devices made from 86% RR and 96% RR P3HT. In addition, there appears to be a trend in V_{oc} where higher RR gives a lower V_{oc}. On average, 96% RR P3HT devices had a V_{oc} of 0.58V whereas 86%RR devices had a V_{oc} of 0.62V.

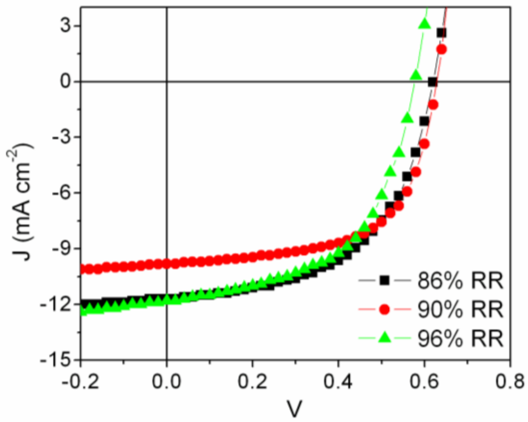

Figure 2.1. IV characteristics of optimized devices made from 86%, 90%, and 96% RR P3HT blended with PCBM at 55:45 weight ratio. 86%RR(■): Voc = 0.62V, Jsc = 11.7mA/cm^2, FF = 0.54, PCE = 3.9%; 90%RR(●): Voc = 0.63V, Jsc = 9.8mA/cm^2, FF = 0.61, PCE = 3.8%; 96%RR(▲): Voc = 0.58V, Jsc = 11.8mA/cm^2, FF = 0.55, PCE = 3.8%.

The thermal stabilities of the photovoltaic devices are also examined and Figure 2.2 shows the evolution of the average efficiencies of eight P3HT-PCBM BHJ devices after thermal annealing at 150°C for various times. Un-annealed devices all have <1% efficiencies (not shown on figure). After 10 minutes of annealing, 96% RR P3HT devices have achieved their highest efficiencies while 90% RR and 86% RR P3HT devices require longer annealing times to achieve power conversion efficiencies in excess of 3%. However, the trend is reversed for longer annealing times. Devices consisting of 96% RR P3HT decay quickly to less than 2% PCE after 5 hours of annealing, whereas devices with 86% RR and 90% RR P3HT are able to maintain ~3% PCE after more than 10 hours of annealing at 150°C, which serves as an accelerated performance test.

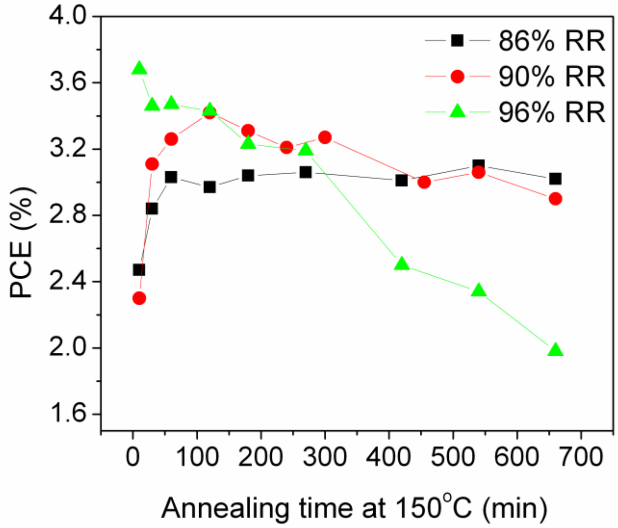

Figure 2.2. Average efficiencies of 86%, 90%, and 96% RR P3HT-PCBM BHJ devices annealed at 150°C for different times. The efficiency of 96% RR P3HT devices decreased drastically after 5 hours of annealing, but the 90% and 86% RR devices maintained ~3% efficiencies after 11 hours of annealing.

2.2.2 Blend Morphology

Optical microscopy was used to provide a qualitative inspection of the P3HT:PCBM blend morphology. Figure 2.3 shows the optical micrographs of P3HT samples with different RR blended with PCBM at a 55:45 weight ratio and annealed at 150°C for 3 hours. As shown in Figure 2.3a, a blend of 86% RR P3HT with PCBM shows only a few small PCBM crystals, while the blend of 90%RR P3HT with PCBM (Figure 2.3b) shows larger and denser PCBM crystals within the same sized area, but there is still a considerable amount of well-mixed area where large PCBM crystals are absent. In contrast, the optical micrograph of a blend of 96% RR P3HT with PCBM (Figure 2.3c) shows many large needlelike PCBM crystals that are more than 100μm in length. These optical micrographs show that the morphology resulting from the blending of highly RR P3HT blends with PCBM displays extreme phase segregation after thermal annealing, which can damage performance in a solar cell since the effective area of the device decreases as aggregation of PCBM crystals take up larger areas. The same trend in morphology was observed under scanning electron microscopy (see Figure 2.7 in Experimental section). Zooming into the homogeneous parts of the film of both the 86% and the 96% RR P3HT:PCBM blend samples, one can see bi-continuous networks of P3HT and PCBM under transmission electron microscopy (see Figure 2.8 in Experimental section). Similar needlelike PCBM crystals in blend films with P3HT had been observed by others and were believed to be due to the fast diffusion of PCBM towards the PCBM crystals, with their growth rate dependent on blend compositions and annealing conditions.[31,32] Here, we have shown that, in addition to the processing conditions of the film, the chemical nature of the polymer significantly affects the extent of growth of these PCBM crystals during thermal annealing.

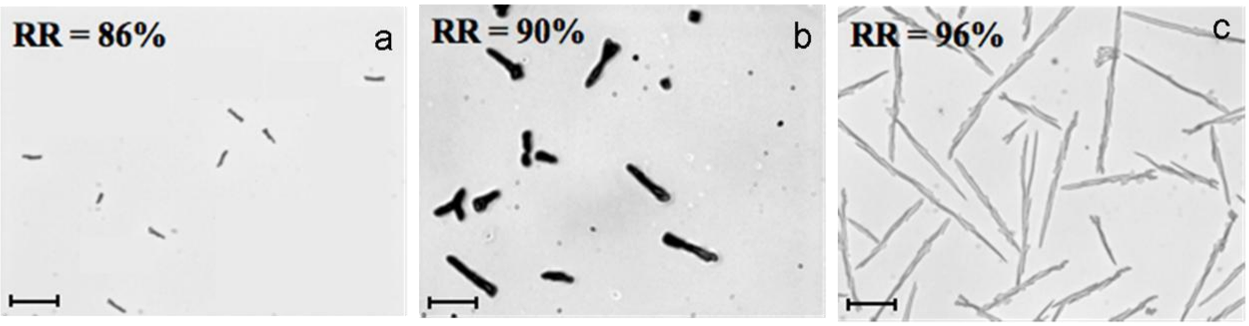

Figure 2.3. Optical microscopy images of 86%RR (a), 90%RR (b), and 96%RR (c) P3HT:PCBM blends at 55:45 wt ratio after 3 hours of annealing at 150°C. Dark areas are PCBM-rich regions.[31,32] Scale bar = 50 µm.

The blend morphology obtained from P3HT of different RR mixed with PCBM was probed by two dimensional grazing incidence X-ray scattering (GIXS) measurements. Figure 2.4 compares the GIXS patterns of 86%, 90%, and 96% RR P3HT blends with PCBM after 1 hour of annealing at 150°C. To produce identical surface conditions as samples for device measurement, a thin layer (20-30 nm) of PEDOT:PSS was spun onto silicon substrates and the P3HT:PCBM blend layer was subsequently spin-coated on top. The angle of incidence (~0.1°) was carefully chosen to allow for complete penetration of X-ray into the polymer film but only limited penetration into the substrate (to reduce the background). The 2-D image map of GIXS patterns can be divided into a component in the plane of the substrate ($\boldsymbol{q_x}$) and a component perpendicular to the substrate ($\boldsymbol{q_z}$) as shown in Figure 2.4. The (100), (200), and (300) diffraction peaks are strongest in the nominally out-of-plane direction, but with some arcing about this direction and some intensity in-plane (near $\boldsymbol{q_z} \approx 0$). This shows that the P3HT:PCBM blend films have a well-organized structure with most of the planar P3HT stacks oriented along the perpendicular axis of the substrate. From the diffraction pattern, we extract a lamella spacing of 1.59nm, which is consistent with that reported elsewhere.[17, 33] The peak near the top of the images at $q \approx 1.7$ Å^{-1} (d=0.38 nm) is the (010) peak resulting from the π-π stacking distance between P3HT chains.

The most distinct difference among the diffraction from the three samples occurs at $q \approx 1.4$ Å^{-1} (d=0.46 nm spacing), which is due to PCBM as determined by previous XRD measurements.[33] The $q \approx 1.4$ Å^{-1} diffraction peak of PCBM is much sharper and more prominent in the 96%RR P3HT blend film. In contrast, the PCBM peak is broad and diffuse in the two lower RR samples. These GIXS images show that the PCBM is highly crystalline for the P3HT:PCBM blend in the higher RR film, which is consistent with the observation of a larger extent of phase segregation from optical and electron microscopy.

Another noticeable and important difference among the samples is a difference in the extent of P3HT crystalline orientation. Specifically, the azimuthal angular width of the P3HT (100), (200) and (300) peaks in the 96% RR sample is much broader than for either the 90% RR or the 86% RR sample. This indicates that the P3HT stacks are less well oriented in the 96% RR sample, i.e. more of the stacks are oriented away from the perpendicular axis to the substrate. This could be attributed to the presence of large PCBM crystallites in the 96%RR sample that force the P3HT stacks to orient away from the perpendicular plane and in more random directions.

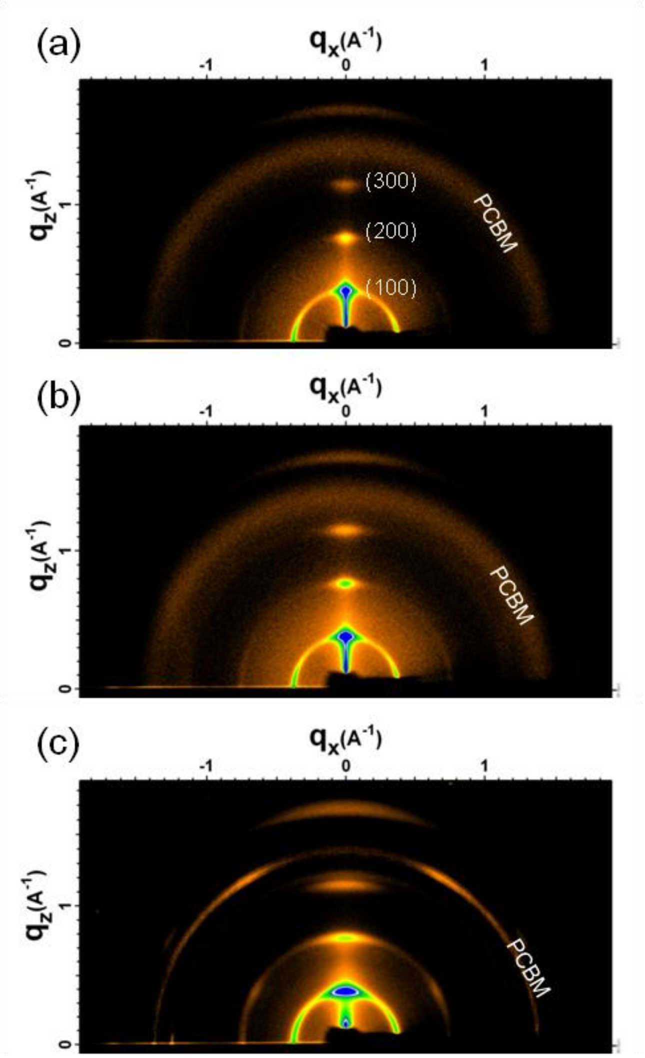

Figure 2.4. GIXS patterns of blend films of 86%RR (a), 90%RR (b), and 96%RR (c) P3HT:PCBM at a 55:45 ratio after 1 hr of annealing at 150°C. The vertical section at $q_x \approx 0$ is not the true specular direction (i.e. $q_x = 0$), but is tilted from this.

2.2.3 Polymer Properties

The optical, electronic, and thermal properties of the pristine polymers of different regioregularities were studied to investigate fundamental differences among these three polymers. The absorption spectra of thin films of P3HT of all three RR are shown in Figure 2.5. 96% RR P3HT has a higher optical density than the other two lower RR P3HT polymers. In addition, although all three polymers have similar absorption breadths, the 86% RR and 90% RR P3HT have blue-shifted λ_{max} at 514nm (7.3 x 10^4 cm^{-1}) and 519nm (6.8 x 10^4 cm^{-1}) respectively, compared to λ_{max} at 556nm (9.2 x 10^4 cm^{-1}) for the highly ordered 96% RR P3HT.

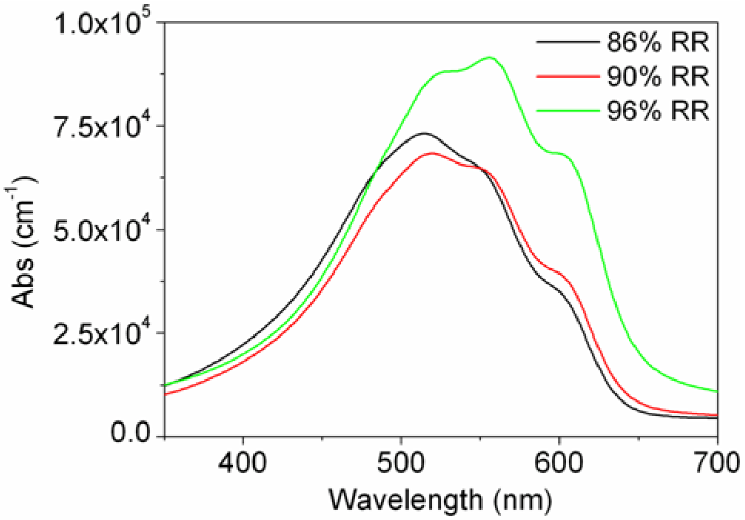

Figure 2.5. Absorption spectra of 86% RR, 90% RR, and 96% RR P3HT thin films annealed at 150°C for 1hr.

Besides absorption, charge carrier mobility is of great importance to solar cells. The space charge limited current mobility (SCLC) measures the mobility in the direction perpendicular to the electrodes and thus is the most representative measurement of charge carrier mobility for solar cells. For 86% RR, 90% RR, and 96% RR P3HT, the SCLC mobilities were measured to be 6.4×10^{-4} $cm^2\ V^{-1}\ s^{-1}$, 1.1×10^{-3} $cm^2\ V^{-1}\ s^{-1}$, and 1.1×10^{-3} $cm^2\ V^{-1}\ s^{-1}$. These measurements are consistent with typical values for P3HT.[34] In addition, this type of behavior where disrupting the order of the polymer does not affect the SCLC mobility has been observed for another poly-akylthiophene system.[35] Although the SCLC mobility of the 86% RR P3HT is slightly lower than the other two higher RR P3HTs, the same order of magnitude for mobilities for all three polymers indicate that reducing the RR within the range investigated does not significantly compromise the electronic properties of the polymer, as confirmed by device results shown above.

The GIXS results shown above suggest that there are differences in crystalline behavior (e.g., orientation) among the polymers of different RR and this difference has a strong influence on blend morphology. To elucidate the quantitative difference in the crystallinity of polymers, differential scanning calorimetry (DSC) measurement was performed. Degrees of crystallinity of the three polymer samples are calculated by comparing the heat of fusion for the particular polymer sample (ΔH_m) and the heat of fusion of an ideal crystal (ΔH_m^0 = 99 J/g).[36-38] For 86% RR, 90% RR and 96% RR P3HT, the degrees of crystallinity were measured to be 12%, 15%, and 21%, which are consistent with values reported by others for high MW P3HT measured by DSC.[36] These results show that crystallinity increases dramatically with RR. In addition, DSC traces show increases in both the melting temperature (T_m) and the crystallization temperature (T_c) with RR (see Figure 2.13). The lower T_m values in the lower RR samples indicate a more defective crystal structure. The two lower RR P3HTs also showed a shoulder peak near the melting temperature, which could be characteristic of the existence of multiple crystal structures in the polymer sample.[36,39] The second smaller peak may also have arisen as a consequence of the melting of a less defective crystal generated via fast crystallization of the initial melt.

2.3 Discussion

It had been proposed that highly regioregular P3HT was preferred in solar cells since it has a stronger tendency to self-organize within the film, thus leading to higher crystallinity,[13] charge carrier mobility,[17] and optical density.[13,18] Kim *et al*[13] concluded that higher RR is necessary for achieving high efficiency solar cells by comparing unoptimized device results. In their paper, they only optimized the processing conditions for the highest RR P3HT devices and achieved 4.4% PCE. In contrast, our results showed that with some optimization similar peak performance (~4%) can be attained for 86%, 90%, and 96% RR P3HT. Although higher RR P3HT may have a higher absorption coefficient, the difference between 86%RR and 96%RR polymers can easily be overcome by further optimization in the device fabrication process such as longer annealing times to achieve the desired morphology. Measurements of SCLC mobility have also demonstrated that electronic properties of the polymer are maintained while lowering RR within the range investigated. Moreover, devices made from lower RR P3HT displayed superior thermal stability, suggesting that lower RR could be a better choice for P3HT-PCBM composite cells.

The difference in thermal stability of the different RR P3HT blends with PCBM correlates with the observed active layer morphology as well as degree of crystallinity measurements. First, optical microscopy results illustrate that the extent of phase separation is larger in the higher RR P3HT:PCBM blend films after thermal annealing treatment at 150^{o}C. Large PCBM crystals can be seen under optical and electron microscopy, and the PCBM crystalline peak in GIXS is much sharper and more distinct in the 96%RR P3HT blend sample. Second, DSC measurement confirms that higher RR P3HT has a higher degree of crystallinity. These two observations suggest that the stronger driving force for crystallization of highly RR P3HT induces larger extent of phase segregation (i.e., larger domains of pure phases) in a blend film with PCBM at a given thermal annealing condition, leading to faster deterioration in device performance. Interestingly, Kim *et al*[13] also observed that a higher RR polymer had a higher degree of crystallinity, and they claimed that this higher crystallinity was beneficial to device performance since it led to enhanced optical and electronic properties. In comparison, our results suggest a different picture where the higher crystallinity of a higher RR P3HT was a disadvantage as it induces more phase segregation and leads to less thermally stable blend morphology.

Strong correlations between crystallization and the resulting morphology in polymer blends have been previously established. In particular, crystallization of one or both blend components is known to induce phase segregation.[40-42] Upon thermal annealing, crystallization of the highly ordered 96%RR P3HT as well as that of PCBM in the active layer of the device leads to extreme phase segregation of the two components resulting in large crystallites of PCBM, thus reducing the interfacial area for charge transfer and leading to lower efficiencies. On the other hand, the weaker crystallization of lower RR P3HT leads to weaker phase segregation in a blend film with PCBM and it is shown that the larger amorphous content in the polymer inhibits large scale PCBM crystallization such that the desired interpenetrating network can withstand longer annealing treatment, thus improving the thermal stability of the device. In other words, although 86%RR P3HT may have slightly lower charge carrier mobility and optical density, its lower degree of crystallinity gives it an advantage in limiting the extent of phase segregation with

PCBM upon thermal annealing and maintaining the desired morphology for bulk heterojunction solar cells. While previous papers have focused on controlling PCBM diffusion by blend composition and annealing conditions,[31, 32] our result is the first example of using varying degrees of polymer crystallinity to control phase segregation.

Of particular interest is the disruption in the orientation of P3HT crystals in the highly crystalline 96%RR polymer, which is indicated by the broadening of the crystalline peaks of P3HT shown in GIXS patterns. This is possibly due to the aggregation of PCBM which can push P3HT crystallites away from the preferred orientation. Figure 2.6a is a schematic illustration of the twisting of P3HT stacks away from the perpendicular plane by the presence of large PCBM crystals. In the highly RR P3HT sample, upon thermal annealing, PCBM diffuses away from the highly crystalline polymer and aggregates together to a larger extent than in lower RR P3HT, and these large crystallites could cause the leaning of P3HT stacks. Therefore, the P3HT stacks become more randomly oriented so that fewer of them are perpendicular to the substrate, thus leading to broader crystalline P3HT peaks under X-ray scattering. In contrast, lower RR P3HT:PCBM blends have a lesser extent of phase segregation, leading to fewer and smaller PCBM crystals and thus minimizing the randomization of the orientation of P3HT stacks, as illustrated in the schematic in Figure 2.6b and confirmed by the narrower crystalline P3HT peaks in GIXS.

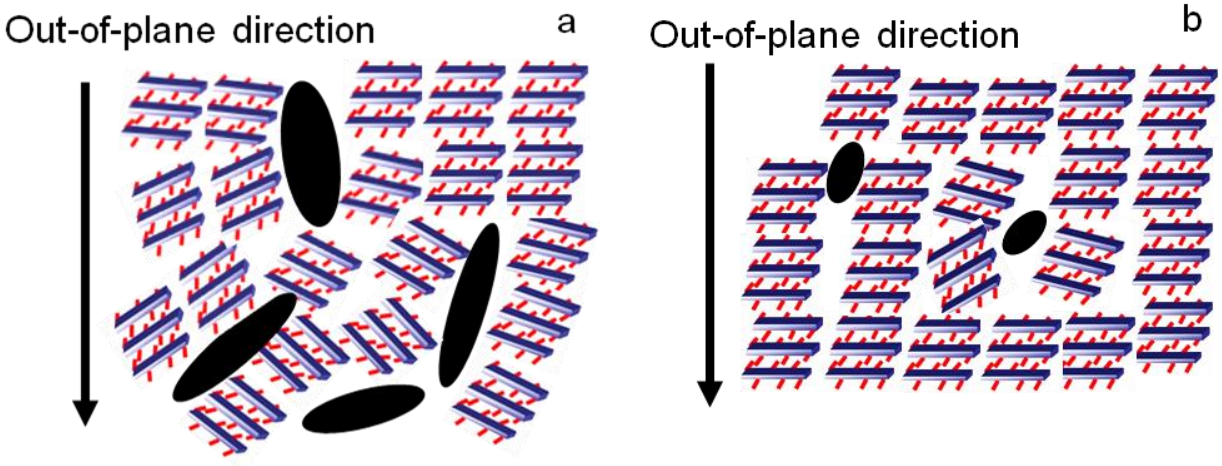

Figure 2.6. Schematic of high RR P3HT:PCBM blend film with many large PCBM crystallites that cause the P3HT stacks to orient away from the out-of-plane direction (a), and low RR P3HT:PCBM blend film with fewer and smaller PCBM crystallites and more ordered P3HT stacks (b).

Considering the effect of crystallization-induced phase segregation, the regioregularity of P3HT should be optimized to maintain high electronic properties and initial device performance while improving thermal stability. Introducing a controlled amount of disorder to the polymer can lead to better blending with PCBM and more stable active layer morphology. This suggests that in terms of future designs of polymers for solar cells, instead of trying to obtain the highest crystallinity to achieve better electronic properties and higher initial device performance, an alternative strategy would be directed towards the search for a polymer that would have favorable interactions with the acceptor material so as to realize the best and most stable morphology for BHJ solar cells.

2.4 Conclusions

We have shown that regioregularity is an important variable that affects polymer crystallinity, blend morphology and device performance. For pristine polymer films, as used in organic transistors, a more regioregular polymer with higher crystallinity and higher mobility gives rise to a better device due to better charge transport. However, in polymer-fullerene composite solar cells, considerations for the properties of the pristine polymer are complicated by the addition of another component where blend morphology becomes an important variable. Although higher RR P3HT has higher optical density and charge carrier mobility, its increased degree of crystallinity in fact becomes a disadvantage as it induces more severe phase segregation with PCBM upon thermal annealing. Although only a few regioregularities were examined in this paper, we have demonstrated that high RR is not necessary to achieve high efficiency solar cells, and using a polymer with a lower RR actually has the benefit of improving the thermal stability of the device.

In particular, the 86%RR P3HT sample we synthesized not only has sufficient electronic properties to afford high efficiency photovoltaic devices, but it also has the advantage of producing more thermally stable devices due to less crystallization-induced phase segregation of PCBM. Evidence from optical and electron microscopy and GIXS supports the hypothesis that highly crystalline 96%RR P3HT blends develop many large PCBM crystals that are detrimental to device performance. Our results emphasize the need to take into account the interaction of blending components while designing materials for BHJ solar cells. In addition to good optical and electronic properties, a polymer for photovoltaic applications must also blend well with the acceptor material in order to achieve the ideal composite morphology with sufficient thermal stability.

2.5 Experimental

2.5.1 Synthetic Details

All chemicals were purchased from Aldrich and used without further purification unless stated otherwise. All reactions were performed under nitrogen in glassware that had been flame dried under vacuum. All compounds were characterized by ^{1}H NMR (400 MHz) and ^{13}C NMR (75 MHz) on a Bruker AVB 400 or AVQ 400. High-resolution mass spectra and elemental analysis (CHNS) was performed at the University of California, Berkeley Department of Chemistry analytical services. Polymer ^{1}H NMR (500 MHz) were obtained on Bruker DRX 500. For polymer molecular weight determination, polymer samples were dissolved in HPLC grade dichlorobenzene at a concentration of 1 mg/ml and stirred overnight at room temperature prior to filtering through a 0.2 μm PVDF filter and SEC was performed using HPLC grade dichlorobenzene at a flow rate of 0.8 μL/min on two 300 x 8 mm linear S SDV, 5 micron columns (Polymer Standards Services, USA Inc.) at 70 ºC using a Waters (Milford, MA) 2690 separation module and a Waters 486 Tunable Absorption Detector monitored at 350 nm. The instrument was calibrated vs. polystyrene standards (1,050 – 135,000 g/mol) and data was analyzed using Millenium 3.2 software.

Regioregularity values were calculated by comparing the integrated peaks of the ^{1}H NMR corresponding to the α-methylene protons on the hexyl chains in head-to-tail (HT) versus head-to-head (HH) linkages[43] at δ2.78 and δ2.54 respectively in Figures S1-S3. The reported regioregularities were calculated by dividing the integrated area of the peak centered at δ2.79 by the combined area of the peaks at δ2.79 and δ2.56. The margin of error on the %RR values is estimated to be about ±1%.

Scheme 2.1.

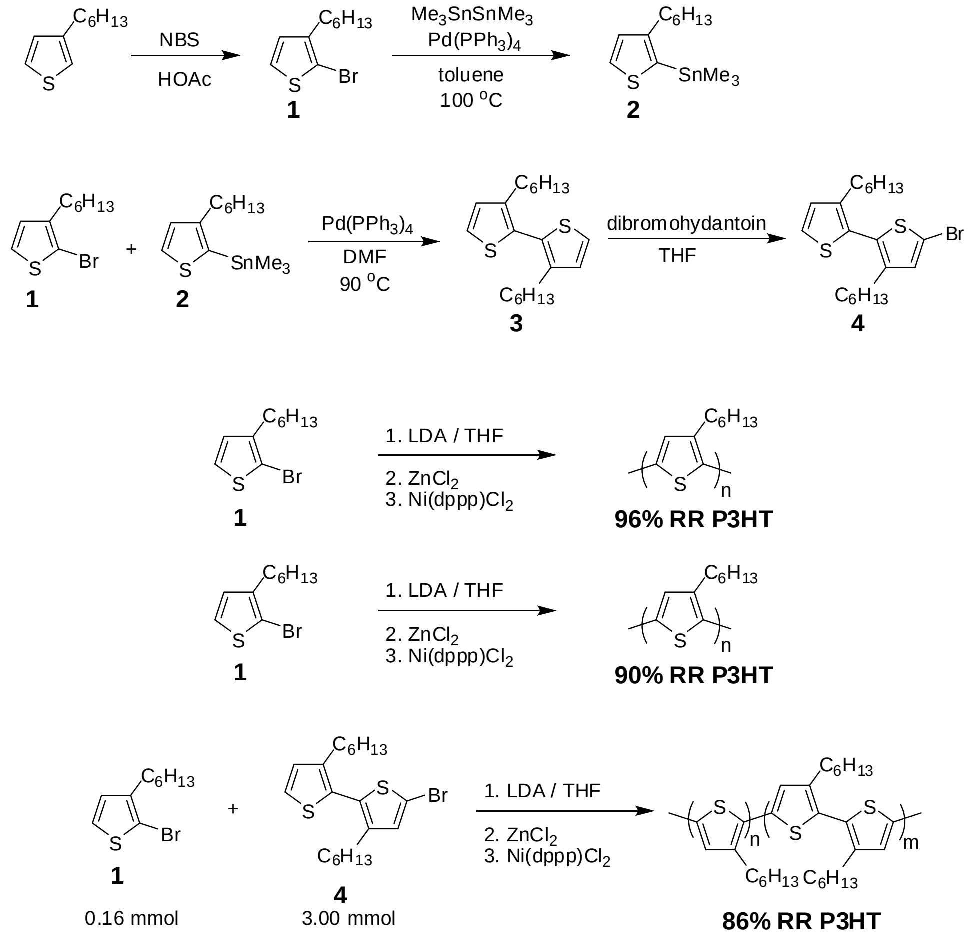

2-Bromo-3-hexylthiophene (1). In 50 mL of glacial acetic acid, 4.97 g (29.6 mmol) of 3-hexylthiophene was dissolved. Then, 5.29 g (29.7 mmol) of freshly recrystallized NBS was added in one portion. The internal temperature of the reaction increased to 35 ºC with concomitant dissolution of NBS. The reaction was stirred until it cooled back to room temperature and was then poured into 150 mL of water and 150 mL of ether. The organic layer was separated and washed five times with 2 M NaOH, followed by an aqueous wash. The organic layer was then dried over $MgSO_4$ and the ether was removed by rotary evaporation. Distillation of the crude product (60 ºC, 300 mTorr) gave 7.01 g (96%) of the product as a clear oil. ^{1}H NMR (400 MHz, $CDCl_3$) δ 7.17 (d, 1H), 6.78 (d, 1H), 2.55 (t, 2H), 1.55 (m, 2H), 1.30 (m, 6H), 0.88 (t, 3H).

2-trimethylstannyl-3-hexylthiophene (2). In a 500 ml three-neck flask, 10.17 g (41.2 mmol) of **1** and 14.18 g of hexamethylditin (43.3 mmol, 1.05 eq) were combined in 200 ml of toluene and the mixture was degassed by bubbling with nitrogen for 20 minutes. Then 1.00 g of $Pd(PPh_3)_4$ was added and the reaction was heated to 100 °C for four days. The reaction mixture was then cooled to room temperature and water was added. After extraction with ether, the organic phase was dried with Na_2SO_4 and solvent was removed under vacuum. The product was then isolated via distillation (86 °C, 160 mtorr) as a clear oil (8.302 g, 49%). ^1H NMR (400 MHz, $CDCl_3$) δ 7.52 (d, 1H), 7.09 (d, 1H), 2.62 (t, 2H), 1.58 (m, 2H), 1.34 (br m, 6H), 0.89 (t, 3H), 0.37 (s, 9H).

3,3'-dihexyl-2,2'-bithiophene (3). In a 250 ml three-neck flask, 1.007 g (4.08 mmol) of **1** and 1.773 g (4.28 mmol) of **2** were dissolved in 40 ml DMF and the mixture was degassed by bubbling with nitrogen for 20 minutes. Then 2.5 mol% of $Pd(PPh_3)_4$ (120 mg) was added and the reaction was heated to 90 °C for 12 hours. The reaction was then cooled to room temperature and water was added prior to extraction with ether and drying of the organic phase with $MgSO_4$. The product was then isolated via silica chromatography with hexanes as the eluent to yield 1.33 g (98%) of the product as a clear oil. ^1H NMR (400 MHz, $CDCl_3$) δ 7.28 (d, 2H), 6.96 (d, 2H), 2.50 (t, 4H), 1.53 (m, 4H), 1.24 (br m, 12H), 0.86 (t, 6H). ^{13}C NMR (70 MHz, $CDCl_3$) δ 142.3, 128.7, 128.5, 125.2, 31.6, 30.7, 29.1, 28.8, 22.6, 14.1.

5-bromo-3,3'-dihexyl-2,2'-bithiophene (4). In a 50 ml flask, 1.30 g of **3** was dissolved in 20 ml of THF and cooled to 0 °C. Then 560 mg (0.5 eq) of 1,3-Dibromo-5,5-dimethylhydantoin was added portion-wise. The reaction was then stirred for 30 minutes at 0 °C and then warmed to room temperature for 1.5 hours. The reaction mixture was then poured into hexanes and the resulting mixture was stirred at 0 °C for 30 minutes. The mixture was then filtered to remove all solids and the filtrate was concentrated under vacuum. The crude product was then purified via silica chromatography using hexanes as the eluent to give the product in 70% yield as a clear oil (1.12 g). ^1H NMR (400 MHz, $CDCl_3$) δ 7.28 (d, 1H), 6.93 (d, 1H), 6.91 (s, 1H), 2.48 (t, 2H), 2.42 (t, 2H), 1.49 (m, 4H), 1.24 (br m, 12H), 0.85 (t, 6H). ^{13}C NMR (70 MHz, $CDCl_3$) δ 143.2, 142.9, 131.3, 130.2, 128.6, 127.4, 125.8, 111.6, 31.6, 31.5, 30.7, 30.5, 29.1, 29.0, 28.8, 28.7, 22.6, 22.5, 14.1. HRMS calcd for $C_{20}H_{29}BrS_2$ (M^+), 412.0894; found 412.0895. Anal. calcd for $C_{20}H_{29}BrS_2$: C, 58.10; H, 7.07; S, 15.51. Found: C, 58.09; H, 6.91; S, 15.19.

96% RR-P3HT. In 40 ml of THF, 1.183 g (4.8 mmol) of **1** was dissolved and cooled to -78 °C. In 20 ml of THF, 4.8 mmol LDA was added and the mixture was stirred at -78 °C for one hour. Then $ZnCl_2$ (1.1 eq, 5.3 mmol, 720 mg) was added and the mixture was stirred at -78 °C for 20 minutes and then warmed to room temperature for one hour prior to the addition of 25 mg of $Ni(dppp)Cl_2$. The reaction was then stirred overnight at room temperature. The thick purple mixture was then precipitated in methanol, filtered, and the solid was subjected to Soxhlet extraction with methanol, followed by hexanes. The polymer was then taken up by Soxhlet extraction with chloroform and isolated by precipitation from chloroform into methanol to give 615 mg (77%) of product. See Figure 2.9 for ^1H NMR.

90%RR-P3HT. In 125 ml of THF, 2.080 g (8.4 mmol) of **1** was dissolved and cooled to -78 °C. In 25 ml of THF, 8.3 mmol LDA was added and the mixture was stirred at -78 °C for one hour. Then $ZnCl_2$ (9.5 mmol, 1.30 g) was added and the mixture was stirred at -78 °C for 20 minutes and then warmed to room temperature for one hour prior to the addition of 45 mg of Ni(dppp)Cl_2. The reaction was then stirred overnight at room temperature. The thick purple mixture was then precipitated in methanol, filtered, and the solid was subjected to Soxhlet extraction with methanol, followed by hexanes. The polymer was then taken up by Soxhlet extraction with chloroform and isolated by precipitation from chloroform into methanol to give 830 mg (59%) of product. See Figure 2.10 for ^1H NMR.

86%RR-P3HT. In a 100 ml three-neck flask, 738 mg (3.00 mmol) of **1** and 67 mg (0.16 mmol) of **4** were dissolved in 35 ml of THF and cooled to -78 °C. Then, 1 eq (3.16 mmol) of LDA was added in 15 ml of THF and the mixture was stirred at -78 °C for one hour. Then $ZnCl_2$ (4.3 mmol, 580 mg) was added and the mixture was stirred at -78 °C for 20 minutes and then warmed to room temperature for one hour prior to the addition of 25 mg of Ni(dppp)Cl_2. The thick purple mixture was then precipitated in methanol, filtered, and the solid was subjected to Soxhlet extraction with methanol, followed by hexanes. The polymer was then taken up by Soxhlet extraction with chloroform and isolated by precipitation from chloroform into methanol to give 428 mg (78%) of product. See Figure 2.11 for ^1H NMR.

Table 2.1. Molecular weight and PDI of P3HT measured by SEC

RR	M_n (g/mol)	PDI
96%	28,600	1.5
90%	18,000	1.4
86%	25,700	1.5

The PCBM was synthesized in-house by the method first reported by Hummelen *et al* in 1995 and was purified using the same reported procedures.[44]

UV-Visible absorption spectra were obtained using a Carey 50 Conc UV-Visible spectrophotometer. For thin film measurements polymers were spin coated onto untreated glass slides from chlorobenzene solution (30 mg/ml). A model P6700 Spincoater was used to spin coat the films at 2000 RPM for 60 s.

Polymer mobility was measured using a diode configuration of ITO/ PEDOT:PSS/ Polymer/Al in the space charge limited current regime. At sufficient potential the conduction of charges in the device can be described by

$$J_{SCLC} = \frac{9}{8}\varepsilon_R \varepsilon_o \mu \frac{V^2}{L^3}, \qquad (1)$$

where ε_0 is the permittivity of space, ε_R is the dielectric constant of the polymer (assumed to be 3), μ is the mobility of the majority charge carriers, V is the potential across the device ($V = V_{applied} - V_{bi} - V_r$), and L is the polymer layer thickness. The series and contact resistance of the device (13-21 Ω) was measured using a blank (ITO/PEDOT/Al) and the voltage drop due to this resistance (V_r) was subtracted from the applied voltage. The built-in voltage (V_{bi}), which is based on the relative work function difference of the two electrodes, was also subtracted from the applied voltage. The built-in voltage can be determined from the transition between the ohmic region and the SCL region and is found to be about 1 V. Polymer film thickness was measured by a Veeco Dektak profilometer.

Differential Scanning Calorimetry measurements were performed on a TA instrument DSC

Q200. The samples (~5mg) were heated from 40^{o}C to 260^{o}C at a heating rate of 10^{o}C min^{-1} under N_2 atmosphere. Samples were prepared by drop casting a 30mg/mL chlorobenzene solution onto the DSC pan and letting the solvent slowly evaporate under Argon atmosphere before DSC measurements.

2.5.2 Photovoltaic Device Fabrication

All solar devices have a layered structure with the photoactive layer consisting of a P3HT and PCBM blend sandwiched between the two electrodes, ITO and Al. Glass substrates coated with a 150nm sputtered ITO pattern of 20 $\Omega\ \square^{-1}$ resistivity were obtained from Thin Film Device, Inc. The ITO-coated glass substrates were ultrasonicated for 20 min each in acetone, and then 2 % Helmanex soap water, followed by extensive rinsing and ultrasonication in deionized water, and then isopropyl alcohol. The substrates were then dried under a stream of air. A dispersion of PEDOT:PSS (Baytron-PH500) in water was filtered (1μm glass) and spin coated at 3400 RPM for 60s, affording a ~20-30 nm layer. The substrate was dried for 15 min at 140^{o}C in air and then transferred into an Argon glove box for subsequent procedures. Separate solutions of P3HT and PCBM were prepared in chlorobenzene at a concentration of 30mg/ml. The solutions were stirred for 24 hrs and passed through 0.45μm PTFE syringe filer before they were mixed at a 55:45 ratio and diluted with chlorobenzene to make a 13.5mg/ml P3HT and 11.0mg/mL PCBM blend solution. The blend solution was applied to the substrate and spun at 1200 RPM for 60s on top of the PEDOT:PSS layer. The substrates were then placed in an evaporation chamber and pumped down in vacuum (~10^{-7} torr) before evaporating a ~100nm Al layer through a shadow mask on top of the photoactive layer. The configuration of the shadow mask afforded eight independent devices on each substrate, and each device has an active layer of ~0.03cm^{2}. The mechanical removal of part of the organic layer allowed contact with the ITO, and adding conductive paste to the removed area to ensure electrical contact completed the device. Thermal annealing was performed after Al deposition by directly placing the completed device on a temperature-controlled hotplate at 150^{0}C inside the glove box. Devices were cooled to room temperature before testing. Testing of the devices was performed under an argon atmosphere with an Oriel Xenon arc lamp with an AM 1.5G solar filter. Current–voltage behavior was measured with a Keithley 236 SMU. Eight devices were averaged for each condition.

2.5.3 Morphology Characterization

Optical Microscopy

Optical microscopy samples were prepared by spin coating the same P3HT:PCBM solutions onto pre-cleaned glass substrates and annealed on top of hot plates. Microscopic evaluations were performed using a Nikon TE200 inverted fluorescence microscope (Scientific Instrument Company, Sunnyvale, CA). Images were acquired with a Micropublisher 5.0 RTV CCD camera from QImaging (Burnaby, BC, Canada).

Grazing-Incidence X-ray Scattering (GIXS)

GIXS experiments were conducted at the Stanford Synchrotron Radiation Laboratory on beamline 11-3. The sample is irradiated at a fixed incident angle on the order of a tenth of a degree and the GIXS patterns are recorded with a 2-D image detector (MAR345 image plate detector). GIXS patterns were recorded with an X-ray energy of 12.72 keV (λ=0.975Å). To maximize the intensity from polymer sample, the incident angle (~0.1°-0.12°) was carefully chosen so that the X-ray beam penetrates the polymer sample completely but not the silicon substrate. Typical exposure times were 90-180 sec. To produce identical surface condition as samples for device fabrication, a thin layer (20-30 nm) of PEDOT:PSS (Baytron Ph500) was spun onto silicon substrates with a native oxide. And then GIXS samples were prepared by spin-coating the same solutions used for making solar devices onto silicon substrates at 1200RPM for 60s. The substrates were placed directly on top of hot plates under Argon for thermal annealing.

Scanning Electron Microscopy (SEM)

SEM samples on silicon substrates were prepared under identical condition as GIXS samples. Imaging was performed using a **Zeiss Gemini Ultra-55 Analytical Scanning Electron Microscope with an in-lens secondary electron detector with resolution of 1nm** at beam energy of 10kV. Measurements were performed at the Imaging and Manipulation Facility at the Molecular Foundry in Lawrence Berkeley National Lab.

Transmission Electron Microscopy (TEM)

TEM images were obtained using a FEI TECNAI G^2 with a 200 kW accelerating voltage. Samples were prepared by spin-casting films from chlorobenzene as used for device measurement on to freshly cleaved NaCl single crystal substrates at 1500RPM for 60s. The films were floated onto water and placed onto a 600 mesh copper TEM grid (Electron Microscopy Science, Inc.).

2.5.4 Additional Figures

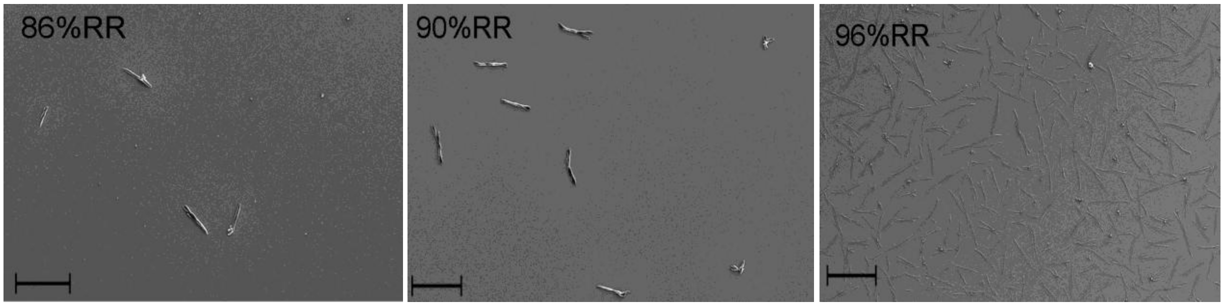

Figure 2.7. SEM images of P3HT: PCBM blend films at 55:45 weight ratio annealed at 150°C for 3 hrs. Scale bar = 100μm.

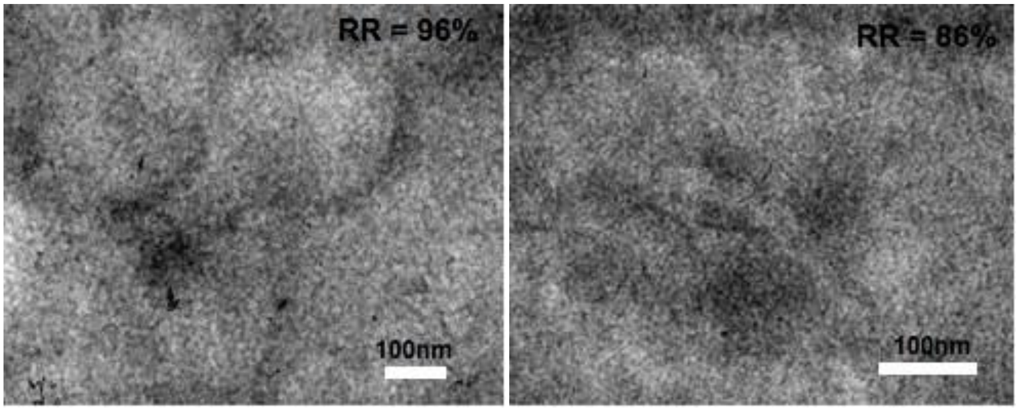

Figure 2.8. Additional TEM images to show the similar bicontinuous network achieved in 96%RR (top) and 86%RR (bottom) P3HT:PCBM blend films at 55:45 wt ratio and annealed at 145^{o}C for 15min.

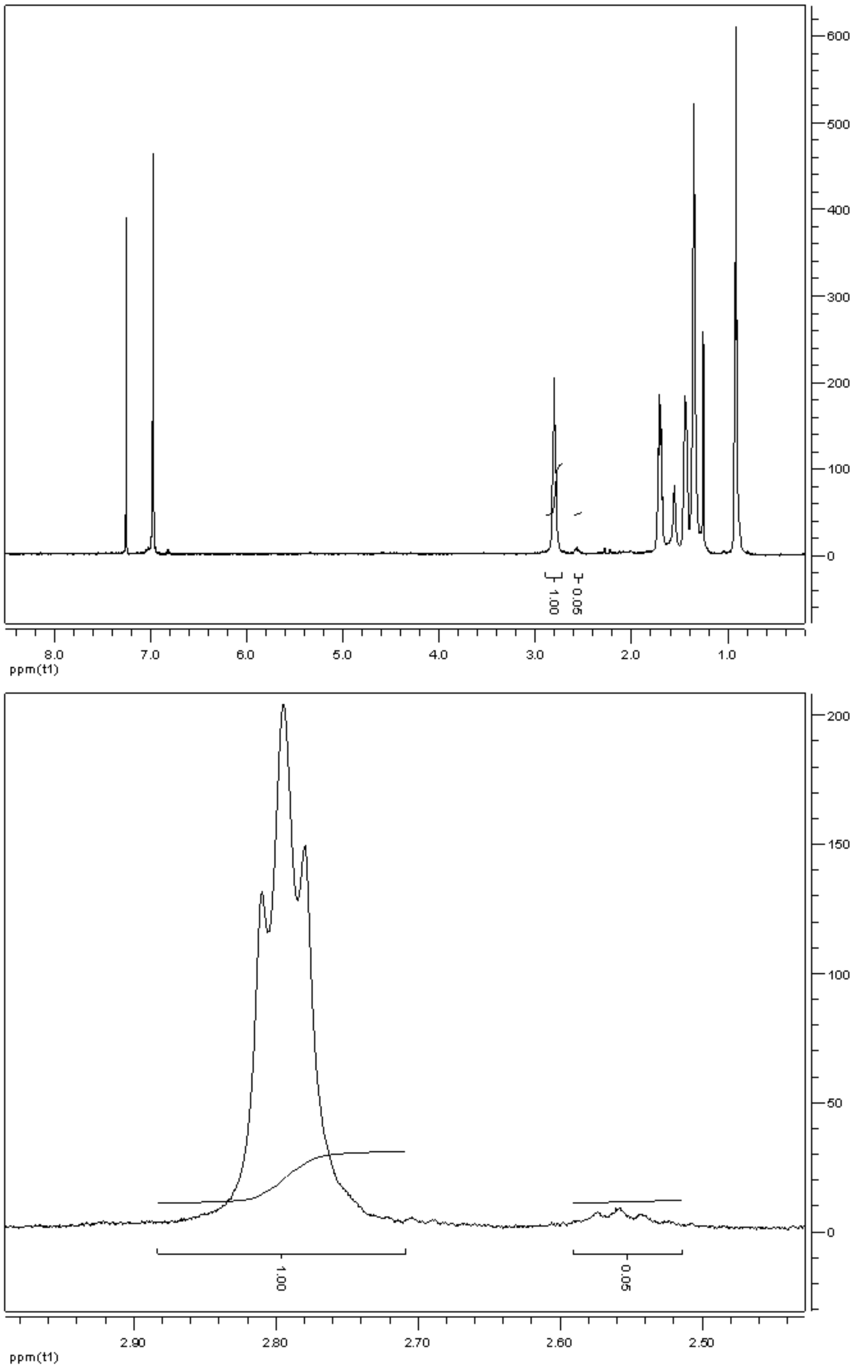

Figure 2.9. ^{1}H NMR and expanded region with integration for 96% RR P3HT.

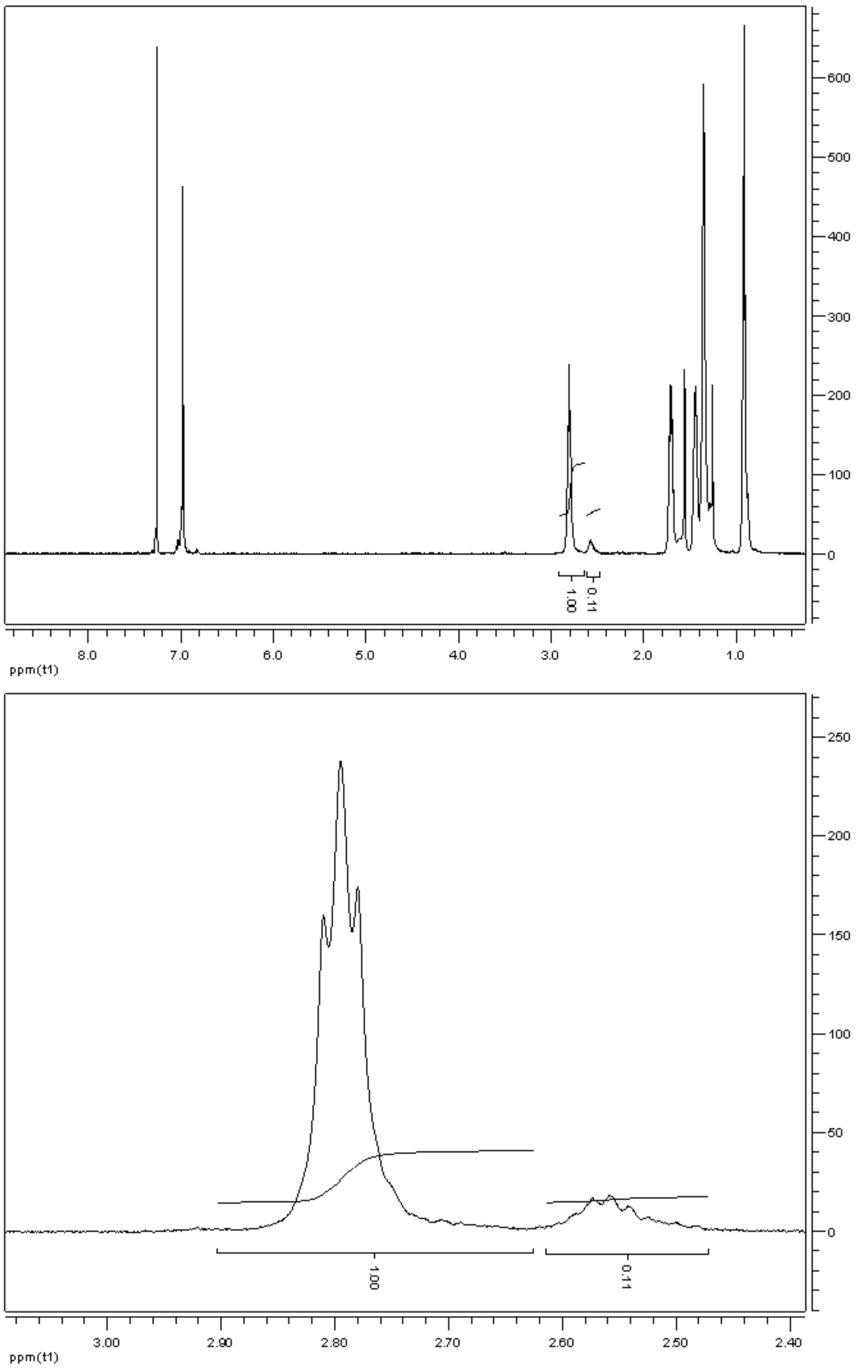

Figure 2.10. ^{1}H NMR and expanded region with integration for 90% RR P3HT.

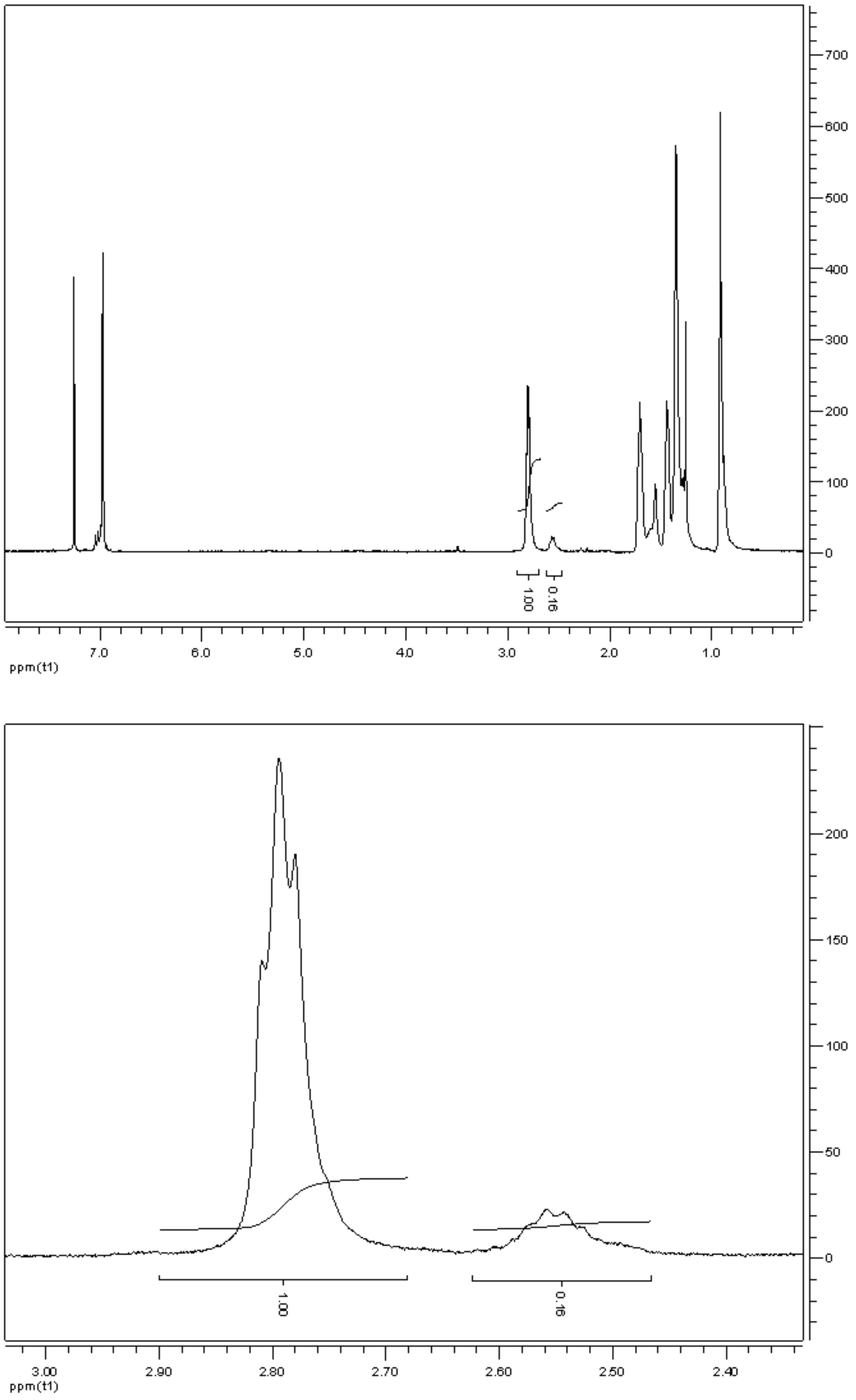

Figure 2.11. ^{1}H NMR and expanded region with integration for 86% RR P3HT.

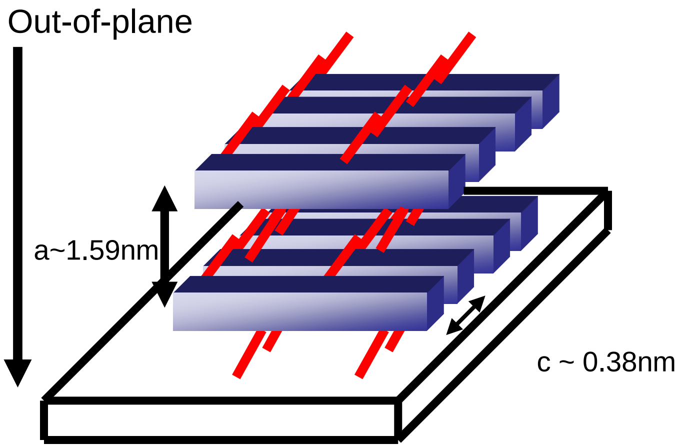

Figure 2.12. Schematic of the organization of P3HT chains relative to the substrate and domain spacing.

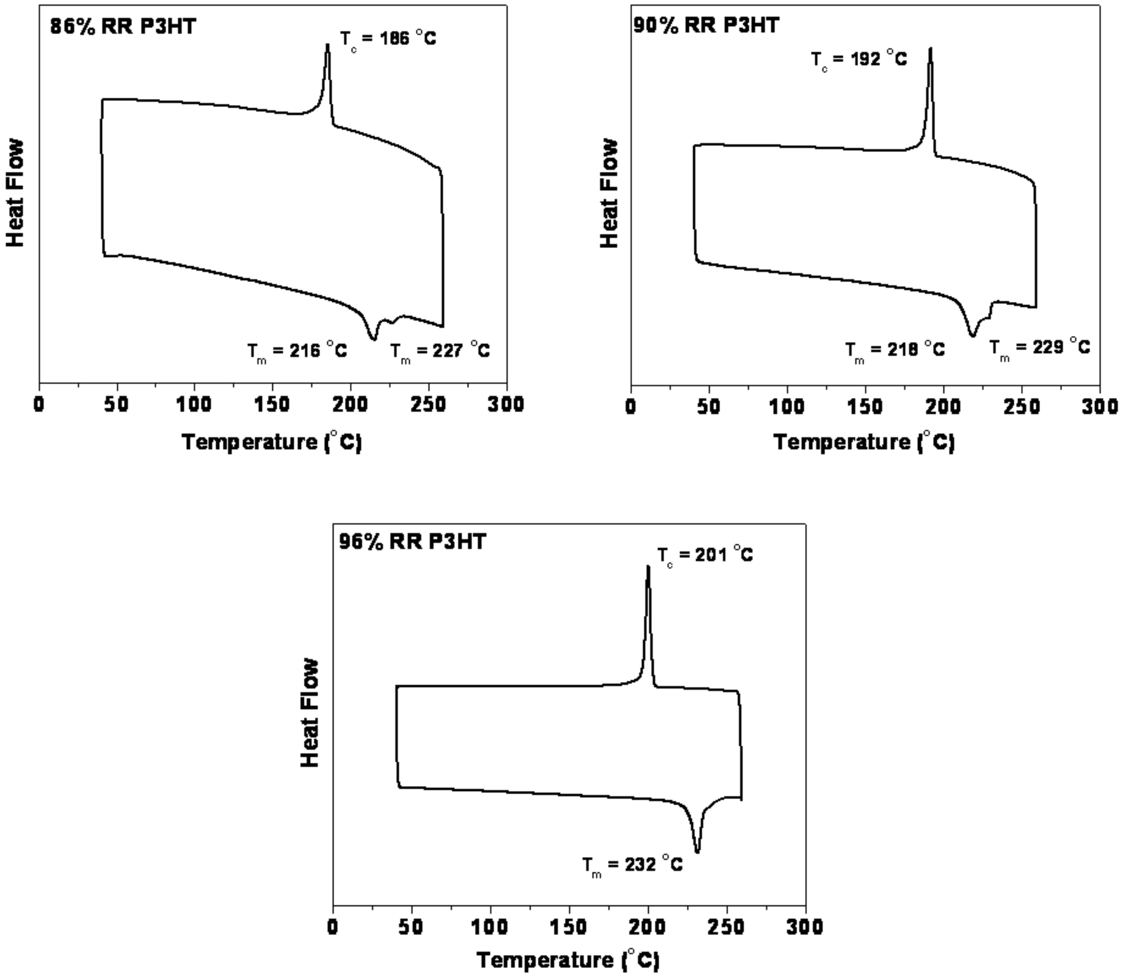

Figure 2.13. Second cycles of DSC scans for 86% RR, 90% RR, and 96% RR P3HT.

2.6 References

(1) Thompson, B. C.; Fréchet J. M. J. *Angew. Chem., Int. Ed*. **2008**, 47, 58-77.
(2) Gunes, S.; Neugebauer, H.; Sariciftci, N. S. *Chem. Rev.* **2007**, 107, 1324-1338.
(3) Ma, W.; Yang, C.; Gong, X.; Lee, K.; Heeger, A. J. *Adv. Funct. Mater.* **2005**, *15*, 1617-1622.
(4) Li, G.; Shrotriya, V.; Huang, J.; Yao, Y.; Moriarty, T.; Emery, K.; Yang, Y. *Nat. Mater.* **2005**, 4, 864-868.
(5) Hoth, C. N., Choulis, S.A.; Schilinsky, P.; Brabec, C. J. *Adv. Mater.* **2007,** 19, 3973-3978.
(6) Peet, J.; Kim, J. Y.; Coates, N.E.; Ma, W. L.; Moses, D.; Heeger, A. J.; Bazan, G. C. *Nat. Mater.* **2007,** 6, 497-500.
(7) Wienk, M. M.; Turbiez, M.; Gilot, J.; Janssen, R. A. J. *Adv. Mater.* **2008**, 20, 2556-2560.
(8) Thompson, B. C.; Kim, Y.; McCarley, T. D.; Reynolds, J. R. *J. Am. Chem. Soc.* **2006,** 128, 12714-12725.
(9) Blouin,N.; Michaud, A.; Gendron, D.; Wakim, S.; Blair, E.; Neagu-Plesu, R.; Belletete, M.; Durocher, G.; Tao, Y.; Leclerc, M. *J. Am. Chem. Soc.* **2008,** 130, 732-742
(10) Scharber, M.; Mühlbacher, D.; Koppe, M.; Denk, P.; Waldauf, C.; Heeger, A. J.; Brabec, C. J. *Adv. Mater.* **2006**, 18, 789-794.
(11) Schilinsky, P.; Asawapirom, U.; Scherf, U.; Biele, M.; Brabec, C. J. *Chem. Mater.* **2005,** 17*,* 2175-2180.
(12) Ma, M.; Kim, J.Y.; Lee, K.; Heeger, A. J. *Macromol. Rapid Commun.* **2007**, 28, 1776-1780.
(13) Kim, Y.; Cook, S.; Tuladhar, S. M.; Choulis, S.A.; Nelson, J.; Durrant, J. R.; Bradley, D.D. C.; Giles, M.; McCullough, I.; Ha, C. S.; Ree, M. *Nat. Mater.* **2006**, 5, 197-203.
(14) Urien, M.; Bailly, L.; Vignau, L.; Cloutet, E.; de Cuendias, A.; Wantz, G.; Cramail, H.; Hirsch, L.; Parneix, J. *Polym. Int.* **2008**, 57, 764-769.
(15) Kline, R. J.; McGehee, M. D.; Kadnikova, E. N.; Liu, J.; Fréchet, J. M. J.; Toney, M. F. *Macromolecules* **2005**, 38, 3312-3319.
(16) Zen, A.; Pflaum, J.; Hirschmann, S.; Zhuang, W.; Jaiser, F.; Asawapirom, U.; Rabe, J. P.; Scherf, U.; Neher, D. *Adv. Funct. Mater.* **2004,** 14, 757-764.
(17) Sirringhaus, H.; Brown. P. J.; Friend, R. H.; Nielsen, M. M.; Bechgaard, K.; Langeveld-Voss, B. M. W.; Spiering, A. J. H.; Janssen, R. A. J.; Meijer, E. W.; Herwig, P.; de Leeuw, D. M. *Nature*, **1999**, 401, 685-688.
(18) Barta, P.; Cacialli, F.; Friend, R. H.; Salaneck, W. R.; Zagorska, M.; Prori, A. *Synth. Met.* **1999**, 101, 296-297.
(19) Kim, Y.; Choulis, S.A.; Nelson, J.; Bradley, D. D. C.; Cook, S.; Durrant, J. R. *Appl. Phys. Lett.* **2005,** 86, 063502.
(20) Chu, C.-W.; Yang H.; Hou, W.J.; Huang, J.; Li, G.; Yang, Y. *Appl. Phys. Lett.* **2008,** 92, 103306.
(21) Nakamura, J.; Murata, K.; Takahashi, K. *Appl. Phys. Lett.* **2005,** 87, 132105.
(22) Chirvase, D.; Parisi, J.; Hummelen, J. C.; Dyakonov, V. *Nanotechnology,* **2004**, 15, 1317-1323.
(23) Shrotriya, V.; Yao, Y.; Li, G.; Yang, Y. *Appl. Phys. Lett.* **2006**, 89, 063505.
(24) Reyes-Reyes, M.; Kim, K.; Carroll, D. L. *Appl. Phys. Lett.* **2005,** 87, 083506.

(25) Yang, X.; Loos, J.; Veenstra, S. C.; Verhees, W. J. H.; Wienk, M. M.; Kroon, J. M.; Michels, M. A. J.; Janssen, R. A. J. *Nano Letters.* **2005**, 5, 579-583.

(26) Ko. C.-J.; Lim. Y.-K.; Chen, F.-C.; Chu, C.-W. *Appl. Phys. Lett.* **2007,** 90, 063509.

(27) Kim, J. Y.; Kim, S. H.; Lee. H.-H.; Lee, K.; Ma, W.; Gong, X.; Heeger, A. J. *Adv. Mater.* **2006,** 18, 572-576.

(28) Sivula, K; Luscombe, C.K.; Thompson, B.C.; Fréchet, J.M.J. *J. Am. Chem. Soc.* **2006**, 128, 13988.

(29) Schilinsky, P.; Asawapirom, U.; Scherf, U.; Biele, M.; Brabec, C. J. *Chem. Mater.* **2005,** 17*,* 2175-2180.

(30) Ma, M.; Kim, J.Y.; Lee, K.; Heeger, A. J. *Macromol. Rapid Commun.* **2007**, 28, 1776-1780.

(31) Swinnen, A.; Haeldermans, I.;Vande Ven, M.; D'Haen, J.; Vanhoyland, G.; Aresu, S.; D'Olieslaeger, M.; Manca, J. *Adv. Funct. Mater.* **2006**, 16, 760-765.

(32) Campoy-Quiles, M.; Ferenzi, T.; Agosinelli, T.; Etchegoin, P. G.; Kim, Y.; Anthopoulos, T. D.; Stabrinou, P. N.; Bradley, D. C.; Nelson, J. *Nat. Mater.* **2008**, 7 , 158-164.

(33) Vanlaeke, P.; Swinnen, A.; Haeldermans, I.; Vanhoyland, G.; Aernouts, T.; Cheyns, D.; Deibel,C., D'Haen, J.; Heremans, P.; Poortmans, J.; Manca, J.V. *Solar Energy Materials and Solar Cells*. **2006,** 90, 2150-2158.

(34) Mihailetchi, V. D.; Xie, H.; de Boer, B.; Koster, L. J. A., Blom, P. W. M. *Adv. Funct. Mater.* **2006,** 16, 699-708.

(35) Thompson, B. C.; Kim, B. J.; Kavulak, D. F.; Sivula, K.; Mauldin, C.; Fréchet, J. M. J. *Macromolecules* **2007**, 40, 7425-7428.

(36) Zen, A.; Saphiannikova, M.; Neher, D.; Grenzer, J.; Grigorian, S.; Pietsch, U.; Asawapirom, U.; Janietz, S.; Scherf, U.; Lieberwirth, I.; Wegner, G. *Macromolecules* **2006**, 39, 2162-2171.

(37) Malik, S.; Nandi, A. K. *J. Poly. Sci. B* **2002**, 40, 2073-2085.

(38) Causin, V.; Marega, C.; Marigo, A.; Valentini, L.; Kenny, J. K. *Macromolecules* **2005,** *38*, 409-415.

(39) Swinnen, A.; Zhao, G.; Van Assche, D.; Vanderzande, D.; D'Olieslaeger, M.; Manca, J. V.; Van Mele, B. *Proc. SPIE,* **2007,** 6656, 665619.

(40) Defieuw, G.; Groeninckx, G.; Reynaers, H. *Polymer*, **1989**, 30, 2164-2169.

(41) Alamo, R. G.; London, J. D.; Mandelkern, L., Stehling, F. C.; Wignall, G. D. *Macromolecules*, **1994**, 27, 411-417.

(42) Chiu, H.; Chen, H. L.; Lin, J. S. *Polymer*, **2001**, 42, 5769-5754.

(43) Chen, T. A.; Wu, X.; Rieke, R. D. *J. Am. Chem. Soc.* **1995**, *117*, 233-244.

(44) Hummelen, J. C.; Knight, B. W.; LePeq F.; Wudl, F.; Yao, J.; Wilkins, C. L. *J. Org. Chem.* **1995**, 60, 532-538.

Chapter 3

Modifying the Dielectric Properties of Conjugated Polymers for Improved Charge Separation

Abstract

A modified poly(3-hexylthiophene) (P3HT) derivative is used to examine the correlation between the dielectric constant of the active layer and charge separation efficiency in organic photovoltaics. 15CI, a poly(alkylthiophene) with a terminal camphoric imide moiety appended to the end of 15% of its alkyl chains, is designed to increase the dielectric constant of P3HT layers and thus improve charge separation in all-polymer solar cells. Incorporating 15CI with a dielectric constant of 5.6, almost twice that of P3HT, leads to improved performance over pure P3HT in bilayer all-polymer solar cells with CN-PPV as the acceptor. The higher efficiencies in the P3HT:15CI blend devices are attributed to the higher active layer dielectric constant which facilitates improved charge separation. An optimized device utilizing a 1:1 blend of P3HT:15CI shows a 42% increase in power conversion efficiency compared to a P3HT control device.

3.1 Introduction

Although OPVs have generated much interest due to their potential in the production of low-cost solution-processed solar cells,[1] state-of-the-art OPVs exhibit power conversion efficiencies (PCEs) of only 4-5%.[2] In contrast, their inorganic counterparts can produce PCEs well over 20%.[3] A major difference between inorganic and organic solar cells is the dielectric constant (ε) of the semiconductor and this difference leads to dramatically different photovoltaic operating mechanisms.[4] Inorganic semiconductors have a relatively high ε (typically > 10) and thus generate free charges directly upon photoexcitation.[5] On the other hand, organic semiconductors with a lower ε (~ 3) form strongly bound excitons.[6]

Due to the excitonic nature of organic semiconductors, charge generation in an OPV device must occur at a donor/acceptor interface via a two-step mechanism that involves the ultrafast separation of the exciton into an intermolecular bound radical pair, followed by a slower conversion to mobile carriers.[7] The driving force for this charge separation, i.e. ΔG_{CS}, is typically defined by the Weller equation, which includes critical terms such as the ionization potential of the donor and the electron affinity of the acceptor.[8] ΔG_{CS} is also known to be affected by the dielectric constant.[9, 10] Theoretical modeling suggests that increasing ε of the active layer can increase |ΔG| of charge dissociation as well as decrease |ΔG| of charge recombination, both of which would facilitate the generation of free charge carriers.[11] Experimental studies on photoinduced charger transfer in solution have also concluded that a higher ε solvent increases the stabilization of the charge separated species, leading to more facile charge separation.[9, 12] These reports and others suggest the importance of ε in the active layer and how it might favorably influence OPV performance.[13]

Of particular interest are all-polymer OPVs, which suffer performance loss from a low charge separation efficiency. The smaller LUMO-LUMO offset between the donor and the acceptor typical of these devices leads to a reduced driving force for charge separation.[14] Mandoc *et al.* have also ascribed the poor charge dissociation efficiency in an all-polymer system to the lower ε of the polymer blend in comparison to polymer-fullerene composites, which benefits from the high polarizability of the fullerene.[15] Therefore, increasing the dielectric constant of the active layer may be particularly useful in facilitating charge separation in all-polymer OPVs by increasing the |ΔG| of charge separation and/or reducing recombination losses through the stabilization of separated charges.

3.2 Results and Discussion

Camphoric anhydride has been used as a dopant to increase ε of a polystyrene film.[16] In this Chapter, we describe a newly synthesized poly(3-hexylthiophene) (P3HT) substituted with camphor imide (CI) moieties and its use as the donor in all-polymer OPVs. The dielectric, optical and thermal properties of the CI-modified polymer and its increased performance in solar cells are shown as a function of % CI incorporation. We report the first systematic experimental study of the effect of increasing the dielectric constant of a conjugated polymer and establish a correlation between the dielectric constant and OPV device operation.

The CI-modified P3HT (Figure 3.1a) was prepared by copolymerizing 2,5-dibromo-3-hexylthiophene and the CI-appended thiophene monomer at a controlled ratio via a Grignard metathesis (GRIM) polymerization (see Scheme 3.1). The concentration of CI-modified unit in the final polymer after purification was determined to be ca. 15 mol% based on ^{1}H NMR analysis. A regioregular P3HT of similar M_n and PDI was polymerized via the same method as a control. Because the CI moiety is not conjugated to the backbone and does not absorb light, it should have minimal impact on the electronic structure of the polymer as confirmed by cyclic voltammetry measurements (See Figure 3.6). This material choice and design strategy aims to more easily attribute changes in device performance to the influence of ε.

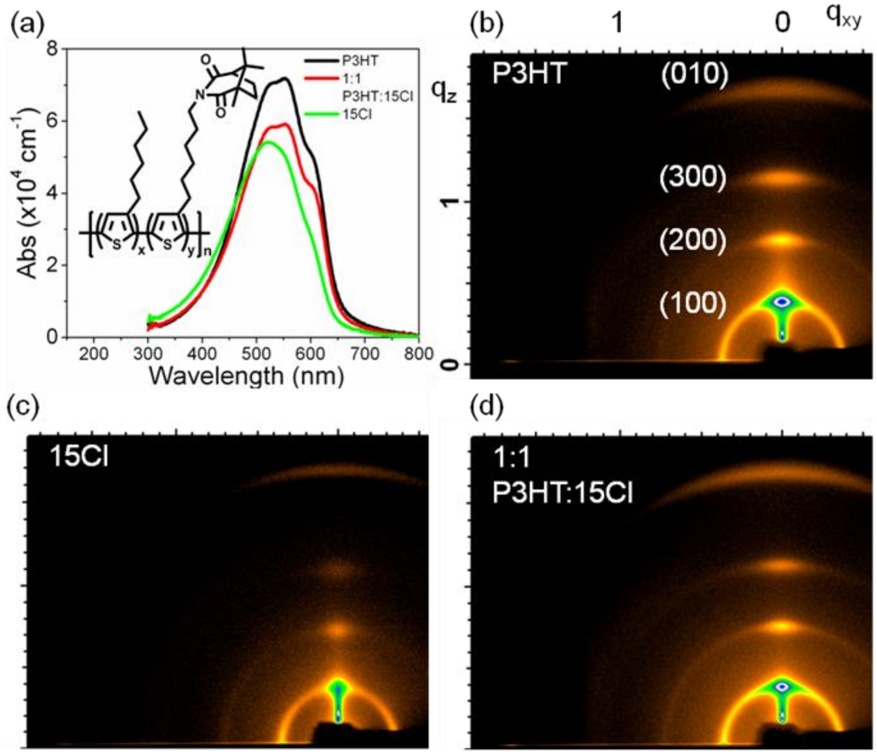

Figure 3.1. (a) Absorption spectra of P3HT, 15CI, and a 1:1 P3HT:15CI blend. (Inset) The structure of 15CI where x = 0.85 and y = 0.15. GIXS patterns from thin films of (b) P3HT, (c) 15CI, and (d) 1:1 P3HT:15CI.

Although the electronic structure of P3HT is largely preserved in 15CI, adding the CI group leads to changes in the solid state optical properties. As shown in Figure 3.1a, the thin film absorption of 15CI is reduced in intensity and blue-shifted from that of P3HT. Moreover, vibronic structures seen at 560 nm and 620 nm, which are indicative of crystalline packing,[17] are clearly visible in the P3HT spectrum and absent in the 15CI spectrum. The changes in absorption are most likely a consequence of appending the bulky CI unit, which leads to the disruption of the solid-state packing of the thiophene backbone. A film blend consisting of a 1:1 ratio by weight of P3HT and 15CI has an absorption higher than that of 15CI but lower than P3HT. More importantly, the vibronic structures are again visible in the blend, suggesting that the crystallinity of P3HT is largely retained upon blending.

A comparison of the two dimensional grazing incidence X-ray scattering (GIXS).patterns of Figures 3.1b and 3.1c shows that 15CI has much weaker diffraction peaks than P3HT. Differential scanning calorimetry (DSC) data supports the lower crystallinity finding for 15CI as evidenced by a reduced crystallization peak (see Figure 3.7 for DSC data). In contrast, the diffraction peaks of the 1:1 P3HT:15CI blend are more comparable in intensity to those for

P3HT (Fig.3.1b & 3.1d), This is again confirmed by DSC data of the blend sample, which shows thermal properties similar to P3HT.

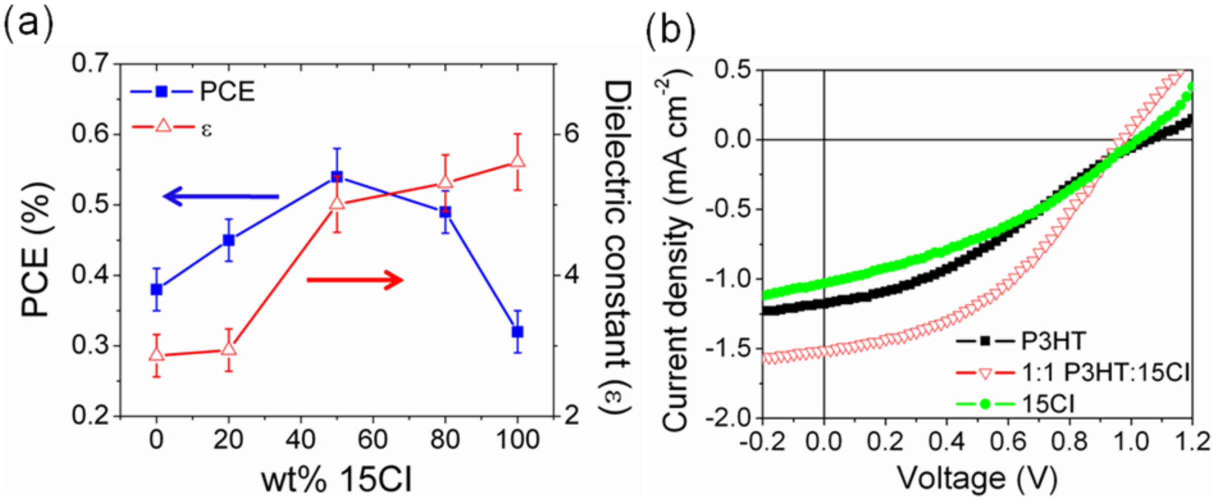

Figure 3.2. (a) PCE of bilayer solar cells and the dielectric constant (ε) of the polymer as a function of wt% 15CI blended into P3HT. (b) *I-V* curves of the best bilayer devices fabricated from P3HT, 15CI, and a 1:1 blend as the donor layer with CN-PPV as the acceptor.

The dielectric constant of P3HT, was determined to be 2.9 ± 0.3 at 1000Hz (see Figure 3.2 and Figure 3.5), consistent with literature values.[18] The higher capacitance of the 15CI results in a larger ε value (5.6 ± 0.4 at 1000Hz) nearly twice that of P3HT. The dielectric constants of blend films made from three different ratios of P3HT and 15CI (4:1, 1:1, 1:4) were also measured. Figure 3.2a illustrates the trend of increasing ε in blends that contain a higher wt% of 15CI.

Solution processed all-polymer bilayer solar cells were fabricated using either P3HT, 15CI or a blend of the two as the donor layer and a separate top layer of poly[2-methoxy-5-(2'-ethylhexyloxy)-1,4-(1-cyanovinylene)phenylene] (CN-PPV) as the acceptor. The device architecture consisted of ITO/ PEDOT:PSS/ P3HT:15CI (40 nm)/ CN-PPV (40 nm)/ LiF/ Al. The bilayer architecture was chosen to allow the investigation of fundamental properties of the separate donor and acceptor layers without the complications of morphology introduced in a bulk heterojunction device. As shown in Figure 3.2, the performance of pure 15CI/CN-PPV bilayer devices (average PCE = 0.32%) is slightly lower than that of P3HT/CN-PPV devices (average PCE = 0.38%). The main difference is the photocurrent, where the 15CI/ CN-PPV devices have a lower average short circuit current (J_{sc}) of 1.03 mA cm^{-2} compared to the P3HT/ CN-PPV devices with an average J_{sc} of 1.24 mA cm^{-2}. This decrease is likely due to the losses in absorption and crystallinity shown for 15CI.

Bilayer devices made from blend films of P3HT and 15CI showed improved performance with higher J_{sc}, FF and overall PCE compared to either homo-polymer (See Table 3.3 for device parameters). In Figure 3.2b, the *I-V* curves of the best devices fabricated from P3HT, 15CI and a 1:1 blend illustrate that devices from the 1:1 blend show both enhanced photocurrent (J_{sc} = 1.51 mA cm^{-2}) and an improved PCE of 0.54%. In order to eliminate the possibility of differences in interfacial areas between the various donor layers and the CNPPV acceptor layer, AFM images of the donor layer before and after solvent washing were recorded and the RMS roughness of all samples were comparable (See Figure 3.8 and Table 3.4). Because the absorption and solid state packing of the blends are not superior to pure P3HT, the improvement in device efficiency is attributed to the larger ε resulting from incorporation of 15CI. The increased J_{sc} and FF strongly suggest that charge separation is more efficient at the D/A interface in these films. The improved separation efficiency is likely due to the higher ε of the active layer leading to a larger ΔG_{CS} which assists in the dissociation of excitons and/or bound radical pairs. The improvement could also be due to the stabilization of charge separated species by the surrounding dipoles, which can reduce recombination losses.

3.3 Conclusions

In conclusion, we have designed and synthesized a CI-modified polythiophene with a higher dielectric constant than P3HT. Although adding the CI moiety leads to reductions in absorption and chain packing in 15CI, these losses can be partially recovered in P3HT:15CI blend films while maintaining a higher dielectric constant. In all-polymer bilayer solar cells using CN-PPV as the acceptor, a blend of 15CI and P3HT as the donor layer leads to clear improvements in device performance. This enhancement is attributed to the higher active layer dielectric constant and subsequent stabilization of charge separated species as well as an increase in the $|\Delta G_{CS}|$ for more efficient charge separation.

3.4 Experimental

3.4.1 Synthetic Details

All chemicals were purchased from Aldrich and used without further purification unless stated otherwise. All reactions were performed under nitrogen in glassware that had been flame dried under vacuum. All compounds were characterized by ^{1}H NMR (400 MHz) and ^{13}C NMR (75 MHz) on a Bruker AVB 400 or AVQ 400. For polymer molecular weight determination, polymer samples were dissolved in HPLC grade dichlorobenzene at a concentration of 1 mg/ml. The solutions were briefly heated and then allowed to return to room temperature before filtering through a 0.2 μm PVDF filter. SEC was performed using HPLC grade dichlorobenzene at a flow rate of 0.8 μL/min on two 300 x 8 mm linear S SDV, 5 micron columns (Polymer Standards Services, USA Inc.) at 70ºC using a Waters (Milford, MA) 2690 separation module and a Waters 486 Tunable Absorption Detector monitored at 350 nm. The instrument was calibrated vs. polystyrene standards (1,050 – 135,000 g/mol) and data was analyzed using Millenium 3.2 software. GC/MS data was collected on an Agilent 7890A GC system fitted with an Agilent HP-5 chromatography column. Helium carrier gas at a flow rate of 2.2 mL/min was used as the mobile phase. The sample inlet was 250 °C and a pressure of 8.8 PSI was used to load the vaporized compounds onto the column at a split ratio of 50:1. The oven temperature was equilibrated at 50 °C for 30 seconds, and then a temperature program was run as follows. 50 °C for 1 minutes, ramp to 310 °C at 20 °C/min, hold at 310 °C for 10 minutes. Total run time is 24 minutes. An auxiliary heater is kept at 150 °C between the GC column and the Agilent 5975C VL MSD system, in order to keep the separated compounds from precipitating from the He carrier gas at the MSD system inlet. MS information was collected by the 5975C system and analyzed with the Agilent Chemstation software.

Scheme 3.1.

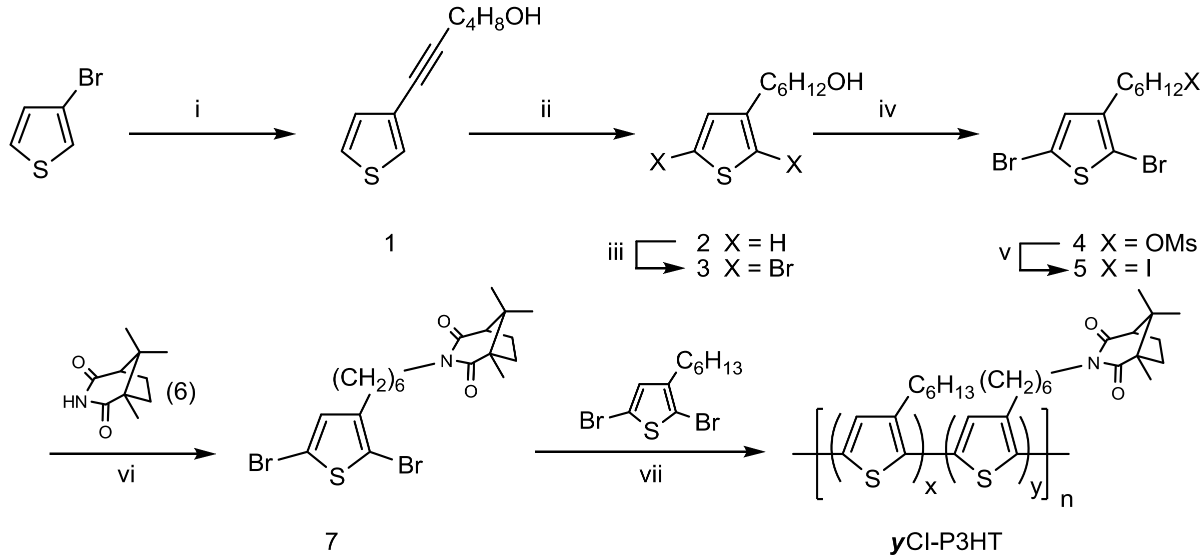

Reagents: i. $Pd(PPh_3)_4/CuI$, THF/Et_3N, 75%; ii. Pd/C, EtOH, 95%; iii. NBS, THF, 80%; iv. MsCl, Et_3N, DMAP, quant.; v. NaI, acetone, 90%; vi. Cs_2CO_3, THF, 75%; vii. 1)^{i}PrMgCl, LiCl, 2)Ni(dppp)Cl_2, 75%.

6-(Thiophen-3-yl)hex-5-yn-1-ol (**1**). A Schlenk flask was charged with 7.5 g of 3-bromothiophene (46.0 mmol), 5.0 g of hex-5-yn-1-ol (50.9 mmol) and 150 ml of THF/Et_3N (v/v, 3/2). The clear solution was degassed with argon for 15 min. Then $Pd(PPh_3)_4$ (1.5 g, 1.3 mmol, 3 mol%) and CuI (0.5 g, 2.7 mmol, 6 mol%) were added under the protection of argon. The resulting yellow solution was heated overnight at 80°C. The brownish suspension was filtered through a short plug of celite. After evaporation of the solvent, the residue was purified by flash chromatography on silica gel with ethyl acetate:hexane (1/2.5) to afford a light yellow oil (6.0 g, 75%). ^1H NMR ($CDCl_3$, δ_{ppm}): 7.32 (m, 1H), 7.22 (m, 1H), 7.04 (m, 1H), 3.68 (q, 2H), 2.43 (m, 2H), 1.69 (m, 4H), 1.34 (s, 1H). GC-MS: $t = 9.82$ min, $m/z = 180.0$.

6-(Thiophen-3-yl)hexan-1-ol (**2**). A mixture of 6-(Thiophen-3-yl)hex-5-yn-1-ol (6.0 g, 33.3 mmol) and 5% Pd on carbon (1.1 g, 20 wt%) in 200 ml ethanol was hydrogenated at room temperature under 100 psi H_2 for 36 hours. The mixture was then filtered through celite. After removal of the solvent, the product was isolated by vacuum distillation to afford a colorless oil (3.7 g, 95%). ^1H NMR ($CDCl_3$, δ_{ppm}): 7.23 (m, 1H), 6.92 (m, 2H), 3.63 (t, 2H), 2.63 (t, 2H), 1.67-1.52 (m, 4H), 1.42-1.27 (m, 5H). ^{13}C NMR ($CDCl_3$, δ_{ppm}):143.02, 128.22, 125.09, 119.81, 62.96, 32.67, 30.47, 30.16, 29.04, 25.54. GC-MS: $t = 8.89$ min, $m/z = 184.1$.

6-(2,5-Dibromothiophen-3-yl)hexan-1-ol (**3**). A solution of 6-(thiophen-3-yl)hexan-1-ol (3.7 g, 20.0 mmol) in 75 ml of THF was cooled to 0°C. N-bromosuccimide (7.4 g, 41.6 mmol) was added in one portion to the reaction. The resulting mixture was then allowed to warm to room temperature and stirred overnight. Then the reaction mixture was then added to 100 ml of water, and extracted with ethyl ether (150 ml x 2). The combined organic phases were dried over $MgSO_4$, and the solvent removed under reduced pressure. The light yellow residue was purified by flash chromatography on silica gel with ethyl acetate:hexane (1/3) to afford the product as a clear oil. (5.4g, 80%). ^{1}H NMR ($CDCl_3$, δ_{ppm}): 6.78 (s, 1H), 3.64 (t, 2H), 2.51 (t, 2H), 1.60-1.52 (m, 4H), 1.43-1.34 (m, 4H). GC-MS: t = 11.5 min, m/z = 341.9.

6-(2,5-Dibromothiophen-3-yl)hexyl methanesulfonate (**4**). A solution of 6-(2,5-Dibromothiophen-3-yl)hexan-1-ol (3.45 g, 10.0 mmol) in 75 ml of dry CH_2Cl_2 was added to Et_3N (1.7 ml, 12 mmol) and dimethylaminopyridine (244 mg, 20 mol%). Methanesulfonyl chloride (1.0 ml, 12.9 mmol) was then added dropwise to the reaction. After stirring at room temperature for 1 hour, the reaction mixture was added to 100 ml of water and extracted with CH_2Cl_2 (100 ml × 2). The organic phases were then combined and dried over $MgSO_4$. After solvent removal under reduced pressure, a yellow oil was obtained and used in the next reaction step without further purification. ^{1}H NMR ($CDCl_3$, δ_{ppm}): 6.77 (s, 1H), 4.22 (t, 2H), 3.02 (s, 3H), 2.51 (t, 2H), 1.79-1.72 (m, 2H), 1.60-1.52 (m, 2H), 1.47-1.31 (m, 4H).

2,5-Dibromo-3-(6-iodohexyl)thiophene (**5**). 6-(2,5-Dibromothiophen-3-yl)hexyl methanesulfonate (3.15 g, 7.5 mmol) and NaI (5.6 g, 5 equiv.) were combined in 75 ml of acetone. The resulting mixture was refluxed for 2 hours. After filtering through celite, the solution was concentrated and passed through a short plug of silica. After being diluted with CH_2Cl_2, the light purple solution was washed with saturated $Na_2S_2O_3$ (300 ml x 1). The colorless solution was then dried over $MgSO_4$ and the solvent removed under reduced pressure to afford the product as a colorless oil (3.4 g, 90%). ^{1}H NMR ($CDCl_3$, δ_{ppm}): 6.76 (s, 1H), 3.18 (t, 2H), 2.50 (t, 2H), 1.85-1.78 (m, 2H), 1.61-1.51 (m, 2H), 1.45-1.29 (m, 4H). ^{13}C NMR ($CDCl_3$, δ_{ppm}): 142.59, 130.86, 110.43, 108.06, 33.78, 33.32, 30.19, 29.32, 29.27, 27.91. GC-MS: t = 12.5 min, m/z = 451.9.

D,L-camphoric imide (**6**). An Erlenmeyer flask was charged with D, L-camphoric anhydride (5.89 g, 32.3 mmol), urea (2.33 g, 30.1 mmol) and a magnetic stir bar. The Erlenmeyer flask was then placed in a sand bath preheated to 230 °C. Bubbles were generated as both compounds melted and reacted. After 30 min, the heating source was removed. The crude product was then purified by recrystallization from water to afford an off-white solid (5.0 g, 85%). ^{1}H NMR ($CDCl_3$, δ_{ppm}): 7.89 (s, 1H, NH), 2.60 (d, 1H), 2.28-2.16 (m, 1H), 2.04-1.78 (m, 3H), 1.17 (s, 3H), 1.03 (d, 6H). GC-MS: t = 8.5 min, m/z = 181.1.

Monomer (**7**). Camphoric imide (1.25 g, 6.9 mmol) was dissolved in 25 ml of anhydrous THF. Cs_2CO_3 (2.15 g, 6.6 mmol) was added to the solution in one portion. The resulting white suspension was stirred at room temperature for 1 hour. Then a solution of 2,5-Dibromo-3-(6-iodohexyl)thiophene (1.36 g, 3 mmol) in 5 ml of THF was added dropwise to the reaction, followed by the addition of tetrabutylammonium iodide (1.22 g, 3.3 mmol). After stirring at 65°C for 24 hours, the reaction mixture was poured into 100 ml of water. The aqueous phase was extracted with ethyl acetate (150 ml × 2) and dried over $MgSO_4$. After removal of the solvent, the crude product was purified by flash chromatography on silica gel with ethyl acetate:hexane (1:9) to afford the product as a colorless oil (1.1 g, 75%). ^{1}H NMR ($CDCl_3$, δ_{ppm}): 6.76 (s, 1H), 3.63 (t, 2H), 2.68 (d, 1H), 2.48 (t, 2H), 2.22-2.14 (m, 1H), 1.94-1.87 (m, 2H), 1.76-1.69 (m, 1H), 1.52-1.47 (m, 4H), 1.22-1.16 (m, 4H), 1.04 (s, 3H), 0.95 (d, 6H). ^{13}C NMR ($CDCl_3$, δ_{ppm}): 178.29, 176.34, 142.73, 130.87, 110.28, 107.94, 56.58, 54.36, 44.12, 39.23, 34.20, 29.34, 29.30, 28.63, 27.40, 26.69, 25.28, 21.93, 19.22, 14.05. GC-MS: $t = 16.4$ min, $m/z = 426.1$ (M^+-Br)

Polymerization. A three-necked round bottom flask was charged with monomer **7** (0.18 g, 0.35 mmol), 2,5-dibromo-3-hexylthiophene (0.64 g, 1.95 mmol) and anhydrous LiCl (0.11 g, 2.56 mmol). The resulting solution was cooled to -78°C and stirred for 30 min. Then ^{i}PrMgCl (2 M in THF, 1.1 ml, 2.2 mmol) was added to the reaction mixture dropwise. After stirring at -78°C for 30 min, the reaction was transferred in to an ice/water bath (< 5°C) and stirred for an additional hour. Then Ni(dppp)Cl_2 (3.5 mg, 6.5 µmol, 0.3 mol%) was added in one portion. Following the addition of Ni(dppp)Cl_2, the color of the reaction mixture changed from colorless to red. The reaction was then heated at reflux for 12 hours. The polymer was precipitated into methanol (500 ml) from THF and filtered into a Soxhlet thimble and extracted with methanol for 12 h, followed by hexanes for 12 h. The polymer was then isolated by extraction with chloroform, followed by concentration and finally precipitation into methanol (500 ml). The control polymer (P3HT) was synthesized using a similar procedure without LiCl. A typical yield of ~ 75% was obtained for these polymerizations.

Table 3.1. Molecular weight and PDI of polymers used in present study measured by SEC. Regioregularity (RR) is determined by ^{1}H NMR.

polymer	M_n (g/mol)	PDI	RR
P3HT	32,000	1.1	96%
15CI	24,000	1.2	> 90%

3.4.2 Optical and Electronic Characterization of Polymers

Cyclic voltammograms were collected using a Solartron 1285 potentiostat under the control of CorrWare II software. A standard three electrode cell based on a Pt button working electrode, a silver wire pseudo reference electrode (calibrated vs. Fc/Fc+), and a Pt wire counter electrode was purged with nitrogen and maintained under a nitrogen atmosphere during all measurements. Acetonitrile was distilled over CaH_2 prior to use and tetrabutyl ammonium hexafluorophosphate (0.1 M) was used as the supporting electrolyte. Polymer films were drop cast onto a Pt button working electrode from a 1% (w/w) chloroform solution and dried under nitrogen prior to measurement.

UV-Visible absorption spectra were obtained using a Carey 50 Conc UV-Visible spectrophotometer. For thin film measurements polymers were spin coated onto untreated glass slides from chlorobenzene solution (10 mg/ml). A model P6700 Spincoater was used to spin coat the films at 1200 RPM for 60 s.

Photoluminescence (PL) spectra were collected using a Horiba Jobin Yvon NanoLog. Samples were prepared under identical conditions as photovoltaic devices. Polymers were spin coated onto clean glass slides from chlorobenzene solution at 10 mg/ml concentration. CN-PPV was deposited subsequently on top from spin coating an ethyl acetate solution at 8 mg/ml concentration as a quenching layer. Samples were excited at 600 nm where CN-PPV does not absorb so that only the PL of P3HT was observed. The PL intensity of sample films with and without CN-PPV were compared to calculate the extent of quenching.

Polymer mobility was measured using a diode configuration of ITO/ PEDOT:PSS/ Polymer/ Al in the space charge limited current (SCLC) regime. At sufficient potential the conduction of charges in the device can be described by

$$J_{SCLC} = \frac{9}{8}\varepsilon\varepsilon_o\mu\frac{V^2}{L^3}, \qquad (1)$$

where ε_0 is the permittivity of free space, ε is the dielectric constant of the polymer, μ is the mobility of the majority charge carriers, V is the potential across the device ($V = V_{applied} - V_{bi} - V_r$), and L is the polymer layer thickness. The series and contact resistance of the device (~15 Ω) was measured using a blank device (ITO/ PEDOT:PSS/ Al) and the voltage drop due to this resistance (V_r) was subtracted from the applied voltage. The built-in voltage (V_{bi}), which is based on the relative work function difference of the two electrodes, was also subtracted from the applied voltage. The built-in voltage can be determined from the transition between the Ohmic region and the SCLC region and was found to be about 1 V. Polymer film thickness was measured by a Veeco Dektak profilometer.

Table 3.2. SCLC mobility of polymers used in present study

Polymer	μ ($cm^2 V^{-1} s^{-1}$)
P3HT	1 e -3
15CI	1 e -4
1:1 P3HT:15CI blend	2 e -4

Differential Scanning Calorimetry (DSC) measurements were performed on a TA instrument DSC Q200. The samples (~5 mg) were heated from 40°C to 260°C at a heating rate of 10°C min^{-1} under N_2 atmosphere. Samples were prepared by drop casting a 30mg/ml CB solution onto the DSC pan and letting the solvent slowly evaporate under Argon atmosphere before DSC measurements.

Grazing-Incidence X-ray Scattering (GIXS) experiments were conducted at the Stanford Synchrotron Radiation Laboratory on beamline 11-3. The sample was irradiated at a fixed incident angle on the order of 0.1° and the GIXS patterns were recorded with a 2-D image detector (MAR345 image plate detector). GIXS patterns were recorded with an X-ray energy of 12.72 keV (λ = 0.975 Å). To maximize the intensity from polymer sample, the incident angle (~0.1°-0.12°) was carefully chosen so that the X-ray beam penetrates the polymer sample completely but not the silicon substrate. Typical exposure times were 90-180 s. To produce identical surface condition as samples for device fabrication, a thin layer (20-30 nm) of PEDOT:PSS was spun onto silicon substrates with a native oxide. Then the GIXS samples were prepared by spin-coating the same polymer solutions used for making devices onto silicon substrates at 1200 RPM for 60 s. The substrates were placed directly on top of hot plates under Argon for 3 hours of thermal annealing at 150°C before data acquisition.

The dielectric constant of a polymer film was determined by impedance spectroscopy. Diode-like devices were fabricated with the structure ITO/ PEDOT:PSS/ polymer/ Al. The complex impedance of the device was measured using a Solartron SI 1260 impedance analyzer by applying an oscillating voltage of 100 mV. The measurement was performed in the dark at ambient conditions at a range of frequencies from 10 MHz to 10 Hz. The equivalent circuit in Figure 3.4 was used, with a capacitance C, a parallel resistance R_p, a series resistance R_s to model the data. The capacitance (C) was used to calculate the dielectric constant of the polymer film by:

$$\varepsilon = \frac{Cd}{\varepsilon_0 A} \tag{2}$$

where d is the thickness of the film, ε_0 is the permittivity of free space, and A is the area of the electrode. Thicknesses of polymer films were ~ 60-70 nm, and the electrode area was 1 cm^2.

3.4.3 Photovoltaic Device Fabrication

All devices have a layered structure with the photoactive layer consisting of separate donor and acceptor layers sandwiched between the two electrodes, ITO and LiF/Al. Glass substrates coated with a 150nm sputtered ITO pattern of 20 $\Omega\ \square^{-1}$ resistivity were obtained from Thin Film Device, Inc. The ITO-coated glass substrates were ultrasonicated for 20 min each in acetone, and then 2 % Helmanex soap water, followed by extensive rinsing and ultrasonication in deionized water, and then isopropyl alcohol. The substrates were then dried under a stream of air. A dispersion of PEDOT:PSS (Baytron PH500) in water was filtered (0.45 μm glass) and spin coated at 3400 RPM for 60 s, affording a ~20-30 nm layer. The substrates were dried for 15 min at 140^{o}C in air and then transferred into an Argon glove box for subsequent procedures. P3HT and 15CI solutions were prepared in chlorobenzene at a concentration of 10 mg/ml and were heated to 120^{o}C for complete dissolution. CN-PPV solution was prepared in ethyl acetate at a concentration of 8 mg/ml. Ethyl acetate was chosen as the solvent because it is a bad solvent for P3HT and this orthogonality afforded true bilayer devices. The solutions were stirred overnight and passed through a 0.2 μm PTFE syringe filer before they were spin coated. For blend solutions, different ratios of P3HT and 15CI solutions were mixed and stirred overnight at 120^{o}C before spin coating. The donor layer, consisting of P3HT or 15CI or a blend of the two, was spin coated first onto the substrate at 1200 RPM for 60 s on top of the PEDOT:PSS layer. Subsequently, the CN-PPV layer was spin coated on top of the donor layer at 2000 RPM for 60 s. The substrates was then placed in an evaporation chamber and pumped down in vacuum (~10^{-7} torr) before evaporating a 1 nm LiF layer and subsequently a 100 nm Al layer through a shadow mask on top of the photoactive layer. The configuration of the shadow mask afforded eight independent devices on each substrate, and each device has an active area of ~ 0.03 cm^2. The mechanical removal of part of the organic layer allowed contact with the ITO, and adding conductive Ag paste to the removed area to ensure electrical contact completed the device. Testing of the devices was performed under an argon atmosphere with an Oriel Xenon arc lamp with an AM 1.5G solar filter. Current–voltage behavior was measured with a Keithley 236 SMU. Eight devices were averaged for each condition.

3.4.4 Additional Data and Figures

Table 3.3. Average device parameters of P3HT:15CI/CN-PPV bilayer cells.

P3HT:15CI	**V_{oc}**	**J_{sc}**	**FF**	**PCE**
P3HT only	0.98	1.24	0.32	0.38% ± 0.02
4:1	0.97	1.31	0.36	0.45% ± 0.02
1:1	0.95	1.55	0.37	0.54% ± 0.05
1:4	1.00	1.36	0.36	0.49% ± 0.04
15CI only	0.97	1.03	0.32	0.32% ± 0.02

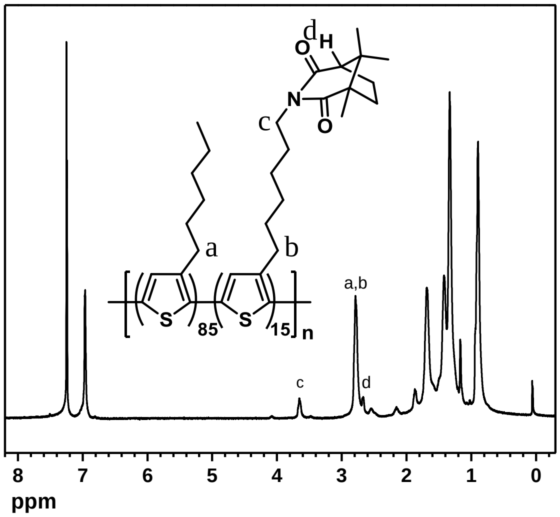

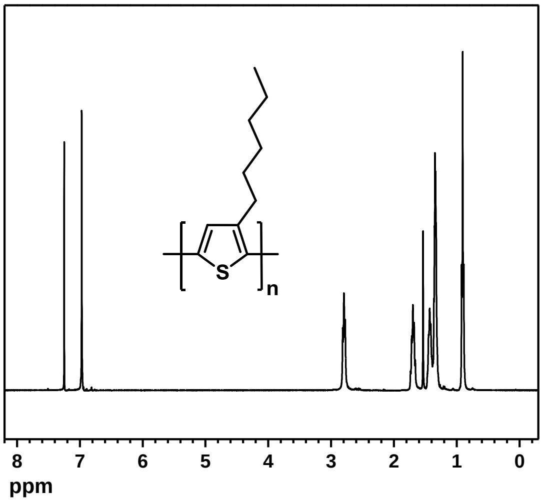

Figure 3.3. ^{1}H NMR spectra of 15CI (top) and P3HT (bottom) in $CDCl_3$.

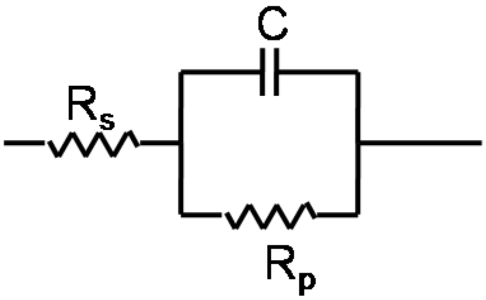

Figure 3.4. Equivalent circuit used to model the impedance spectroscopy data, with capacitance C, parallel resistance R_p, and series resistance R_s indicated in the figure.

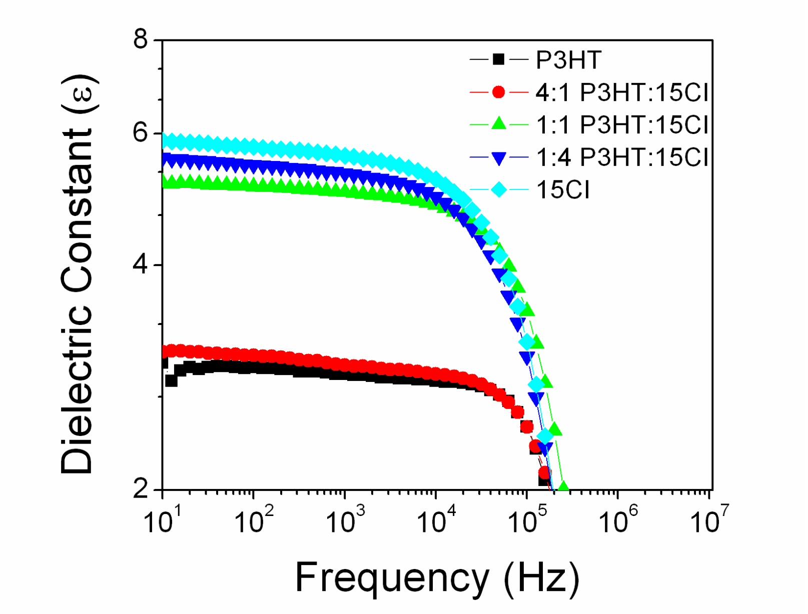

Figure 3.5. Dielectric constant (ε) of polymer films calculated from capacitance as a function of the frequency of the oscillating voltage.

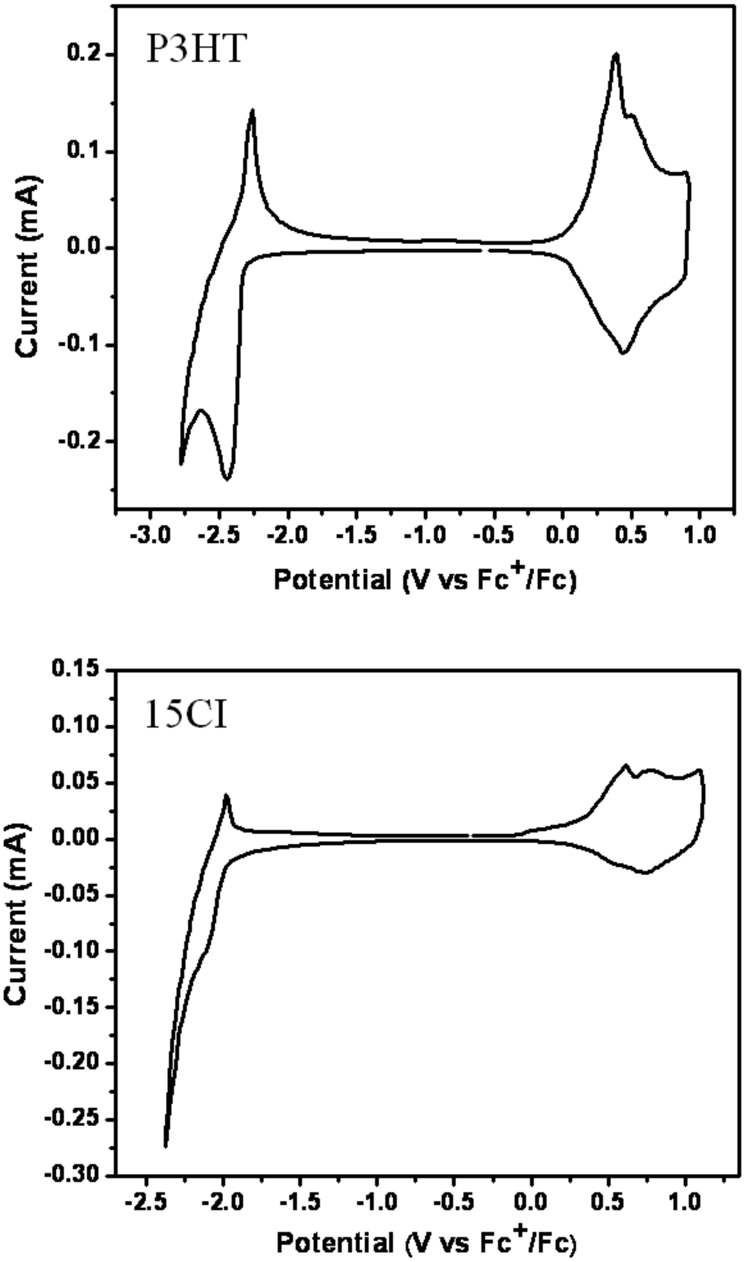

Figure 3.6. Cyclic voltammograms (CV) of P3HT (top) and 15CI (bottom) films on a platinum electrode (0.1 M Bu_4NBF_4 in CH_3CN). Ferrocene was used as the internal standard, scan rate: 100 mV/s. The HOMO and LUMO energy levels are calculated from the onset of oxidation and reduction potentials relative to ferrocene. For P3HT they are 0.2 eV and -2.2 eV respectively, and for 15CI they are 0.3 eV and -2.1 eV respectively.

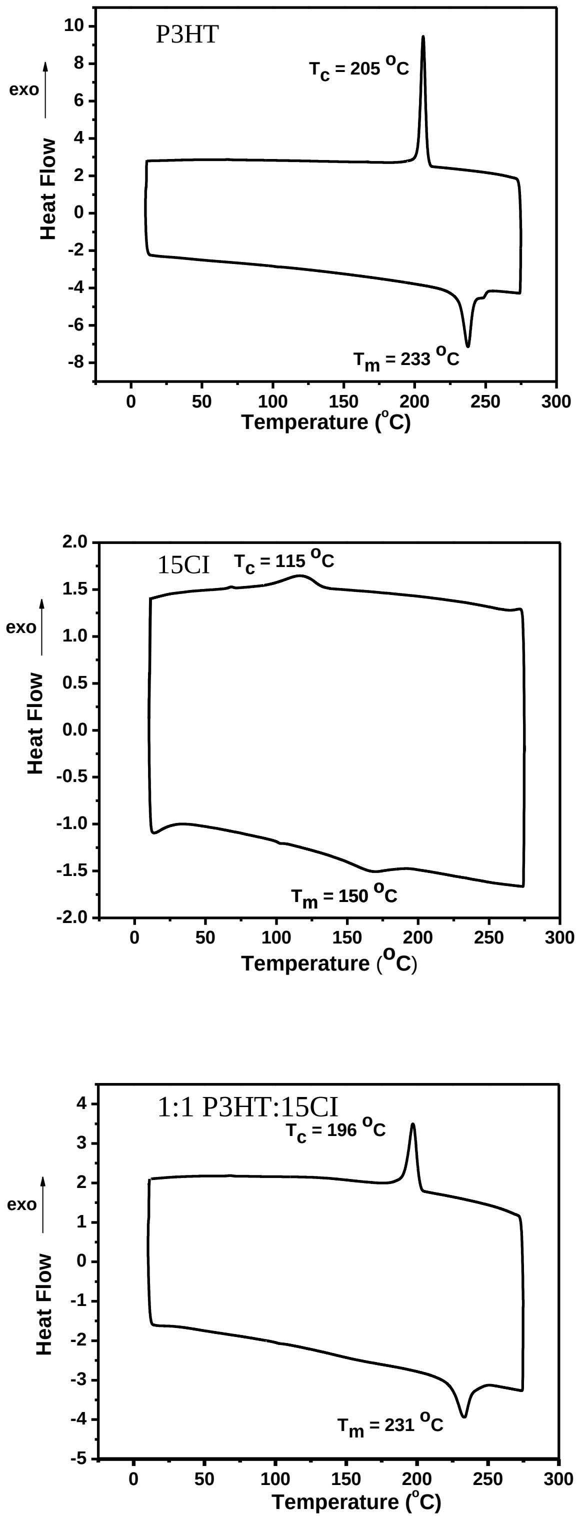

Figure 3.7. Second cycles of DSC scans for P3HT, 15CI, and 1:1 blend of P3HT:15CI.

To study the extent of D/A interfacial mixing in the bilayer devices, the surface topography of the donor polymer films spin coated on PEDOT coated ITO glass substrates before and after ethyl acetate (EtAc) washing was studied. Topographical images were obtained using a Veeco Multimode V Atomic Force Microscope (AFM) in tapping mode.

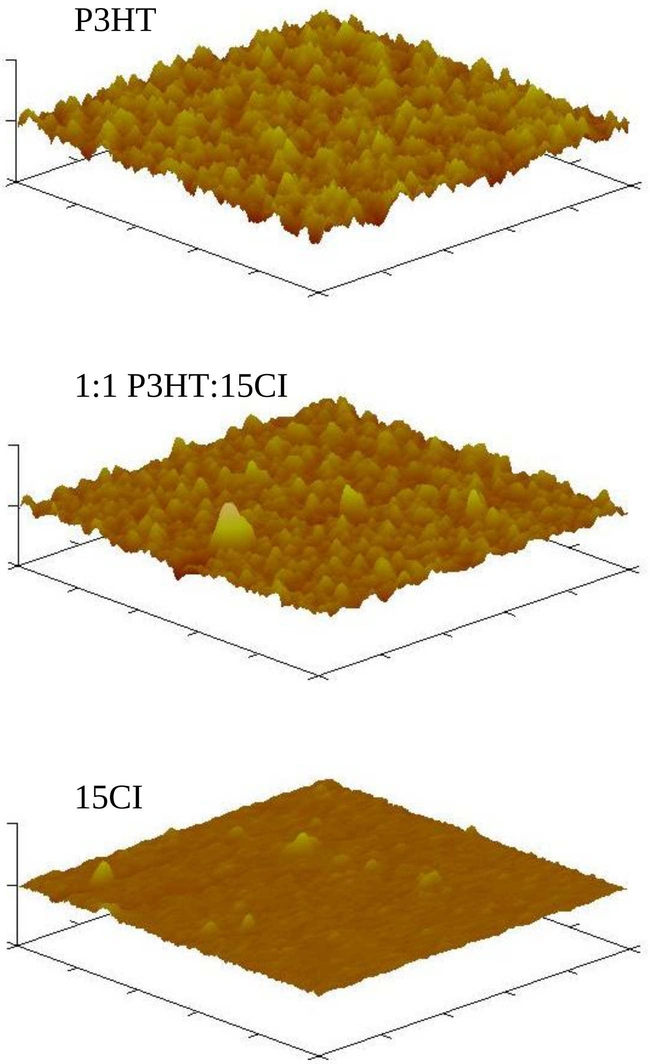

Figure 3.8. AFM tapping mode images of P3HT, 1:1 P3HT:15CI blend and 15CI films after ethyl acetate wash. Vertical divisions are 10 nm each. Horizontal divisions are 1 μm each.

Table 3.4. Average RMS roughness of polymer films taken on two 5 μm x 5 μm areas.

	As spun (nm)	After EtAc wash (nm)
P3HT	3.0	4.3
1:1 P3HT:15CI	2.3	2.8
15CI	1.0	1.4

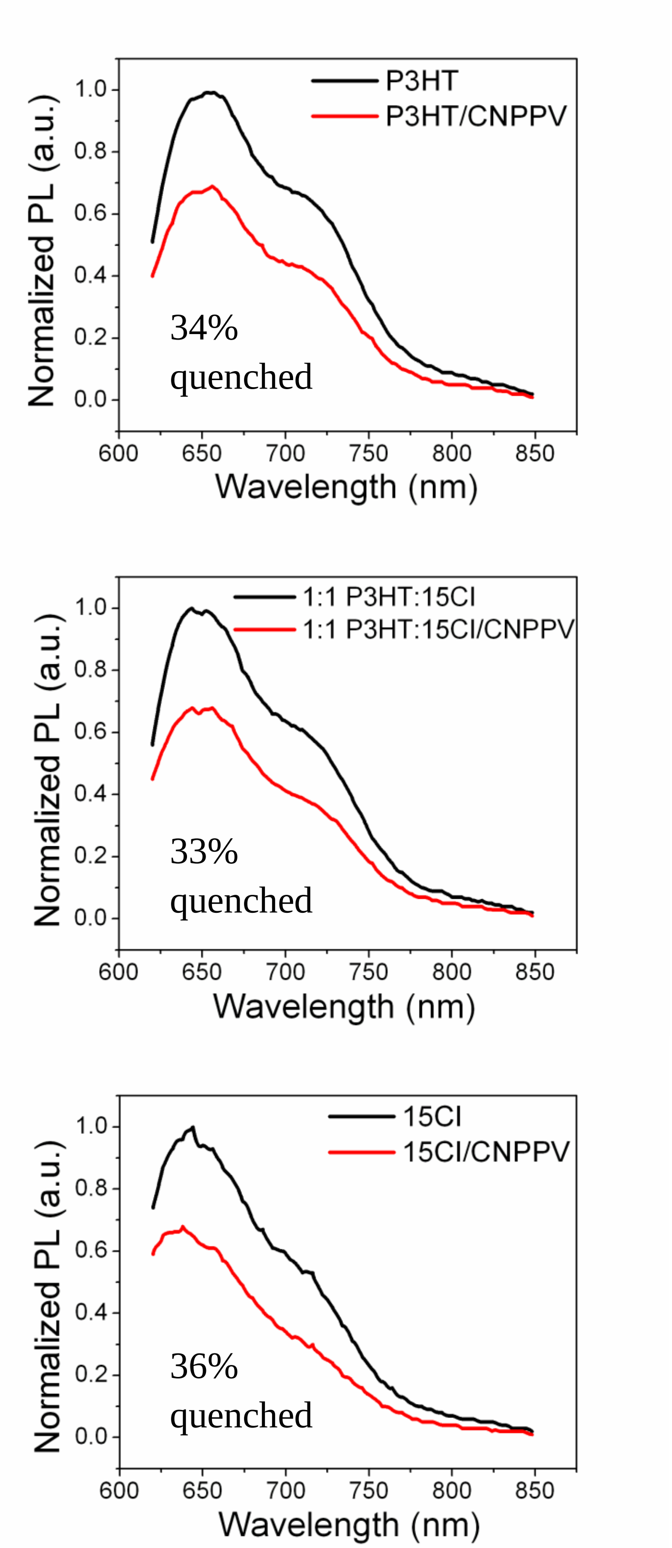

Figure 3.9. Normalized photoluminescence spectra of neat polymers films and bilayers with CN-PPV.

3.5 References

(1) (a) Gunes, S.; Neugebauer, H.; Sariciftci, N. S. *Chem. Rev.* **2007**, *107*, 1324-1338. (b) Thompson, B. C.; Fréchet, J. M. J. *Angew. Chem., Int. Ed.* **2008**, *47*, 58-77.

(2) (a) Peet, J.; Kim, J. Y.; Coates, N. E.; Ma, W. L.; Moses, D.; Heeger, A. J.; Bazan, G. C. *Nat. Mater.* **2007**, *6*, 497-500. (b) Wienk, M. M.; Turbiez, M.; Gilot, J.; Janssen, R. A. J. *Adv. Mater.* **2008**, *20*, 2556-2560. (c) Hou, J.; Chen, H. Y.; Zhang, S.; Li, G.; Yang, Y. *J. Am. Chem. Soc.* **2008**, *130*, 16144-16145.

(3) Miles, R. W.; Zoppi, G.; Forbes, I. *Materials Today* **2007**, *10*, 20-27.

(4) Gregg, B. A.; Hanna, M. C. *J. Appl. Phys.* **2003**, *93*, 3605-3614.

(5) Kittel, C. *Introduction to Solid State Physics*; Wiley & Sons: 2005.

(6) Offermans, T.; Meskers, S. C. J.; Janssen, R. A. J. *J. Chem. Phys.* **2003**, *119*, 10924-10929.

(7) (a) Ohkita, H.; Cook, S.; Astuti, Y.; Duffy, W.; Tierney, S.; Zhang, W.; Heeney, M.; McCulloch, I.; Nelson, J.; Bradley, D. D. C.; Durrant, J. R. *J. Am. Chem. Soc.* **2008**, *130*, 3030-3042. (b) Clarke, T.M.; Ballantyne, A. M.; Nelson, J.; Bradley, D. D. C.; Durrant, J. R. *Adv. Funct. Mater.* **2008**, *18*, 4029-4035.

(8) Weller, A. *Z. Phys. Chem. Neue Folge* **1982**, *133*, 93.

(9) van Hal, P. A.; Janssen, R. A. J.; Lanzani, G.; Cerullo, G.; Zavelani-Rossi, M.; De Silvestri, S. *Phys. Rev. B* **2001**, *64*, 075206.

(10) Arkhipov, V. I.; Heremans, P.; Bassler, H. *Appl. Phys. Lett.* **2003**, *82*, 4605-4607.

(11) Lemaur, V.; Steel, M.; Beljonne, D.; Bredas, J. L.; Cornil, J. *J. Am. Chem. Soc.* **2005**, *127*, 6077-6086.

(12) Neuteboom, E. E.; Meskers, S. C. J.; Beckers, E. H. A.; Chopin, S.; Janssen, R. A. J. *J. Phys. Chem. A* **2006**, *110*, 12363-12371.

(13) (a) Sentein, C.; Rocha, L.; Apostoluk, A.; Raimond, P.; Duyssens, I.; Van Severen, I.; Cleij, T.; Lutsen, L.; Vanderzande, D.; Kazukauskas, V.; Pranaitis, M.; Cyras, V. *Sol. Energy Mater. Sol. Cells* **2007**, *91*, 1816-1824. (b) Van Severen, I.; Breselge, M.; Fourier, S.; Adriaensens, P.; Manca, J.; Lutsen, L.; Cleij, T. J.; Vanderzande, D. *Macromol. Chem. Phys.* **2007**, *208*, 196-206. (c) Mandoc, M. M.; Veurman, W.; Sweelssen, J.; Koetse, M. M.; Blom, P. W. M. *Appl. Phys. Lett.* **2007**, *91*, 073518-3.

(14) Westenhoff, S.; Howard, I. A.; Hodgkiss, J. M.; Kirov, K. R.; Bronstein, H. A.; Williams, C. K.; Greenham, N. C.; Friend, R. H. *J. Am. Chem. Soc.* **2008**, *130*, 13653-13658.

(15) Mandoc, M. M.; Veurman, W.; Koster, L. J. A.; de Boer, B.; Blom, P. W. M. *Adv. Funct. Mater.* **2007**, *17*, 2167-2173.

(16) Madigan, C. F.; Bulovic, V. *Phys. Rev. Lett.* **2003**, *91*, 247403.

(17) Yamamoto, T.; Komarudin, D.; Arai, M.; Lee, B. L.; Suganuma, H.; Asakawa, N.; Inoue, Y.; Kubota, K.; Sasaki, S.; Fukuda, T.; Matsuda, H. *J. Am. Chem. Soc.* **1998**, *120*, 2047-2058.

(18) Knipper, M.; Parisi, J.; Coakley, K.; Waldauf, C.; Brabec, C. J.; Dyakonov, V. *Zeitschrift fur Naturforschung Section A-A Journal of Physical Sciences* **2007**, *62*, 490-494.

(19) Jonscher, A. K. *Dielectric Relaxation in Solids*. Chelsea Dielectric Press: London, 1983.

Chapter 4

The Effect of Polymer Side Chain on Charge Separation – Steric Control of the Donor/Acceptor Interface in Non-Fullerene OPVs[2]

Abstract

The performance of OPV devices are currently limited by charge recombination at the donor/acceptor (D/A) interface, leading to low short-circuit current densities. Approaches toward improving charge transfer at the critical D/A interface may provide new avenues to advance OPV technologies and the basic science of charge transfer in organic semiconductors. A two-step charge separation process is an essential component of photocurrent generation in organic solar cells. This Chapter highlights how steric control of the charge-separation interface can be effectively tuned by changing the side chain of the donor polymer. This finding is of particular significance for non-fullerene OPVs, which have many potential advantages such as tunable energy levels and spectral breadth, but are prone to poor charge separation efficiency due to decreased symmetry and electron delocalization of non-fullerene electron acceptors. Computational, spectroscopic, and synthetic methods were combined to develop a structure-property relationship that correlates polymer substituents with charge-transfer state energies and, ultimately, device efficiency.

---

[2] Reproduced in part with permission from Holcombe, T. W.; Woo, C. H.; Kavulak, D. F. J.; , J. M. J. *Journal of the American Chemical Society* **2009**, *131*, 14160-14161. Copyright 2009 American Chemical Society and Woo, C. H.; Holcombe, T. W.; Unruh, D. A.; Sellinger, A.; , J. M. J. *Chemistry of Materials,* **2010**, *22*, 1673-1679. Copyright 2010 American Chemical Society.

4.1 Introduction

State-of-the-art OPV devices generally rely on soluble fullerene derivatives (e.g. $PC_{61}BM$ or $PC_{71}BM$) as both the electron acceptor and transporter.[1-3] Polymer:fullerene blends, termed bulk heterojunctions (BHJs), hold record efficiencies around 8%.[4] Although these devices have provided exceptional growth for the field of OPVs and have demonstrated rapid performance improvement over the past two decades, alternative n-type materials[5-7] and device architectures[8] could lead to break-through technological advances and fundamental understandings. Currently, the best non-fullerene OPV device efficiencies is *ca.* 2%, mostly limited by inefficient charge separation and low short-circuit current densities.[9-12] Therefore, to move beyond fullerene-based OPVs, a greater understanding of charge generation is critical.

Fullerenes provide several potential advantages over polymers and non-fullerene small molecules as electron acceptors in OPVs; they possess high molecular symmetry, are strongly polarizable, and present triply-degenerate LUMO levels.[13] On the other hand, conjugated polymers and planar small molecules are less symmetric, often have well-defined charge-transport axes,[14] and are generally not as highly polarizable – conjugated polymers have a dielectric constant of ca. 3[15] vs. fullerenes with a dielectric constant of ca. 4.[16] These properties of fullerenes generally facilitate charge separation and efficient charge extraction.

Charge separation in OPVs happens at the donor/acceptor interface, where the energy offset between the donor and the acceptor provides the thermodynamic driving force to separate the photoexcited state.[17-19] The abbreviated Weller Equation has been used to estimate the relative free energy of charge separation (ΔG_{CS}^{rel}) for several donor polymers combined with a fullerene acceptor: $\Delta G_{CS}^{rel} = E_s - |(HOMO_{donor} - LUMO_{acceptor})|$. The difference between the singlet excited state energy (E_s) of the donor polymer and the HOMO-LUMO offsets provided good agreement with measured short-circuit current (J_{sc}).[20] Although values for ΔG_{CS}^{rel} calculated from this equation loosely correlated with the observed J_{sc} for several devices,[20-22] many additional factors such as active layer absorption breadth, optical density and morphology, as well as charge-carrier mobility and electrode choice are all known to critically affect J_{sc}. Notably, the *abbreviated* Weller equation does not include the lattice polarization energy or Coulomb attraction terms, as these are not easily measured by any experimental methods.[23] To expanding our understanding of charge generation in OPVs, we must explore factors beyond the thermodynamics of charge separation as estimated from bulk electronic properties.

For instance, charge generation depends not only on the donor and acceptor material energy levels, but also on the specific molecular environment at the donor/acceptor (D/A) interface and on the kinetics of exciton separation/recombination.[18,23,24] Similar to a chemical reaction, exciton separation to yield free charges can proceed via more than one mechanism. In some cases, no “reaction” intermediates are observed, whereas in other cases there is an intermediate “geminate pair” or charge transfer (CT) state. Probing the parameters that control the mechanism of charge generation is of great importance to the field of OPVs.

Our work toward understanding charge generation originated from a structural point of view, and we drew inspiration from studies reported by Granstrom et al. in 1998.[25] In that study, poly[3-(4-n-octyl)-phenylthiophene] (POPT) was shown to produce the most photocurrent in any OPV device at the time, a notable achievement with the common electron acceptor material poly[2-methoxy-5-(2'-ethylhexyloxy)-1,4-(1-cyanovinylene)phenylene] (CNPPV). Motivated by that research, we compared the OPV performance of POPT and the prototypical semiconductor

P3HT[26,27] using four different non-fullerene acceptors, and we discovered that POPT consistently outperforms P3HT (see Figure 4.1 and 4.3 for molecular structures). [9,11] This was particularly surprisingly because POPT devices always generated higher short-circuit currents than P3HT devices despite the fact that POPT has a reduced optical density compared to P3HT. The main structural difference in these two polymers is the phenyl ring on POPT, and we suspected that the phenyl content of POPT played a critical role at the D/A interface, potentially facilitating geminate pair separation.

Based on the abbreviated Weller Equation, POPT is thermodynamically less likely to undergo exciton separation with a given acceptor, compared to P3HT. Thus, the considerably and recurrently higher J_{sc} prompted an in-depth investigation combining device fabrication, theoretical modeling, and advanced spectroscopy to gain insight into these systems. The following results exploit observed differences in performance caused by the presence of phenyl substituents to better understand the charge-separation process. By expanding this study to two different polymer backbones and four different acceptors, we aim to probe the universality of this design strategy for improving charge generation in non-fullerene OPVs. Structural control of the D/A interface may become a powerful tool for tuning charge separation dynamics.

4.2 Results

4.2.1 Polymer Characterization

POPT was polymerized from the 2-bromo-5-iodo-3-(4-n-octyl)thiophene monomer in ~50% final yield with a modified GRIM procedure. Due to the steric and electronic effects of the 3-phenyl ring, elevated metal-halogen exchange and polymerization temperatures were required to achieve suitable polymer yield and molecular weight. POPT with M_n up to 75 kDa and PDI < 1.1 was obtained after Soxhlet purification. The purified POPT was >99% RR as determined by NMR. All subsequent electronic and device characterization was performed with 35 kDa POPT (see Table 4.1). To have a fair comparison, we also synthesized P3HT via GRIM polymerization.

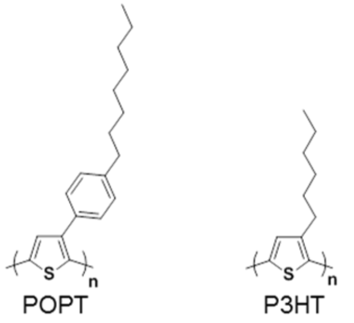

Figure 4.1. The molecular structures of POPT and P3HT.

Table 4.1. Characterizations of POPT and P3HT used in this study.

	M_n (g/mol)	PDI	RR	Absorption coefficient α at λ_{max} (x 10^4 cm^{-1})	μ_{hole} (cm^2/Vs)	HOMO (eV)	LUMO (eV)
POPT	35,000	1.09	99%	4.1	1 x 10^{-4}	5.5	3.2
P3HT	37,700	1.04	99%	8.1	1 x 10^{-4}	5.2	3.2

Both GRIM P3HT and POPT are highly regioregular (RR) and require heating to completely dissolve in chlorobenzene. The limited solubility of P3HT and POPT in other organic solvents enables the fabrication of bilayer solar cells using orthogonal solvents to deposit the acceptor layer on top of the spin-coated polymer layer. The solid state absorption spectra in Figure 4.2 show that POPT has a greater spectral breath with an absorption onset at 700 nm (1.8 eV) compared to 650 nm (1.9 eV) for P3HT. Typically, materials with a broad spectral breath and low optical band gap are desirable for OPV application as it indicates a greater potential for light absorption. However, one also needs to consider the optical density (i.e. the absorption coefficient) of a material. The solid state absorption coefficients α shown in Table 4.1 are measured by varying the polymer film thickness from 5 - 60 nm and examining the change in intensity of their absorption maximum λ_{max}. The α values are 8.1 x 10^4 cm^{-1} for P3HT and 4.1 x 10^4 cm^{-1} for POPT. The 50% reduction in optical density in POPT is likely due to the phenyl ring twisting out of plane from the thiophene backbone, which leads to increased spacing between the polymer backbones.[28] Therefore, despite having a lower optical band gap than P3HT, POPT actually has a lower potential to absorb light.

We have also determined, for the first time, mobility values of 1 x 10^{-4} cm^2/Vs and 0.05 cm^2/Vs for POPT using space-charge limited current and field effect transistor measurements, respectively. No change in mobility was observed upon thermal annealing. These mobility values are similar to those obtained for P3HT and suggest that hole extraction in OPV devices is not likely to differ much between these polythiophenes. The energy levels of the polymers as measured by cyclic voltammetry are also shown in Table 4.1. P3HT has a HOMO level of 5.2 eV, whereas POPT has a lower HOMO of 5.5 eV. Both polymers have a similar LUMO level of 3.2 eV.

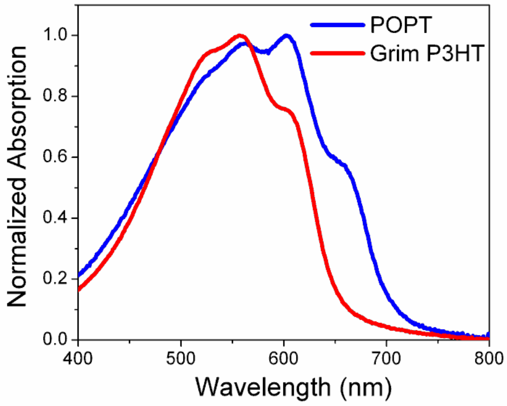

Figure 4.2. Normalized thin film absorption spectra of POPT and P3HT.

4.2.2 Solar Cell Comparison of POPT *vs.* P3HT

Four acceptors were utilized with POPT and P3HT in head-to-head comparisons: CNPPV, 4,7-bis(2-(1-(2-ethylhexyl)-4,5-dicyanoimidazol-2-yl)vinyl)benzo[c][1,2,5]-thiadiazole (EV-BT),[7] N-(1-hexylheptyl)-N'-(1-ethylpropyl)perylene-3,4,9,10-tetracarboxylic diimide (PDI),[29] and poly{[*N*,*N*'-bis(2-octyldodecyl)-naphthalene-1,4,5,8-bis(dicarboximide)-2,6-diyl]-alt-5,5'-(2,2'-bithiophene) (Polyera ActiveInk™ N2200)[30] (structures shown in Figure 4.3a). In most cases, both bilayer and bulk heterojunction devices were compared, provided that an orthogonal solvent system was found to allow the fabrication of bilayers. Polymer-polymer solar cells performed better in the bilayer device architecture, whereas polymer-small molecule solar cells were better in the bulk heterojunction architecture. Table 4.2 and Figure 4.3 summarize the device results.

Table 4.2. Device parameters of POPT vs. P3HT devices; maximum efficiencies for optimized device systems. Symbol '/' indicates a bilayer device while symbol ':' indicates a BHJ device.

Device Active Layer	J_{sc} (mA/cm^2)	V_{oc} (V)	*FF*	PCE (%)
POPT/CNPPV	-5.44	1.06	0.35	2.00
P3HT/CNPPV	-2.63	1.08	0.33	0.93
POPT:EV-BT	-5.70	0.62	0.40	1.41
P3HT:EV-BT	-2.81	0.77	0.51	1.11
POPT/N2200	-2.50	0.52	0.47	0.61
P3HT/N2200	-0.80	0.46	0.46	0.17
POPT:PDI	-5.70	0.24	0.37	0.51
P3HT:PDI	-1.70	0.57	0.41	0.39

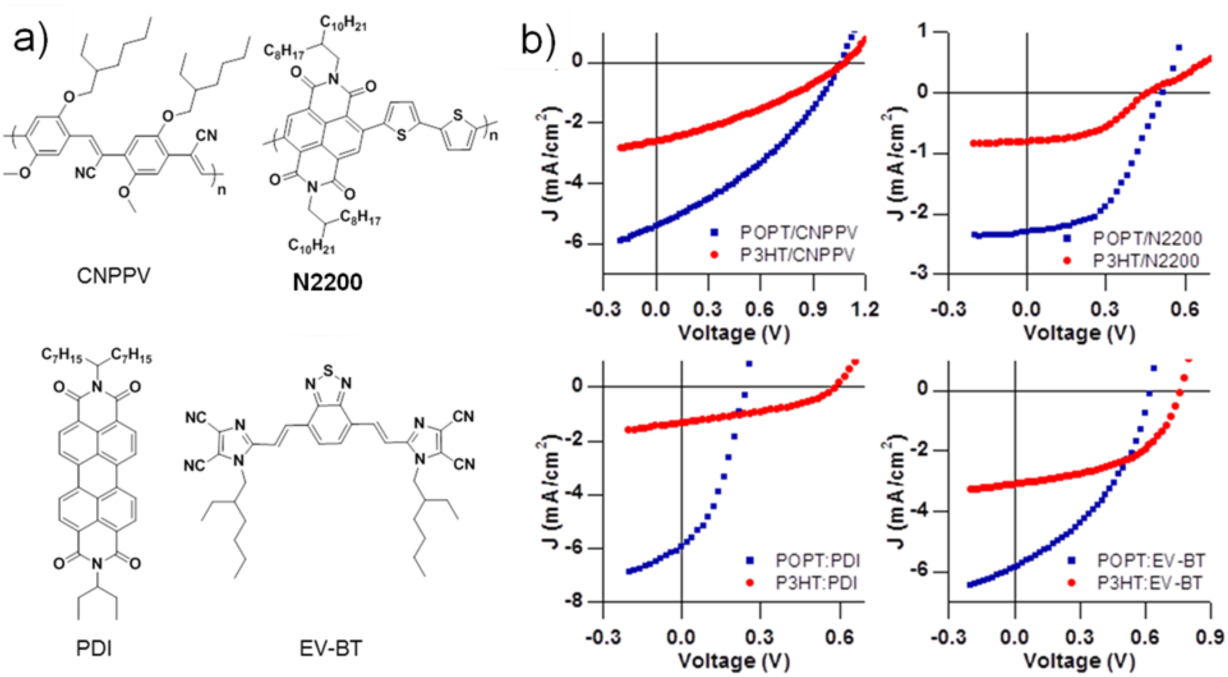

Figure 4.3. (a) The structures of four different acceptors (two polymers: CNPPV, N2200 and two small molecules: PDI, EV-BT) that are tested in a head-to-head comparison between P3HT and POPT. (b) *J-V* curves for the devices corresponding to the acceptor components in (a).

The relatively high solvent resistance of POPT resulting from its high M_n and regioregularity enables a better examination of the all-polymer system first explored by Friend.[25] Therefore, CNPPV can be spin-coated directly on top of a POPT film using the solvent tetrahydrofuran which does not dissolve POPT, leading to bilayer devices. A peak efficiency of 2.0% was achieved with this system after 2 hrs of thermal annealing at 110°C (average η =

1.5%). This constitutes the highest reported efficiency to date for a solution processed all-polymer OPV.[31-33] Significantly, similar all-polymer devices optimized from P3HT yielded a max efficiency of 0.93% with an average of 0.75%. This lower efficiency is due to a reduction in J_{sc}. The increased J_{sc} exhibited by the POPT/CNPPV devices does not derive from increased absorption. Under optimized conditions, the POPT/CNPPV bilayer absorbs less light but exhibits about twice the photocurrent of the P3HT/CNPPV bilayers with improved photocurrent across the entire absorption spectrum of the device.

For the acceptor EV-BT, both bilayer and BHJ devices were fabricated. Bilayer devices had the architecture: ITO/ PEDOT:PSS (30 nm)/POPT or P3HT (40nm)/ EV-BT (40 nm)/ LiF (1 nm)/ Al (100 nm). Upon annealing at 80°C for 20 min, the POPT devices reach an average efficiency of 0.97%, which is more than twice that of P3HT devices with an average of 0.43%. The higher efficiency of the POPT device originates from an improvement in the photocurrent as J_{sc} is 4.0 mA cm^{-2} compared to only 1.7 mA cm^{-2} for the P3HT device. BHJ devices were optimized by varying annealing conditions, device thickness, and the ratio of polymer to EV-BT. The optimal device thickness is *ca.* 100 nm for both systems and the optimal ratio of polymer to EV-BT was 1:1 by weight with the following device structure: ITO/ PEDOT:PSS/polymer:EV-BT/ LiF/ Al. After independent optimization, POPT:EV-BT devices exhibit an average efficiency of 1.4% after 40 min of annealing at 80°C, which is slightly superior to that of P3HT:EV-BT devices with an efficiency of 1.1%. The POPT device shows a clearly improved J_{sc} over the P3HT devices but its V_{oc} is lower than that of the P3HT device.

Similarly, for the acceptors N2200 and PDI, POPT devices displayed superior performance over P3HT devices. It should be noted that the P3HT/N2200 device results are consistent with two recent reports that demonstrated N2200 in a BHJ device with P3HT yields ~0.2% efficiency.[34,35] Therefore, based on individually optimized devices in all four comparisons, POPT consistently outperforms P3HT. While the V_{oc} and *FF* of the POPT and P3HT devices are comparable in most cases, the J_{sc} of POPT devices are at least twice those of P3HT devices, leading to the higher overall efficiencies of POPT devices.

Besides differences in absorption, another possible explanation for the higher photocurrent in the POPT device is improved blend morphology that allows for increased donor/acceptor (D/A) interfacial areas for exciton dissociation. Figure 4.4 shows the AFM height and phase images of films of POPT and P3HT blended with EV-BT at a 1:1 ratio. The samples were processed under identical conditions as the optimized BHJ devices. Notably, both samples lack any large scale phase separation, which indicates favorable mixing between the donor polymer and EV-BT. In addition, the blend films show similar domain sizes of 10-20 nm in the phase image. Since there appears to be little difference in total D/A interfacial areas in both samples, morphology mostly likely does not account for the large difference in photocurrent in devices made from the two polymers.

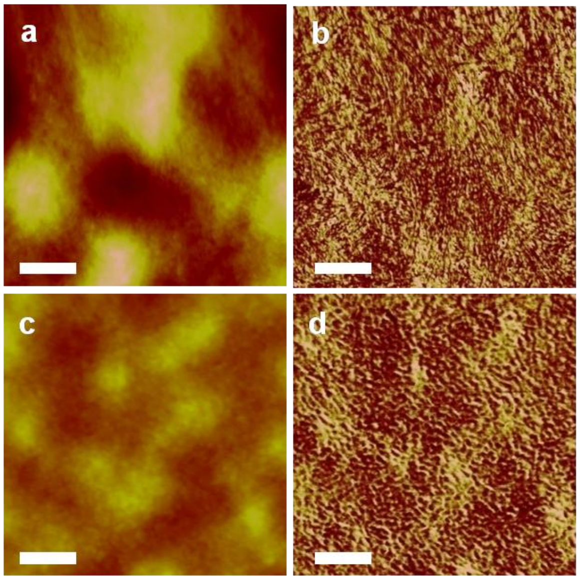

Figure 4.4. AFM height (left) and phase images (right) of POPT (a, b) and P3HT (c, d) blends with EV-BT at 1:1 ratios annealed at 80°C for 100 min. Scale bar is 200 nm.

As the higher photocurrent observed with POPT:EV-BT devices is not expected based on absorption and morphological considerations, we performed reverse bias analysis to study the electric-field dependence of the charge generation process in these devices. By applying a larger electric field across the device than the field at J_{sc}, there is an increased driving force for charge separation and collection within the device.[36,37] At sufficiently large reverse bias, the device reaches saturation where all the excitons that reach the D/A interfaces are separated into free charges, and all separated charges are collected at their respective electrode with minimal recombination losses, thus revealing the maximum potential of each polymer:EV-BT device.[36,37]

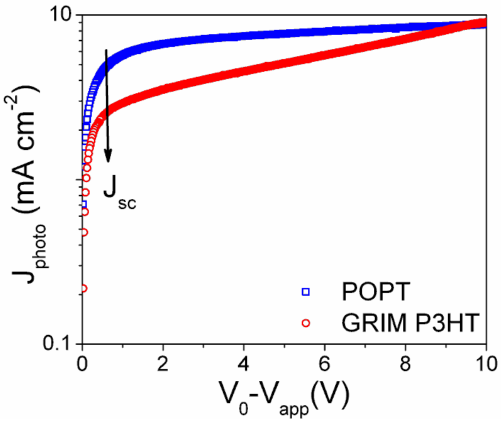

Figure 4.5. Photocurrent (J_{photo}) versus effective applied voltage (V_0-V_{app}) for optimized BHJ devices of POPT and P3HT with EV-BT.

In reverse bias analysis, the photocurrent is often plotted as a function of effective applied voltage. The photocurrent is defined as $J_{photo} = J_{light} - J_{dark}$, where J_{light} and J_{dark} are current densities of the device measured under illumination and in the dark. The effective applied voltage is defined as $V_{eff} = V_o - V_{app}$, where V_o is the compensation voltage defined as the voltage where $J_{photo} = 0$ and V_{app} is the applied bias. A reverse voltage sweep was applied to the polymer:EV-BT devices, and the photocurrent as a function of effective applied voltage is plotted in Figure 4.5. Both polymer:EV-BT pairs display higher J_{photo} at higher applied bias as is expected. For the POPT:EV-BT device, J_{photo} saturates relatively quickly at around $V_{eff} = 2$ V. On the other hand, in the P3HT device, J_{photo} continues to increase and does not reach saturation even at $V_{eff} = 10$ V. More importantly, the J_{photo} of the P3HT device surpasses that of POPT at $V_{eff} = 9.5$ V, indicating that P3HT:EV-BT can generate more photocurrent than POPT devices. The fact that a P3HT:EV-BT device can generate higher J_{photo} agrees with expectations based on absorption considerations (Table 4.1 and Figure 4.2) and the observation that the extent of D/A phase separation are similar in the two systems (Figure 4.4). However, at typical operating voltages near the J_{sc} position indicated in Figure 4.5, POPT outperforms P3HT in terms of charge separation as evidenced by the much higher J_{sc} in POPT:EV-BT devices. Comparing the J_{photo} at low and high fields for these two polymers, it is evident that the dissociation efficiency is much higher for the POPT device, and this device is achieving more of its potential under standard operating conditions.

4.2.3 Solar Cell Comparison of PQT-OP *vs.* PQT-DD

In order to generalize the effect of interfacial steric interactions on charge generation, we expanded the scope of this study beyond POPT and P3HT to another polymer backbone, polyquarterthiophene (PQT). We synthesized poly(3,3-di(4-n-octyl)phenylquaterthiophene) PQT-OP and compared it to poly(3,3-didodecylquaterthiophene) PQT-DD (Table 4.3 and Figure 4.6). Independently optimized devices with CNPPV, EV-BT, and PDI were consistently found to perform nearly twice as well with PQT-OP compared to the alkyl derivative PQT-DD, due largely to an increase in J_{sc}. The V_{oc} values for PQT based devices with the same acceptor material were greater than for the polythiophene based, however there were no significant V_{oc} differences between the phenyl and alkyl PQT derivatives. This supports our hypothesis that interfacial interactions could play a role that rivals the importance of the materials energy levels.[38-40] The CT state energy, whatever its physical structure, has already been strongly correlated with V_{oc}.[38] It is worth noting that PQT-OP:PDI devices reported here have the highest performance of any PDI-containing solar cells to date. These data supported our hypothesis that the effect of this substituent could be generalized to other systems, as this is the same trend that was observed for POPT compared to P3HT.

Table 4.3. Device parameters of PQT-OP vs. PQT-DD devices. Maximum efficiencies for individually optimized device systems. A ‘/’ indicates a bilayer device while a ‘:’ indicates a BHJ device.

Device Active Layer	J_{sc} (mA/cm^2)	V_{oc} (V)	*FF*	PCE (%)
PQT-OP/CNPPV	-2.43	1.18	0.39	1.12
PQT-DD/CNPPV	-1.51	1.20	0.38	0.69
PQT-OP/EV-BT	-2.68	0.95	0.48	1.22
PQT-DD/EV-BT	-1.48	0.98	0.43	0.62
PQT-OP:PDI	-3.33	0.63	0.42	0.88
PQT-DD:PDI	-2.18	0.66	0.34	0.49

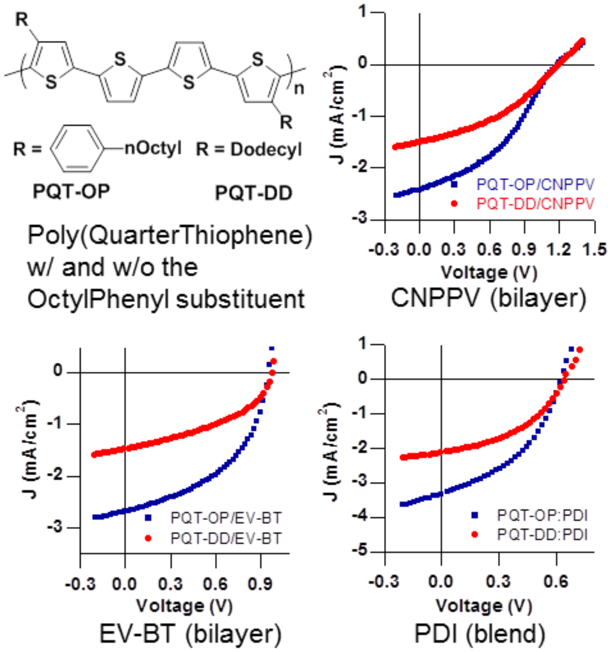

Figure 4.6. PQT polymer structures and a comparison of individually optimized devices. Devices were optimized on the basis of thickness, solvent choice and annealing conditions.

These experimental results are in contradiction with predictions based on a simple comparison of the donor polymer energy levels. The larger ionization potential (lower HOMO level) of POPT compared to P3HT (-5.5 vs. -5.2 eV) in combination with a smaller bandgap should thermodynamically result in a lower J_{sc} based on the abbreviated Weller equation. However, octylphenyl devices produce significantly increased J_{sc} values compared to devices utilizing the alkyl analogs. Morphological and light absorption parameters were ruled out as the dominant factor in this kind of comparison. Analysis of the PQT polymers provided similar results. PQT-OP has a slightly larger ionization potential (IP) and a similar optical gap compared to PQT-DD; PQT-OP and PQT-DD have IPs of -5.4 vs. -5.3 eV, respectively, and optical gaps of approximately 1.9-2.0 eV (with absorption onsets of 640 and 620 nm). Again, devices using the octylphenyl derivative PQT-OP consistently produce a substantially greater J_{sc}. These data clearly confirm that the material state energies and optical properties are not the only factors affecting the charge generation efficiencies in these systems. More importantly, we hypothesize that the molecular interactions at the D/A interface are a determining factor in these devices. Modeling of the D/A interface has recently predicted that the molecular configurations[23] and environment at this interface are critical in the charge-generation process, and here we aim to correlate theory with a benchmark physical test system.[24,41,42]

4.2.4 Calculations of a Model System: POPT/CNPPV *vs.* P3HT/CNPPV

Since the highest performing devices utilized POPT and P3HT in combination with CNPPV (Table 1, Figure 1) as the component materials, these systems were characterized in more detail to understand how their structural properties influence interfacial interactions and, ultimately, charge generation. The component materials were first analyzed using a computational description of their molecular geometries. Modeling at the Density Functional

Theory (DFT) B3LYP/6-31G(d,p) level of theory provided optimized geometries of the neutral ground states for (isolated) hexamers of the relevant species (Figure 4.7). Two POPT conformations were explored: the first structure allows the phenyl rings to participate in conjugation with the thiophene backbone (Figure 4.7b, POPT-*unconstrained*) and the second structure forces the phenyl rings to twist perpendicular to the backbone (Figure 4.7c, POPT-*perp*). POPT-*perp* minimizes conjugation between the pendant phenyl ring of the side group and the thiophene ring of the polymer backbone but maximizes conjugation along the backbone (Figure 4.8). The neutral ground-state geometries were also calculated for P3HT (Figure 4.7a) and CNPPV (Figure 4.7d), where the alkyl chains were modeled as methyl groups. The calculations show that the backbone of POPT is strictly planar only when the phenyl rings are forced out of plane with respect to the backbone, minimizing steric or electronic interactions between the thiophene and phenyl groups.

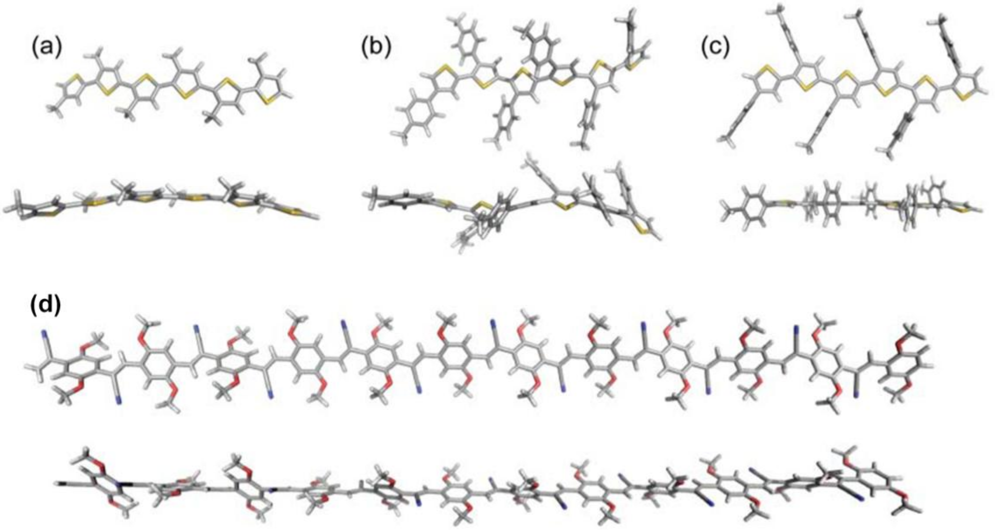

Figure 4.7.. B3LYP/6-31G(d,p) optimized neutral ground-state structures of the hexamers of (a) P3HT, (b) POPT-*unconstrained*, (c) POPT-*perp* and (d) CNPPV shown from the top-view (top) and side-view (bottom).

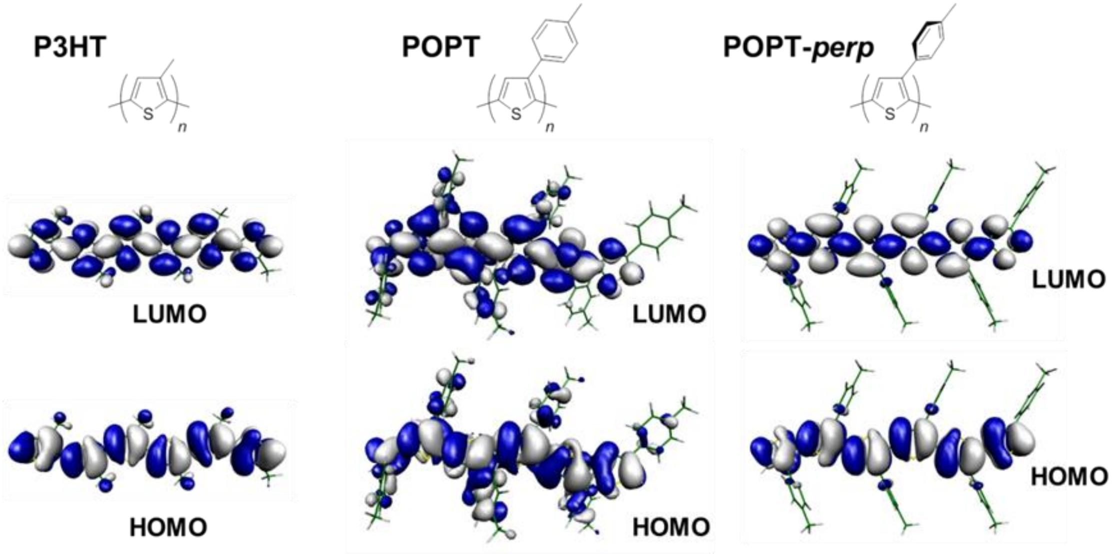

Figure 4.8. P3HT and POPT molecular orbitals.

Vertical transition energies of the polymers can be qualitatively described from those of the oligomers by a Kuhn-type dependence on 1/*N* where *N* is the number of double bonds along the shortest path connecting the terminal carbon atoms of the molecular backbone.[43] The electronic structures for oligomers of increasing length were calculated and a Kuhn fit of the data was used to extrapolate the $S_0 \rightarrow S_1$ transition energies of the extended polymers. The plots for the two POPT structures, P3HT, and CNPPV are presented in Figure 4.9. The best agreement between theory and experiment, i.e., where the optical bandgap (E_g^{opt}) for POPT equals 1.8 eV, occurs when the polymer backbone is planar, suggesting that the phenyl groups of polymer side chains prefer to orient perpendicular to the backbone in thin films. The results for P3HT and CNPPV are also in good agreement with experiment.

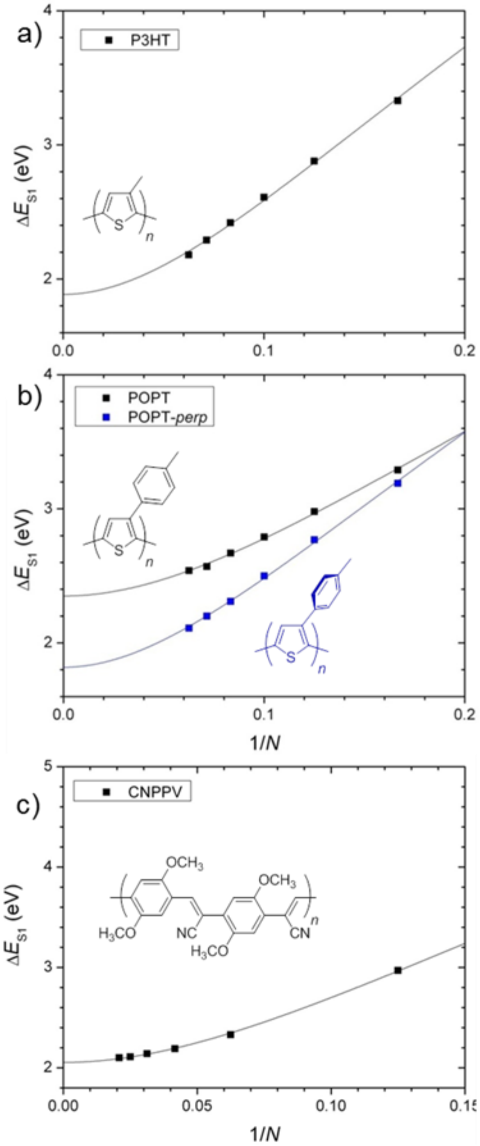

Figure 4.9. Vertical S0 → S1 transition energies of (a) P3HT and (b) POPT-*unconstrained* and POPT-*perp* where the phenyl group is constrained to be perpendicular to the polymer backbone (c) CNPPV. *N* is the number of double bonds along the backbone.

The presence of two dominant conformations of POPT is supported empirically by two-dimensional grazing incidence X-ray scattering (2D GIXS) measurements. Figure 4.10a shows the 2D GIXS pattern and the in-plane line scan of the POPT sample, while Figure 4.10b illustrates the schematic of solid-state packing for POPT. The presence of two peaks at 3.8 and 5.1 Å suggests that there are two different π-π packing distances in the POPT thin film. Importantly, these two different π-π packing distances arise from the two major conformations for the phenyl rings relative to the POPT backbone: the π-π packing distance of 3.8 Å correlates to the phenyl ring oriented parallel with the backbone, while the π-π stacking distance of 5.1 Å correlates to a POPT-*perp* orientation where the phenyl ring is twisted perpendicular to the backbone and causes an increase in separation between adjacent polymers. It should also be noted that the peak broadening observed in the GIXS pattern may be an indication that the phenyl ring can adopt varying degrees of rotation between the parallel and perpendicular conformations. The packing parameters of POPT have been studied in-depth elsewhere.[44]

GIXS data of PQT-OP also evidences two dominant conformations for the phenyl ring, resulting in π-π spacings of 5.1 and 3.9 Å (Figure 4.11). The relative scattering intensity of the two π-π spacings in PQT-OP is reversed from that of POPT. This reversal in PQT-OP can be attributed to the lack of substituents on two of the four thiophenes in the polymer repeat unit, thereby favoring the tighter π-π spacing at 3.9 Å. Detailed GIXS data for P3HT[45] and PQT-DD[46] have been analyzed previously, and backbone spacings of 3.8 and 4.2 Å were reported, respectively. CNPPV derivatives are known to be relatively amorphous; however, weak diffraction signals between 4 and 5 Å have been observed.[47,48] X-ray scattering, however, is limited to the investigation of regular periodicity in a material and is not appropriate for the study of blended interfaces. Since we are interested in the D/A interface in these material systems, we turned to computational analysis to develop a model interface for the charge separation event.

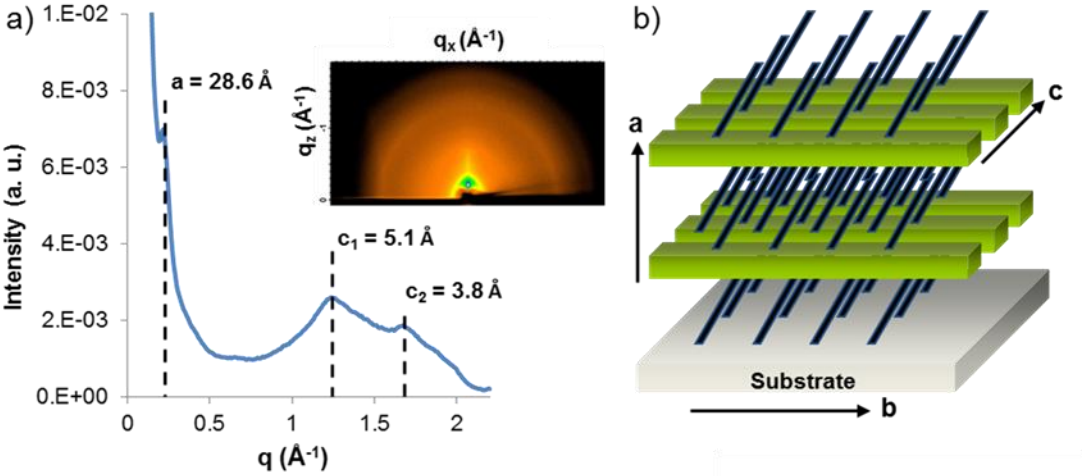

Figure 4.10. (a) An X-ray line scan of POPT thin film taken parallel to the substrate surface showing peaks at *d* spacing equal to 28.6, 5.1 and 3.8 Å corresponding to the "a" distance and two different "c" distances, respectively. (inset) 2D GIXS pattern of POPT thin film on Si substrate. (b) Schematic of the polymer solid state packing relative to the substrate, with corresponding labels to the peaks indicated in (a).

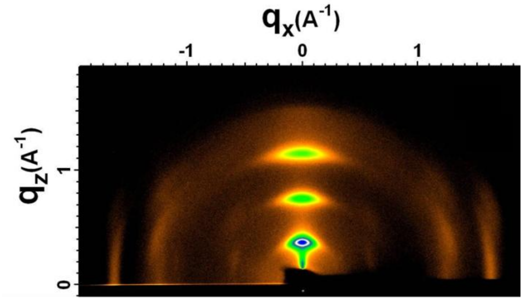

Overnight annealing at 150°C

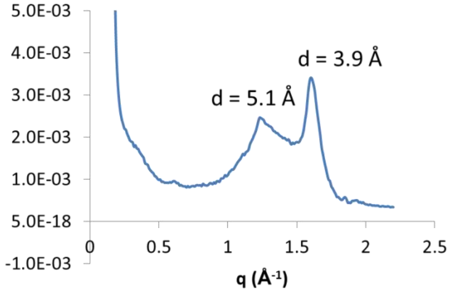

Figure 4.11. 2D GIXS data and 1D line-scan for a film of PQT-OP on Si substrates.

Model dimer configurations were constructed from best-fit-planes of polythiophene/CNPPV separated at distances (R) between 4 and 5 Å at 0.2 Å increments (Figure 4.12). In order to construct CT states from these dimers, charges were constrained to each molecule using the constrained density functional theory (C-DFT) method implemented in NWChem Version 4.6.[49-52] A conductor polarizable continuum model (CPCM) with ε = 4 was used to approximate polarization effects expected in organic solid-state systems. Given the limitations of the theoretical approach, we are mainly interested in the relative CT-state energies, which are plotted in Figure 5c. The model dimer configuration of POPT-*perp* is predicted to have the highest CT state energy followed by the P3HT and then the POPT-*unconstrained* configurations.

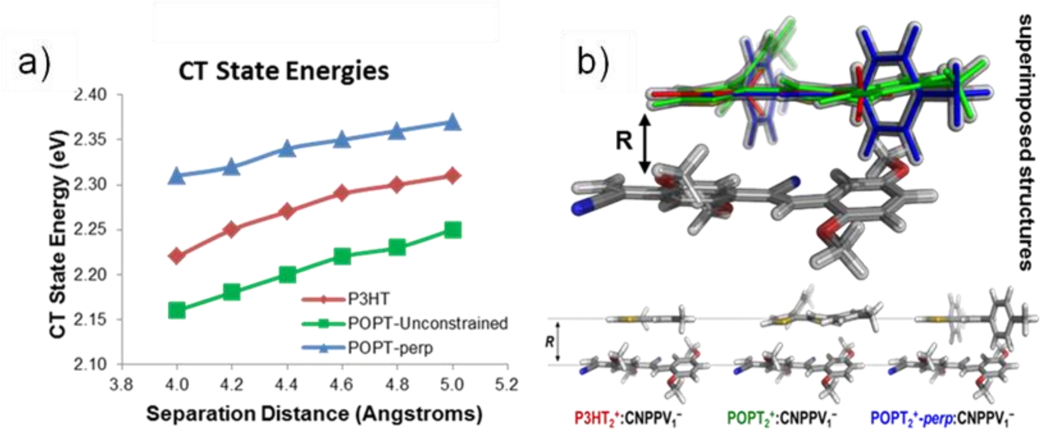

Figure 4.12. (a) CT-state energies for the D/A systems illustrated in (b), estimated at the C-DFT B3LYP/6-31G(d,p) level. (b) Physical representation of dimers of POPT and P3HT with a single repeat unit of CNPPV, both superimposed and side-by-side.

4.2.5 Probing the Charge-Transfer (CT) State

To verify our calculations of the CT state energies in these D/A systems, we used spectroscopic techniques to experimentally observe their CT states. Sensitive photocurrent measurement, via Fourier transform photocurrent spectroscopy (FTPS),[38,53] can extract the weak sub-bandgap external quantum efficiency, and photothermal deflection spectroscopy (PDS) can detect sub-bandgap absorption. These tools have previously been used to investigate charge-transfer states.[54,55] A recent FTPS study suggests that the CT state is efficiently split into free charge carriers at room temperature in P3HT:PCBM and MDMO-PPV:PCBM devices.[56] Spectral evidence and device studies of various D/A systems suggest that these CT states determine the V_{oc} of the PV cell and act as an intermediate in the generation *and* recombination of free charge carriers.[38,53] Consequently, spectroscopic techniques rooted in sub-bandgap absorption are considered a good indicator of the presence of such CT states and of the maximum V_{oc} that can be expected with a given D/A combination.

PDS spectra were obtained by detecting the mirage effect in a transparent, inert medium (Fluorinert®) with a probe HeNe laser beam. Non-radiative heating associated with absorption of a monochromatic pump beam causes the mirage effect to occur. PDS was used in this investigation to support our hypothesis that molecular orientation of the phenyl groups affects the CT state energy. PDS measurements were performed on drop cast and spun cast films of POPT and P3HT blended with CNPPV. Bilayer films do not provide enough interfacial surface area to produce good signal-to-noise ratios; in addition, the *molecular level interface* is not expected to change upon going from the bilayer to BHJ morphology, *vide infra*. Figure 4.13 shows the PDS spectra of the homopolymers and the polymer blends under investigation; spectra are scaled to absolute values of absorption coefficient by matching the signal near the absorption edge to that from UV-vis spectra of the same films.

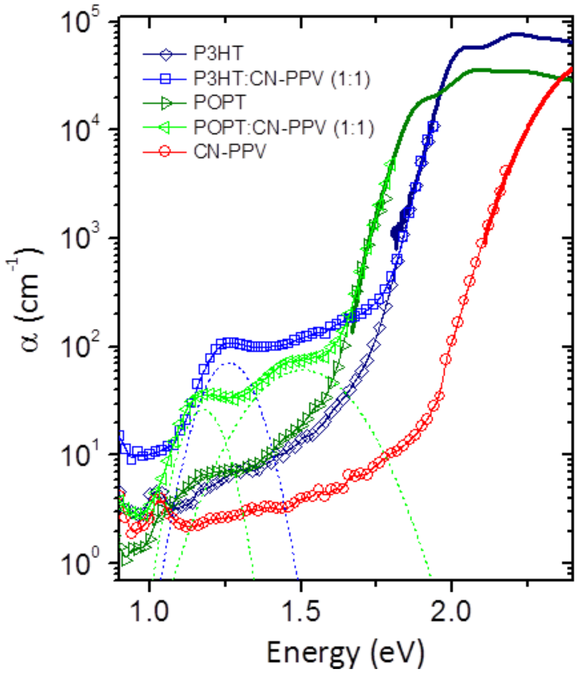

Figure 4.13. PDS spectra of P3HT, POPT and blends with CN-PPV. Thick solid lines are UV-vis absorption spectra of the homo-polymers, symbols are the PDS absorption spectra of drop cast films. P3HT:CNPPV peak maximum at 1.26 eV, while POPT:CNPPV possesses two peaks at 1.17 and 1.50 eV.

Blends of both P3HT and POPT with CNPPV produce non-additive absorptions that are attributed to the presence of CT states at the D/A interfaces. For P3HT:CNPPV (1:1 wt/wt), a CT state absorption is present at 1.26 eV. For POPT, however, there are two sub-bandgap peaks attributed to CT states, one at 1.17 eV and one at 1.50 eV – indicating two distinct interfacial configurations. These peak maxima are extracted by fitting an exponential for the band edge and Gaussian curves for the CT peaks in the sub-bandgap regions. The results of the calculations presented in Figure 4.12a are qualitatively consistent with the observed PDS absorption peaks: the P3HT:CNPPV blend has a CT state energy that resides between the two POPT:CNPPV CT state energies. (We note that, in addition to the intrinsic limitations of the methodologies, the difference in energy between theory and experiment may due in part to the fact that the extent of delocalization of the CT state could be larger than what was considered in the calculations). To verify that the energies of these CT states remain unchanged with film morphology and film thickness, drop cast and spun cast POPT:CNPPV (1:1) films were compared and there was minimal difference.

PDS measurements were also performed to probe the CT state energies of the PQT-based polymers blended with CNPPV. The PQT-DD:CNPPV (1:1 wt/wt) shows little non-additive sub-bandgap absorption, while PQT-OP presents two sub-bandgap absorption peaks at 1.25 eV and 1.56 eV. The higher energy CT state peak is significantly less intense for PQT-OP compared with POPT (Figure 4.14); the reason for this is discussed below.

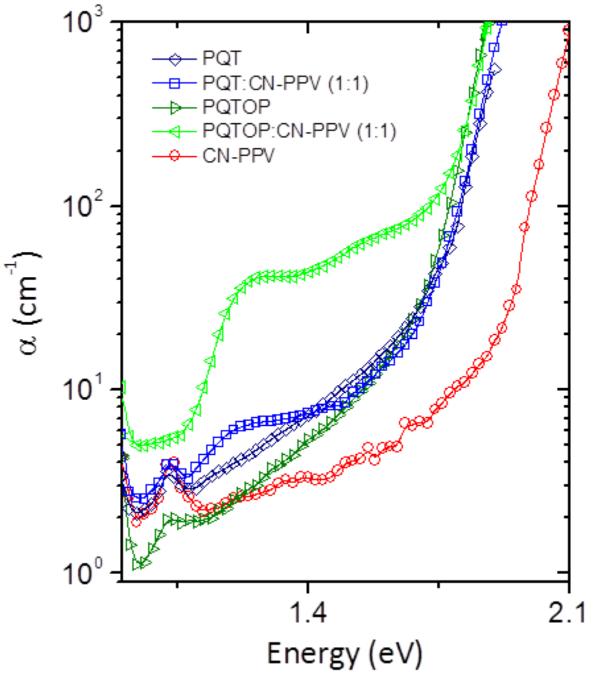

Figure 4.14 PDS spectra of PQT, and POPOP and blends with CN-PPV.

4.3 Discussion

A thermodynamic driving force for charge generation, i.e., exciton dissociation leading to charge separation, is present at the interface between the donor/acceptor (D/A) materials in an

OPV active layer. Photon absorption by either the donor or acceptor material produces the opportunity for charge-carrier generation. In the case of donor excitation, the system decreases in potential energy from the singlet excited state (E_s) by transferring an electron from donor to acceptor; in the case of acceptor excitation, by transferring a hole from acceptor to donor. For simplicity, the process is generally discussed from the viewpoint of an excited donor material. A general diagram depicting charge separation is presented in Figure 4.15.

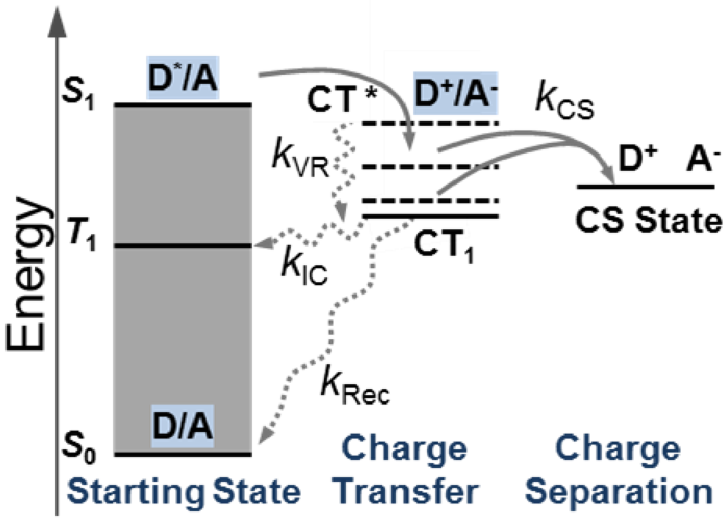

Figure 4.15. A diagram of possible electron flow pathways at the D/A interface, relative to potential energy (adapted from Ref. 18). CT state energies (ground state solid black, excited state dashed black) are shown in relation to the D/A singlet excited state (S_1), triplet state (T_1) and ground state (S_0). Competing energetic pathways and rates are also depicted: vibrational relaxation of the CT state (k_{VR}), intersystem crossing of the CT state to the donor triplet state (k_{IC}), recombination of the CT state to the ground state (k_{Rec}), and finally charge separation (k_{CS}). Both the thermodynamics and the kinetics of these processes affect the charge separation behavior.

Although a thermodynamic driving force helps to generate free charge, the immediate physical separation of the electron and hole does not necessarily lead *directly* to free charges. The low dielectric constant of the active layer can produce a Coulomb trap for a partially separated exciton at the D/A interface. This state is usually referred to as a charge-transfer (CT) state. The CT state may either recombine to the initial ground states of the donor and acceptor materials, or it may undergo further separation into free charges. It is broadly debated whether an intermediate CT state is requisite to charge separation[18,56] and it is more recently debated whether this separation/generation can occur from lowest-lying CT_1 states.[56] The current understanding is that partial exciton dissociation can create either an excited CT state (CT*), which is most likely to escape the Coulomb trap, or a ground state CT state (CT_1).[57]

In addition to thermodynamics, we cannot ignore the important kinetic considerations of this process. Since excited CT* states that may relax down to CT_1, two rates are of critical importance: the rate of charge separation (k_{CS}) and the rate of vibrational relaxation of an excited CT state down to CT_1 (k_{VR}) (Figure 4.15). If $k_{CS} > k_{VR}$, then the electron is expected to readily escape the Coulomb potential and proceed to the charge separated (CS) state. If $k_{VR} > k_{CS}$, then relaxation to the CT_1 state leads to a more tightly bound (lower energy) intermediate. The electron can still escape from the relaxed CT_1 state,[56] however, other processes start to compete with charge separation. For instance, if either the donor or acceptor material possesses a triplet level (T_1) below the CT_1 state, intersystem crossing leads to long-lived metastable triplets. Also, the CT_1 state for some systems can radiatively or vibrationally decay to the ground state S_0 (k_{Rec}).[58,59] For these reasons, the kinetics of charge separation must be considered when parsing the charge-generation process.

In this work, OPV devices comparing POPT to P3HT and PQT-OP to PQT-DD were fabricated and analyzed. POPT and PQT-OP possess phenyl groups covalently bound to the polymer backbone as part of the solubilizing substituents. This functionality decreases the thermodynamic driving force for charge separation, but both POPT and PQT-OP surprisingly produced remarkably higher J_{sc} relative to their alkyl analogs P3HT and PQT-DD. All relevant PV characteristics are summarized in Tables 4.2 and 4.3. Further, X-ray scattering data evidenced that the pendant phenyl rings on POPT and PQT-OP can adopt planar-with- and perpendicular-to-the-backbone conformations. CT state energies for model dimer configurations were calculated and are plotted in Figure 4.12a. POPT-*perp* is predicted to have the highest CT state energy, while the CT state energy for P3HT lies between those of the POPT-*perp* and POPT-*unconstrained* conformations. Finally, spectroscopic evidence of charge-transfer states at the interface with the acceptor CNPPV, gathered via PDS for all four donor polymers, is consistent with the relative values predicted by the model dimer calculations.

Due to the out-of-plane twist of the phenyl rings, the separation distance between POPT and the acceptor molecule at the D/A interface likely increases as steric repulsion from the phenyl ring hinders backbone-backbone interaction. PDS data confirms the presence of two distinct features in the sub-bandgap regime, which is likely a direct result of these two dominant phenyl ring conformations at the D/A interface. Since these conformationally dependent states are both involved as intermediates in the charge-generation process, the corresponding electron-hole pairs must overcome different energetic barriers to split into free charges. We postulate that the twisted phenyl ring conformation of POPT (POPT-*perp*) is beneficial for charge generation, as an intermediate with increased potential energy is more likely to fully separate into free charges (Figure 4.16).

This study also generated two additional significant and supportive findings. PDI-based acceptors have garnered much attention as alternative n-type materials to replace fullerenes;[5] here, we produce the highest efficiency devices with this acceptor to date, despite tremendous efforts with alternative approaches towards higher efficiency.[5,21,29] This is another indication that control over the interfacial geometry at the molecular level can lead to much improved device performance, as a complementary tool to morphology and energy level control. Additionally, the device performance with the high mobility n-type polymer N2200 demonstrates that POPT outperforms P3HT both in our labs and compared to two very recent reports.[34,35]

Combining all the data, analysis, and literature context, we propose a general design principle for improving charge separation in non-fullerene OPVs: tuning the D/A interfacial interaction through steric control can facilitate photocurrent generation. Regardless of whether charge separation happens from a relaxed CT_1 state or an excited CT state, increasing the steric bulk at the D/A interface decreases the Coulomb binding strength exerted on the geminate pair. We postulate that the phenyl ring pendant to POPT and PQT-OP provides an almost ideal interaction distance between the charge carrying components of the D/A interface, and this leads to two of the best non-fullerene OPV devices reported to date. The higher energy of the intermediate CT state, with a lower activation barrier to free carrier generation, improves photocurrent generation and provides the key to the observed phenomenon (Figure 4.16). This effect was not limited to one donor polymer or one acceptor material, but rather it was general for two donors and four acceptors – four polymers and two small molecules. All of these material combinations yielded devices with the phenyl containing polymer producing substantially greater J_{sc}, and overall power conversion efficiency, than their alkyl analogs.

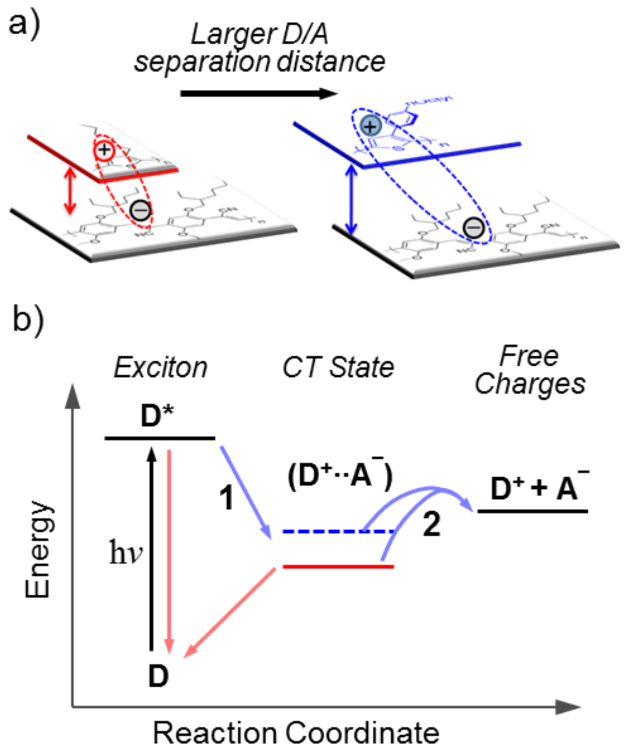

Figure 4.16. (a) Schematic of how steric interactions can lead to an increase in backbone spacing, a decrease in the Coulomb binding force and destabilization of the CT state. (b) The phenomenon depicted in (a) leads to a different energy landscape with increased charge separation probability in POPT, as the CT state is considered an intermediate trapped in an energetic well.

4.4 Conclusion

We have utilized computational modeling, PDS spectroscopy, and tailored synthetic design in order to probe the importance of steric interactions at the donor/acceptor interface in non-fullerene OPV devices. By introducing the octylphenyl substituent onto the investigated polymer backbones, the charge-transfer state of the D/A system can be raised in energy. This decreases the energetic barrier to charge separation and results in increased photocurrent generation. The design principle was shown to be general across two polythiophene backbones and with four different acceptors – two polymeric and two small molecules. The lower energy PDS onset for POPT based devices with CNPPV (1.17 eV) vs the onset for PQT-OP with CNPPV (1.26 eV) is reflected in the V_{oc} of these devices. The combined data from POPT and PQT-OP devices and their materials analyses suggest that controlling the steric interaction at the D/A interface could be a general design principle toward improving charge generation in non-fullerene OPVs.

4.5 Experimental

4.5.1 Synthetic Details

All reagents from commercial sources were used without further purification, unless otherwise noted. All reactions were performed under dry N_2, unless otherwise noted. All dry reactions were performed with glassware that was oven dried and then flamed under high-vacuum and backfilled with N_2. All extracts were dried over powdered magnesium sulfate ($MgSO_4$) and solvents removed by rotary evaporation under reduced pressure. Toluene and tetrahydrofuran (THF) were purified and dried by passing through two columns of neutral alumina under nitrogen prior to use. All solvents used in Pd-catalyzed cross-coupling reactions were degassed prior to use. Flash chromatography was performed using Silicycle SiliaFlash ® P60 (particle size 40-63 µm, 230-400 mesh) silica gel. CN-PPV was purchased from H. W. Sands Corp. and used without further purification. The molecular weight was M_n = 16 kDa with a PDI of 4.5.

All compounds were characterized by ^{1}H NMR (400 MHz) and ^{13}C NMR (100 MHz) on a Bruker AVB 400 or AVQ 400. High-resolution mass spectra and elemental analysis (CHNS) was performed at the University of California, Berkeley Department of chemistry analytical services. Polymer ^{1}H NMRs (500 MHz) were obtained on Bruker DRX 500. ^{13}C spectra were measured with a proton-decoupling pulse program. For polymer molecular weight determination, P3HT and POPT samples were dissolved in HPLC grade dichlorobenzene at a concentration of 1 mg/ml, briefly heated and then allowed to return to room temperature prior to filtering through a 0.2 µm PVDF filter. SEC was performed using HPLC grade dichlorobenzene at a flow rate of 0.8 µL/min on two 300 x 8 mm linear S SDV, 5 µm columns at 70 ºC using a Waters 2690 separation module and a Waters 486 Tunable Absorption Detector monitored at 350 nm. The instrument was calibrated vs. polystyrene standards (1,050 – 135,000 g/mol) and data was analyzed using Millenium 3.2 software. For PQT-DD and PQT-OP, solutions (1 mg/mL) were prepared using HPLC grade tethrahydrofuran (THF). Samples were briefly heated and then allowed to return to room temperature prior to filtering through a 0.45 µm PVDF filter. SEC was performed with HPLC grade THF eluent at 1.0 mL/min by using three PLgel columns (7.5 x 300 mm) with pore sizes of 10^5, 10^3, and 500 Å, respectively. The particle size in columns was 5 µm and the columns were thermostated at 35 °C. The SEC system consisted of a Waters 510 pump, a Waters 717 autosampler, a Waters 486 UV-Vis detector, and a Wyatt Optilab DSP differential refractive index detector.

Scheme 4.1.

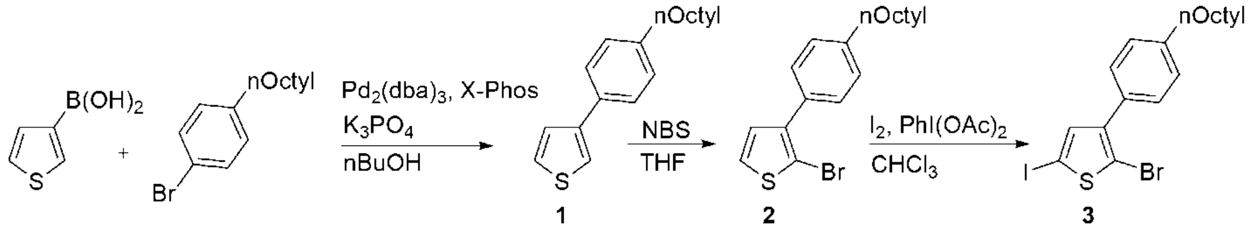

3-(4-nOctyl)-phenylthiophene (1) In a 250 mL 3-neck round bottom with reflux condenser, 4-octyl-bromobenzene (TCI America, 15.00 g, 55.72 mmol), 3-thiophene boronic acid (Combi-Blocks, 7.85 g, 61.28 mmol, 1.1 eq), and tribasic potassium phosphate (15.40 g, 2eq of boronic acid) were dissolved in nButanol (110 mL). This mixture was degassed with N_2 for 30 minutes at which point $Pd_2(dba)_3$ (262 mg, 0.0025 eq) and 2-Dicyclohexylphosphino-2',4',6'-triisopropylbiphenyl (X-Phos) (79 mg, 0.01 eq) was added in one portion and the reaction heated to 100 °C for 12 hours. The reaction was then rotovapped to remove nBuOH and flashed through a silica plug with hexanes and minimal chloroform (to help load the product) to remove powdered phosphates and other impurities (a clay/dirt crude product). The crude (clear & colorless) flashed product was then recrystallized from ethanol. 12.88 g, 85 % yield, white solid flakes. ^{1}H NMR (400 MHz, *$CDCl_3$*): δ ppm 7.53-7.50 (m, 2H), 7.42-7.36 (m, 3H), 7.22 (d, *J* = 8.10 Hz, 2H), 2.65-2.59 (t, 2H), 1.63 (td, *J* = 15.10, 7.54, 7.54 Hz, 2H), 1.38-1.23 (m, 10H), 0.91-0.86 (t, 3H). ^{13}C (100 MHz, *Acetone-d_6*): δ 142.11, 141.66, 133.19, 128.79, 126.26, 126.06, 126.03, 119.62, 35.25, 31.72, 31.41, 22.43, 13.49.

2-bromo-3-(4-octyl)-phenylthiophene (2) In a 25 mL 1 neck round bottom, 3-(4-octyl)-phenylthiophene (1.26 g, 4.6 mmol) was dissolved in $CHCl_3$ (10 ml) and cooled to 0 °C. N-Bromosuccinimide (NBS) (825 mg, 4.6 mmol) was added in one portion to the stirring solution. The reaction was heated to 40 °C for 1 hour and then stirred at room temperature for an additional hour. Usual color change was from clear to yellow back to almost clear. The resultant pale yellow solution was diluted with Et_2O and 1M NaOH added to quench any residual NBS and Br_2. The organic layer was then separated and the aqueous layer extracted with Et_2O. The crude product was then purified by silica gel chromatography (hexanes). This reaction is neither anhydrous nor done under nitrogen. 11.5 g, 93 % yield, colorless oil. ^{1}H NMR (400 MHz, *Acetone-d_6*): δ ppm 7.58 (d, *J* = 5.67 Hz, 1H), 7.51 (d, *J* = 8.13 Hz, 2H), 7.30 (d, *J* = 8.00 Hz, 2H), 7.14 (d, *J* = 5.67 Hz, 1H), 2.70-2.63 (t, 2H), 1.73-1.59 (m, 2H), 1.46-1.22 (m, 10H), 0.93-0.84 (t, 3H). ^{13}C (100 MHz): δ 143.44, 142.88, 138.92, 130.85, 128.47, 128.29, 110.18, 72.93, 35.40, 31.76, 31.34, 22.47, 13.57. HRMS calc *m/*z for ($C_{18}H_{23}BrS$) 350.0704; found 350.0701. Anal. Calcd for $C_{18}H_{24}S$: C, 61.53; H, 6.60; S, 9.13. Found: C, 61.76; H, 6.61; S, 9.29.

2-bromo-5-iodo-3-(4-octyl)-phenylthiophene (3) In a 1 neck flask, 2-bromo-3-(4-octyl)-phenylthiophene (5.3 g, 15.04 mmol) was dissolved in $CHCl_3$ (1 M) and cooled to 0 °C. I_2 (2.10 g, 8.27 mmol, .55 eq) and $PhI(OAc)_2$ (2.90 g, 9.02 mmol, .60eq) were added while stirring. The reaction was slowly warmed to room temperature over 12 hours. The reaction was then diluted with Et_2O and saturated aqueous sodium thiosulfate was added to ensure the elimination of any residual molecular iodine. The organic layer was separated and the crude product purified by silica gel chromatography (hexanes). This reaction is neither dry nor done under nitrogen. 5.77 g, 80 % yield, colorless oil. ^{1}H NMR (400 MHz, *Acetone-d_6*): δ ppm 7.49 (d, *J* = 8.12 Hz, 2H), 7.38 (s, 1H), 7.31 (d, *J* = 8.09 Hz, 2H), 2.77-2.56 (t, 2H), 1.73-1.58 (m, 2H), 1.43-1.24 (m, 10H), 0.96-0.84 (t, 3H). ^{13}C (100 MHz): δ 143.44, 142.87, 138.92, 130.85, 128.47, 128.29, 110.19, 72.93, 35.42, 31.77, 31.36, 22.49, 13.59. HRMS calc *m/*z for ($C_{18}H_{22}BrIS$) 475.9670; found 475.9675. Anal. Calcd for $C_{18}H_{22}BrIS$: C, 45.30; H, 4.65; S, 6.72. Found: C, 45.59; H, 4.54; S, 6.86.

Poly(3-(4-octyl)-phenylthiophene) (POPT) A three-necked round bottom flask with reflux condenser and stirbar was charged with monomer **3** (1.0 g, 2.1 *m*mol) and 50 mL dry THF. The resulting solution was cooled to -78 ^{o}C and stirred for 20 minutes. Then ^{i}PrMgCl (2M in THF, 1.0 ml, 0.96 eq.) was added to the reaction mixture dropwise. After stirring at -78 ^{o}C for 10 minutes, the reaction was removed from the -78 ^{o}C bath and allowed to warm to RT over a 1 hour period. During the last 15 minutes of metal-halogen exchange, an oil bath was pre-heated to 65 ^{o}C. Then Ni(dppp)Cl_2 (4 mg, 0.35 mol%) was added in one portion and the reaction placed in the preheated oil bath and stirred for 12 hours. Following the addition, the color of the reaction mixture changed from colorless to red. The polymer was precipitated into methanol (250 mL) from the THF reaction solution and filtered through a Soxhlet thimble. The polymer was purified by Soxhlet extraction with methanol for 6 h, hexanes for 6 h, and chloroform for 6 h. The polymer was then isolated by extraction with chlorobenzene, followed by concentration under a stream of nitrogen and finally precipitation into methanol (500 mL). A typical yield of ~ 50% was obtained for these polymerizations. NMR (500 MHz, $CDCl_3$): δ ppm 7.19 (dd, *J* = 37.39, 8.03 Hz, 4H), 6.79 (s, 1H), 2.63-2.56 (t, 2H), 1.63-1.60 (m, 2H), 1.31-1.25 (m, 10H), 0.88-0.85 (t, 3H).

Scheme 4.2.

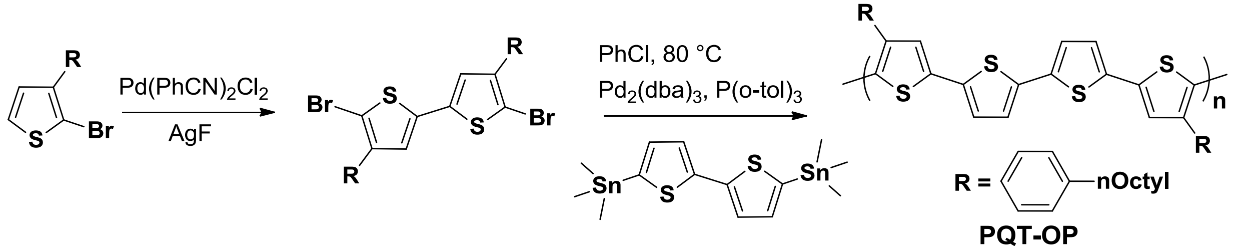

2-bromo-5-(5-bromo-4-(4-n-octylphenyl)thiophen-2-yl)-3-(4-n-octylphenyl)thiophene: In a 100 mL round bottom, 2-bromo-3-(4-octyl)-phenylthiophene (1.45 g, 4.16 mmol), Pd$(PhCN)_2Cl_2$ (16 mg, 1 mol. %), $AgNO_3$ (1.42 g, 8.32 mmol), and potassium fluoride (0.48 g, 8.32 mmol) and 20 mL of anhydrous DMSO were combined. This reaction was heated to 60 °C for 3 hours, and then another two equivalents of $AgNO_3$ and KF were added. The reaction continued overnight. In the morning, the reaction was filtered through celite with diethyl ether, and the filtrate was washed with 1M HCl and excessive amounts of water. The diethyl ether was removed by roto-evaporation and the crude product purified by column chromatography (100% hexanes). 800 mg of a pure white solid were obtained (28% yield). ^{1}H NMR (400 MHz, $CDCl_3$): δ = 7.68 (d, *J* = 8.10 Hz, 4H), 7.47 (s, 2H) 7.46 (d, *J* = 8.03 Hz, 4H), 2.90-2.81 (m, 4H), 1.93-1.79 (m, 4H), 1.64-1.40 (m, 20H), 1.10 (t, *J* = 6.75, 6.75 Hz, 3H). ^{13}C (100 MHz, $CDCl_3$): δ = 142.89, 142.09, 136.13, 131.82, 128.48, 128.36, 125.52, 107.37, 35.77, 31.89, 31.37, 29.48, 29.39, 29.26, 22.67, 14.11

poly(3,3-di(4-n-octyl)phenylquaterthiophene) (PQT-OP): In a 50 mL 3-neck round bottom flask, (**1**) and 2-(trimethylstannyl)-5-(5-(trimethylstannyl)thiophen-2-yl)thiophene were combined and dissolved in 15 mL of PhCl. This solution was degassed by bubbling with nitrogen for 10 minutes, and then Pd_2(dba)3 (11.53 mg, 3 mol. %) and P(o-tol)$_3$ (15.33 mg, 12 mol. %) were added in one shot (together). The mixture was stirred for 36 hours, at which point a strongly complexing ligand (N,N-Diethylphenylazothioformamide, CAS# 39484-81-6) was then stirred with the polymer to remove any residual catalyst before being precipitated into methanol (200 mL). The precipitate was filtered through a Soxhlet thimble and purified via Soxhlet extraction for 12 h with methanol, 1 h with hexanes, chloroform until the eluent went clear, and finally extracted with PhCl. The PhCl solution was then passed through a plug of silica, neutral alumina, and celite (1:1:1), with excess $CHCl_3$ and then concentrated by evaporation and precipitated into methanol (200 mL). A significant quantity of polymer was lost in the chromatography step because of poor solubility. Pure PQT-OP was filtered off as a dark solid (90 mg). SEC analysis: $M_n = 29.3$ kDa, PDI = 1.54

The synthesis of poly(3,3-didodecylquaterthiophene) PQT-DD has been reported previously – *Macromolecules*, **2007**, *40* (21), pp 7425–7428

4.5.2 Optical, Electronic, and Thin Film Characterization

Cyclic voltammograms were collected using a Solartron 1285 potentiostat under the control of CorrWare II software. A standard three electrode cell based on a Pt button working electrode, a silver wire pseudo reference electrode (calibrated vs. Fc/Fc^+), and a Pt wire counter electrode was purged with nitrogen and maintained under a nitrogen atmosphere during all measurements. Acetonitrile was distilled over CaH_2 prior to use and tetrabutyl ammonium hexafluorophosphate (0.1 M) was used as the supporting electrolyte. Polymer films were drop cast onto a Pt button working electrode from a 1% (w/w) chloroform solution and dried under nitrogen prior to measurement.

UV-Visible absorption spectra were obtained using a Cary 50 Conc UV-Visible spectrophotometer. For thin film measurements polymers were spin coated onto cleaned glass slides from chlorobenzene solution (10 mg/ml). A model P6700 Spincoater was used to spin coat the films at 1200 RPM for 60 s. Polymer film thickness was measured by a Veeco Dektak profilometer.

Atomic force microscopy (AFM) was performed using a Veeco (Digital Instruments) Multimode microscope with a Nanoscope V controller. Imaging was performed in semi-contact (tapping) mode using Veeco RTESP tips.

Thin-film transistors were fabricated on 300 nm SiO_2 dielectric substrates on heavily doped silicon. Bottom contact source-drain electrodes (Cr = 5 nm, Au = 100 nm) were fabricated by conventional photolithography using a transparency photomask. Channel lengths of 10 and 20 μm and channel widths of 100 and 200 μm were used for discrete transistors. The active semiconducting layer was applied by spin-casting 5-10 mg/mL solutions in anhydrous chlorobenzene at 2000 rpm. The films were then vacuum-dried overnight and measurements were carried out in ambient conditions using an Agilent 4156C Precision Semiconductor Parameter Analyzer.

Polymer mobility was measured using a diode configuration of ITO/ PEDOT:PSS/ Polymer/Al in the space charge limited current (SCLC) regime. At sufficient potential the conduction of charges in the device can be described by

$$J_{SCLC} = \frac{9}{8}\varepsilon\varepsilon_o\mu\frac{V^2}{L^3}, \qquad (1)$$

where ε_0 is the permittivity of free space, ε is the dielectric constant of the polymer, μ is the mobility of the majority charge carriers, V is the potential across the device ($V = V_{applied} - V_{bi} - V_r$), and L is the polymer layer thickness. The series and contact resistance of the device (~15 Ω) was measured using a blank device (ITO/PEDOT/Al) and the voltage drop due to this resistance (V_r) was subtracted from the applied voltage. The built-in voltage (V_{bi}), which is based on the relative work function difference of the two electrodes, was also subtracted from the applied voltage. The built-in voltage can be determined from the transition between the Ohmic region and the SCLC region and was found to be about 1 V.

Grazing-incidence x-ray scattering (GIXS) experiments were conducted at the Stanford Synchotron Radiation Laboratory on beamline 11-3 and 7-2. Samples were irradiated at a fixed incident angle on the order of 0.1^o and their GIXS patterns were recorded with a 2-D image detector (MAR345 image plate detector). GIXS patterns were recorded with an X-ray energy of 12.7 keV (λ = 0.975 Å). To maximize the intensity from the sample, the incident angle (~0.1^0 – 0.12^o) was carefully chosen such that the X-ray beam penetrated the sample completely but did not interact with the silicon substrate. Typical exposure times were 30-600 s.

4.5.3 Photovoltaic Device Fabrication

All devices were fabricated on ITO-coated glass substrates (pre-patterned, R = 20 Ω^{-1}). The substrates were sonicated for 20 minutes in 2% Helmanex soap water and rinsed extensively with deionized (DI) water. They were then sonicated for 20 minutes in DI water, 20 minutes in acetone, and 20 minutes in isopropyl alcohol, followed by drying under a stream of Nitrogen. The substrates were then UV-ozone cleaned for 5 minutes. A thin layer (30-40 nm) of PEDOT:PSS (Clevios PH) was spin-coated onto each substrate at 4000 RPM for 40 s, followed by 10 minutes of drying at 140^{o}C in air. The samples were then transferred to a Nitrogen glovebox, where the active layers were spin-coated at 1200 RPM for 40 s followed by 2000 RPM for 1 s. The metal cathode was thermally evaporated under vacuum (~10^{-7} torr) through a shadow mask that defines an active area of ~0.03 cm^2. Some of the devices were then thermally annealed by placing the substrates directly on a hot plate. Testing of the devices was performed under a Nitrogen atmosphere with an Oriel Xenon arc lamp having an AM 1.5G solar filter to yield 100 mW cm^{-2} light intensity as calibrated by an NREL certified silicon photocell. During optimization of devices, solution concentrations, solvent choice, donor-acceptor ratios and annealing conditions were varied systematically to obtain the optimized processing and fabrication conditions, and the experiments were repeated multiple times to ensure data reproducibility.

POPT/CNPPV	PCE$_{max}$ = 2%
Bilayer device	
POPT	10 mg/ml chlorobenzene
CNPPV	8 mg/ml THF
Annealing	2 hr at 110^{o}C
Cathode	LiF (1 nm) / Al (100 nm)

P3HT/CNPPV	PCE$_{max}$ = 0.93%
Bilayer device	
P3HT	10 mg/ml chlorobenzene
CNPPV	8 mg/ml THF
Annealing	100 min at 110^{o}C
Cathode	LiF (1 nm) / Al (100 nm)

POPT:EV-BT	PCE$_{max}$ = 1.4%
BHJ device	
POPT:EV-BT	1:1

Blend concentration	20 mg/ml chlorobenzene
Annealing	100 min at 80^{o}C
Cathode	LiF (1 nm) / Al (100 nm)

P3HT:EV-BT	PCE$_{max}$ = 1.1%
BHJ device	
P3HT:EV-BT	1:1
Blend concentration	20 mg/ml chlorobenzene
Annealing	100 min at 80^{o}C
Cathode	LiF (1 nm) / Al (100 nm)

POPT/N2200	PCE$_{max}$ = 0.61%
Bilayer device	
POPT	7.5 mg/ml chlorobenzene
N2200	7.5 mg/ml THF
Annealing	No
Cathode	Al

P3HT/N2200	PCE$_{max}$ = 0.17%
Bilayer device	
P3HT	7.5 mg/ml chlorobenzene
N2200	7.5 mg/ml THF
Annealing	1 hr at 110^{o}C
Cathode	Al

POPT:PDI	PCE$_{max}$ = 0.51%
BHJ device	
POPT:PDI	1:2
Blend concentration	25 mg/ml in dichlorobenzene
Annealing	No
Cathode	Al

P3HT:PDI	PCE$_{max}$ = 0.39%
BHJ device	
See Ref 29 for detailed fabrication procedure.	

PQT-OP/CNPPV	PCE$_{max}$ = 1.12%
Bilayer device	
PQT-DD	5 mg/mL in chlorobenzene
CNPPV	8 mg/mL in ethyl acetate
Annealing	10 minutes at 110 °C
Cathode	LiF (1 nm) / Al (100 nm)

PQT-DD/CNPPV	PCE$_{max}$ = 0.62%
Bilayer device	
PQT-DD	7 mg/mL in chlorobenzene
CNPPV	8 mg/mL in ethyl acetate
Annealing	No
Cathode	LiF (1 nm) / Al (100 nm)

PQT-OP/EV-BT	PCE$_{max}$ = 1.22%
Bilayer device	
PQT-OP	5 mg/mL in chlorobenzene
EV-BT	7 mg/mL in THF
Annealing	140 minutes at 80 °C
Cathode	LiF (1 nm) / Al (100 nm)

PQT-DD/EV-BT	PCE$_{max}$ = 0.62%
Bilayer device	
PQT-DD	12 mg/mL in chlorobenzene
EV-BT	4 mg/mL in THF
Annealing	10 minutes at 110 °C
Cathode	LiF (1 nm) / Al (100 nm)

PQT-OP:PDI	PCE$_{max}$ = 0.88%
BHJ device	
PQT-OP:PDI	1:2
Blend concentration	24 mg/mL in chlorobenzene
Annealing	10 minutes at 110 °C
Cathode	LiF (1 nm) / Al (100 nm)

PQT-DD:PDI	PCE$_{max}$ = 0.49%
BHJ device	
PQT-OP:PDI	1:2
Blend concentration	20 mg/mL in chlorobenzene
Annealing	No
Cathode	LiF (1 nm) / Al (100 nm)

4.6 References

(1) Boudreault, P. L. T.; Najari, A.; Leclerc, M. *Chem. Mater.* **2011**, *23*, 456-469.
(2) Piliego, C.; Holcombe, T. W.; Douglas, J. D.; Woo, C. H.; Beaujuge, P. M.; Fréchet, J. M. J. *J. Am. Chem. Soc.* **2010**.
(3) Thompson, B. C.; Fréchet, J. M. J. *Angew. Chem., Int.Ed.* **2008**, *47*, 58-77.
(4) Chen, H. Y.; Hou, J. H.; Zhang, S. Q.; Liang, Y. Y.; Yang, G. W.; Yang, Y.; Yu, L. P.; Wu, Y.; Li, G. *Nat. Photon.* **2009**, *3*, 649-653.
(5) Anthony, J. E. *Chem. Mater.* **2011**, *23*, 583-590.

(6) Brunetti, F. G.; Gong, X.; Tong, M.; Heeger, A. J.; Wudl, F. *Angew. Chem., Int.Ed.* **2010**, *49*, 532-536.
(7) Shin, R. Y. C.; Kietzke, T.; Sudhakar, S.; Dodabalapur, A.; Chen, Z. K.; Sellinger, A. *Chem. Mater.* **2007**, *19*, 1892-1894.
(8) Lee, M. R.; Eckert, R. D.; Forberich, K.; Dennler, G.; Brabec, C. J.; Gaudiana, R. A. *Science* **2009**, *324*, 232-235.
(9) Holcombe, T. W.; Woo, C. H.; Kavulak, D. F. J.; Thompson, B. C.; Fréchet, J. M. J. *J. Am. Chem. Soc.* **2009**, *131*, 14160-14161.
(10) McNeill, C. R.; Abrusci, A.; Zaumseil, J.; Wilson, R.; McKiernan, M. J.; Burroughes, J. H.; Halls, J. J. M.; Greenham, N. C.; Friend, R. H. *Appl. Phys. Lett.* **2007**, *90*.
(11) Woo, C. H.; Holcombe, T. W.; Unruh, D. A.; Sellinger, A.; Fréchet, J. M. J. *Chem. Mater.* **2010**, *22*, 1673-1679.
(12) Zhou, E. J.; Cong, J. Z.; Wei, Q. S.; Tajima, K.; Yang, C. H.; Hashimoto, K. *Angew.Chem., Int.Ed.* **2011**, *50*, 2799-2803.
(13) Kanai, Y.; Grossman, J. C. *Nano Lett.* **2007**, *7*, 1967-1972.
(14) Woll, C. *Physical and Chemical Aspects of Organic Electronics: From Fundamentals to Functioning Devices; WILEY-VCH: Weinheim*; 2008.
(15) Knipper, M.; Parisi, J.; Coakley, K.; Waldauf, C.; Brabec, C. J.; Dyakonov, V. *Zeitschrift fur Naturforschung Section A-A Journal of Physical Sciences* **2007**, *62*, 490-494.
(16) Mihailetchi, V. D.; Koster, L. J. A.; Blom, P. W. M.; Melzer, C.; de Boer, B.; van Duren, J. K. J.; Janssen, R. A. J. *Adv. Funct. Mater.* **2005**, *15*, 795-801.
(17) Sariciftci, N. S.; Smilowitz, L.; Heeger, A. J.; Wudl, F. *Science* **1992**, *258*, 1474-1476.
(18) Bredas, J. L.; Norton, J. E.; Cornil, J.; Coropceanu, V. *Acct. Chem. Res.* **2009**, *42*, 1691-1699.
(19) Halls, J. J. M.; Walsh, C. A.; Greenham, N. C.; Marseglia, E. A.; Friend, R. H.; Moratti, S. C.; Holmes, A. B. *Nature* **1995**, *376*, 498-500.
(20) Ohkita, H.; Cook, S.; Astuti, Y.; Duffy, W.; Tierney, S.; Zhang, W.; Heeney, M.; McCulloch, I.; Nelson, J.; Bradley, D. D. C.; Durrant, J. R. *J. Am. Chem. Soc.* **2008**, *130*, 3030-3042.
(21) Shoaee, S.; Clarke, T. M.; Huang, C.; Barlow, S.; Marder, S. R.; Heeney, M.; McCulloch, I.; Durrant, J. R. *J. Am. Chem. Soc.* **2010**, *132*, 12919-12926.
(22) Clarke, T. M.; Durrant, J. R. *Chem. Rev.* **2010**, *110*, 6736-6767.
(23) Morteani, A. C.; Sreearunothai, P.; Herz, L. M.; Friend, R. H.; Silva, C. *Phys. Rev. Lett.* **2004**, *92*.
(24) Beljonne, D.; Cornil, J.; Muccioli, L.; Zannoni, C.; Bredas, J. L.; Castet, F. *Chem. Mater.* **2011**, *23*, 591-609.
(25) Granstrom, M.; Petritsch, K.; Arias, A. C.; Lux, A.; Andersson, M. R.; Friend, R. H. *Nature* **1998**, *395*, 257-260.
(26) Ma, W. L.; Yang, C. Y.; Gong, X.; Lee, K.; Heeger, A. J. *Adv. Funct. Mater.* **2005**, *15*, 1617-1622.
(27) Li, G.; Shrotriya, V.; Huang, J. S.; Yao, Y.; Moriarty, T.; Emery, K.; Yang, Y. *Nat. Mater.* **2005**, *4*, 864-868.
(28) Fell, H. J.; Samuelsen, E. J.; Andersson, M. R.; Alsnielsen, J.; Grubel, G.; Mardalen, J. *Synthetic Metals* **1995**, *73*, 279-283.

(29) Rajaram, S.; Armstrong, P. B.; Kim, B. J.; Fréchet, J. M. J. *Chem. Mater.* **2009**, *21*, 1775-1777.

(30) Yan, H.; Chen, Z. H.; Zheng, Y.; Newman, C.; Quinn, J. R.; Dotz, F.; Kastler, M.; Facchetti, A. *Nature* **2009**, *457*, 679-6U1.

(31) Alam, M. M.; Jenekhe, S. A. *Chem. Mater.* **2004**, *16*, 4647-4656.

(32) Kietzke, T.; Horhold, H. H.; Neher, D. *Chem. Mater.* **2005**, *17*, 6532-6537.

(33) Jenekhe, S. A.; Yi, S. J. *Appl. Phys. Lett.* **2000**, *77*, 2635-2637.

(34) Fabiano, S.; Chen, Z.; Vahedi, S.; Facchetti, A.; Pignataro, B.; Loi, M. A. *J. Mater. Chem.* **2011**, *21*, 5891-5896.

(35) Moore, J. R.; Albert-Seifried, S.; Rao, A.; Massip, S.; Watts, B.; Morgan, D. J.; Friend, R. H.; McNeill, C. R.; Sirringhaus, H. *Adv. Energy Mater.* **2011**, *1*, 230-240.

(36) Blom, P. W. M.; Mihailetchi, V. D.; Koster, L. J. A.; Markov, D. E. *Adv. Mater.* **2007**, *19*, 1551-1566.

(37) Goodman, A. M.; Rose, A. *J.Appl.Phys.* **1971**, *42*, 2823-2830.

(38) Vandewal, K.; Tvingstedt, K.; Gadisa, A.; Inganas, O.; Manca, J. V. *Nat. Mater.* **2009**, *8*, 904-909.

(39) Yi, Y.; Coropceanu, V.; Bredas, J. L. *J. Mater. Chem.* **2011**, *21*, 1479-1486.

(40) Yi, Y. P.; Coropceanu, V.; Bredas, J. L. *J. Am. Chem. Soc.* **2009**, *131*, 15777-15783.

(41) Huang, Y. S.; Westenhoff, S.; Avilov, I.; Sreearunothai, P.; Hodgkiss, J. M.; Deleener, C.; Friend, R. H.; Beljonne, D. *Nat. Mater.* **2008**, *7*, 483-489.

(42) Vandewal, K.; Tvingstedt, K.; Gadisa, A.; Inganas, O.; Manca, J. V. *Phys. Rev. B* **2010**, *81*.

(43) Gierschner, J.; Cornil, J.; Egelhaaf, H. J. *Adv. Mater.* **2007**, *19*, 173-191.

(44) Fell, H. J.; Samuelsen, E. J.; Mardalen, J.; Andersson, M. R. *Synthetic Metals* **1995**, *69*, 283-284.

(45) Verploegen, E.; Mondal, R.; Bettinger, C. J.; Sok, S.; Toney, M. F.; Bao, Z. A. *Adv. Funct. Mater.* **2010**, *20*, 3519-3529.

(46) Thompson, B. C.; Kim, B. J.; Kavulak, D. F.; Sivula, K.; Mauldin, C.; Fréchet, J. M. J. *Macromolecules* **2007**, *40*, 7425-7428.

(47) Chen, S. A.; Chang, E. C. *Macromolecules* **1998**, *31*, 4899-4907.

(48) Chen, S. H.; Su, C. H.; Su, A. C.; Chen, S. A. *J. Phys. Chem. B* **2004**, *108*, 8855-8861.

(49) Valiev, M.; Bylaska, E. J.; Govind, N.; Kowalski, K.; Straatsma, T. P.; Van Dam, H. J. J.; Wang, D.; Nieplocha, J.; Apra, E.; Windus, T. L.; de Jong, W. *Computer Physics Communications* **2010**, *181*, 1477-1489.

(50) Wu, Q.; Van Voorhis, T. *Phys. Rev. A* **2005**, *72*.

(51) Wu, Q.; Van Voorhis, T. *J. Phys. Chem. A* **2006**, *110*, 9212-9218.

(52) Wu, Q.; Van Voorhis, T. *J. Chem. Theory Comp.* **2006**, *2*, 765-774.

(53) Vandewal, K.; Gadisa, A.; Oosterbaan, W. D.; Bertho, S.; Banishoeib, F.; Van Severen, I.; Lutsen, L.; Cleij, T. J.; Vanderzande, D.; Manca, J. V. *Adv. Funct. Mater.* **2008**, *18*, 2064-2070.

(54) Goris, L.; Haenen, K.; Nesladek, M.; Wagner, P.; Vanderzande, D.; De Schepper, L.; D'Haen, J.; Lutsen, L.; Manca, J. V. *J. Mater. Sci.* **2005**, *40*, 1413-1418.

(55) Goris, L.; Poruba, A.; Hod'akova, L.; Vanecek, M.; Haenen, K.; Nesladek, M.; Wagner, P.; Vanderzande, D.; De Schepper, L.; Manca, J. V. *Appl. Phys. Lett.* **2006**, *88*.

(56) Lee, J.; Vandewal, K.; Yost, S. R.; Bahlke, M. E.; Goris, L.; Baldo, M. A.; Manca, J. V.; Van Voorhis, T. *J. Am. Chem. Soc.* **2010**, *132*, 11878-11880.
(57) Zhu, X. Y.; Yang, Q.; Muntwiler, M. *Acct. Chem. Res.* **2009**, *42*, 1779-1787.
(58) Loi, M. A.; Toffanin, S.; Muccini, M.; Forster, M.; Scherf, U.; Scharber, M. *Adv. Funct. Mater.* **2007**, *17*, 2111-2116.
(59) Veldman, D.; Ipek, O.; Meskers, S. C. J.; Sweelssen, J.; Koetse, M. M.; Veenstra, S. C.; Kroon, J. M.; van Bavel, S. S.; Loos, J.; Janssen, R. A. J. *J. Am. Chem. Soc.* **2008**, *130*, 7721-7735.

Chapter 5

Incorporation of Furan into Low Band Gap Polymers for Efficient Solar Cells[3]

Abstract

The design, synthesis, and characterization of the first examples of furan-containing low band gap polymers (PDPP2FT and PDPP3F) with substantial power conversion efficiencies in organic solar cells is reported. Substituting thiophene units with furans in the conjugated backbone does not compromise the optical and electronic properties of these low band gap polymers. In addition, inserting furan moieties in the backbone enables the use of less bulky solubilizing side-chains due to the significant contribution of the furan rings to overall polymer solubility in common organic solvents. Bulk heterojunction solar cells fabricated from furan containing polymers and $PC_{71}BM$ as the acceptor show high power conversion efficiencies over 6%.

---

[3] Reproduced in part with permission from Woo, C. H.; Beaujuge, P.M.; Holcombe, T. W.; Lee, O. P.; , J. M. J. *Journal of the American Chemical Society* **2010**, *132*, 15547-15549. Copyright 2010 American Chemical Society.

5.1 Introduction

In the past decade, the field of OPVs has focused much attention on polythiophenes, particularly P3HT, because of their early success in solar cell performance.[1,2] However, the maximum achievable efficiency of P3HT-based solar cells is limited to 5% due to its non-optimal band gap and energy levels.[3] To overcome this limitation, recent research efforts have focused on the development of low band gap donor polymers that have broad absorption spectra and have the potential to out-perform P3HT.[4-6] The search for new building blocks for semiconducting polymers continues as we gain mechanistic understandings and establish design rules relevant to organic electronic applications.[3,7,8] For example, the ideal polymer should (i) have sufficient energy level offsets with fullerenes for efficient charge separation while maximizing the open circuit voltage,[3,9] (ii) display an absorption spectrum extending across the visible spectrum and into the near-IR, and (iii) maintain high extinction coefficients over this spectral range.[7] At the same time, it has become increasingly apparent that a balance among the competing effects of solution processability, miscibility with the fullerene component, and solid state packing needs to be established.[10-12] Both the chemical structure of the backbone repeat units and the choice of the solubilizing side-chains critically impact the above-mentioned criteria.[13,14] For example, while the use of longer and bulkier alkyl substituents improves solubility, it also increases lamellar and π-stacking distances, hindering intermolecular ordering, and affecting the transport of charge carriers across the polymer stacks.[13,15,16] In this regard, strategies to reduce the length, bulkiness, and density of solubilizing side-chains along the conjugated polymer backbone are well worth exploring.

A survey of state-of-the-art BHJ solar cells reveals that most high performance polymers reported so far rely on thiophene or thiophene-based heterocycles.[17-23] While thiophene-based conjugated materials have attracted much attention in the area of organic electronics, only a limited number of studies have examined furan-containing materials potentially useful for device applications.[24-26] Recently, furans have been used as an alternative to thiophenes in organic dyes for dye-sensitized solar cells and have shown very similar optical and electronic properties.[27,28] Furan-based heterocycles have also been introduced as peripheral substituents in one of the highest performing small molecule photovoltaics.[29] The sparsity of studies examining polymer backbones containing furans in this field is surprising given that furans exhibit similar energy levels and a comparable degree of aromaticity relative to their thiophene counterparts.[24,30] Importantly, furan derivatives can be synthesized from a variety of natural products, hence they fall into the category of renewable and sustainable synthetic resources.

5.2 Results and Discussion

We demonstrate that furan heterocycles can be advantageously incorporated into conjugated polymer backbones without hindering their photovoltaic device performance. In addition, we show that furans can be employed to dramatically reduce the amount of aliphatic side-chain material necessary to solubilize polymer backbones that otherwise require the presence of long and bulky substituents. This concept is exemplified by the synthesis and characterization of two furan-containing semiconducting polymers: PDPP2FT and PDPP3F (Figure 5.1a). These polymers contain a diketopyrrolopyrrole (DPP) unit[22,31-33] and are structurally analogous to the low band gap polymer PDPP3T previously reported by Janssen et al.[34]. Importantly, these furan-containing derivatives were synthesized with 2-ethylhexyl substituents as well as linear alkyl substituents whereas PDPP3T (as initially reported[34]) was appended with large and bulky 2-hexyldecyl solubilizing groups.

5.2.1 Polymer Characterization

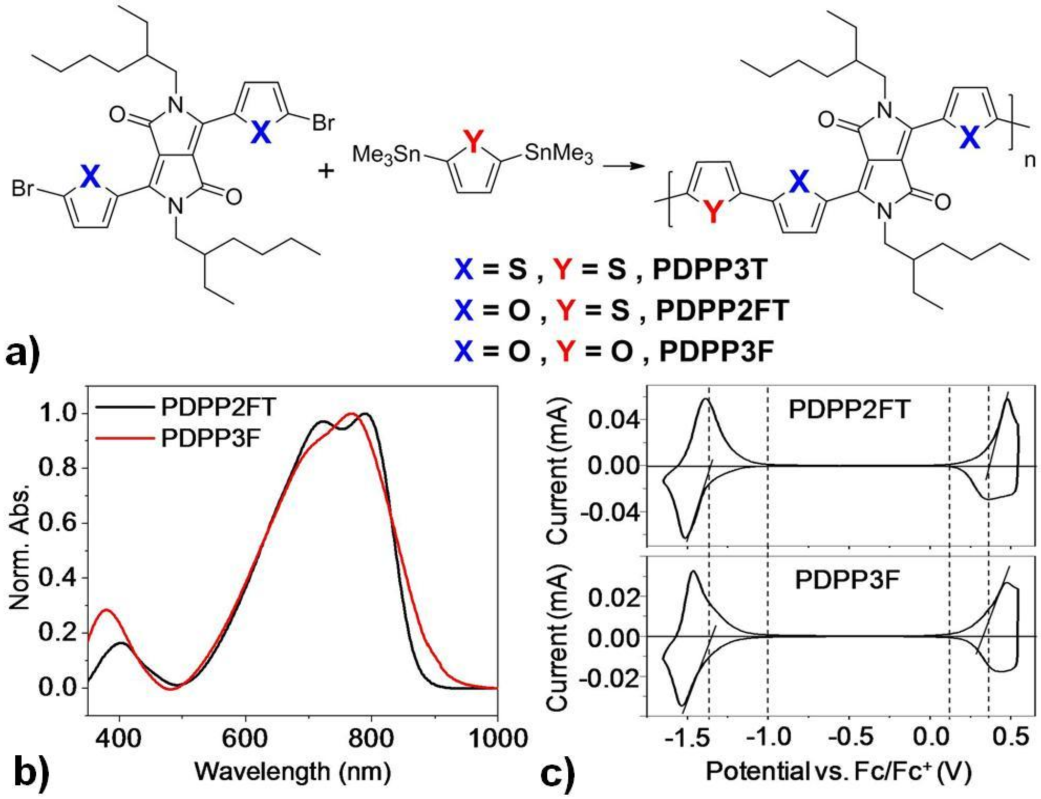

Figure 5.1. a) Synthetic scheme and polymeric structures used in this study (polymerization protocol: Pd_2dba_3, P(o-tol)$_3$, chlorobenzene, 110°C, 24h). b) Thin film absorption spectra and c) cyclic voltammograms of PDPP2FT and PDPP3F.

While exploring the use of furans as alternatives to thiophenes in low band gap conjugated polymers containing DPP, we found that soluble high molecular weight PDPP2FT could be readily obtained (M_n = 66 kDa). The use of 2-ethylhexyl substituents was sufficient to impart PDPP2FT with appropriate solubility in common organic solvents (*e.g.* tetrahydrofuran, chloroform, chlorobenzene) for device fabrication. In contrast, the all-furan derivative PDPP3F synthesized using the same polymerization protocol (M_n = 29 kDa, see SI) was found to possess slightly reduced solubility in the same organic solvents. While the improved solubility of oligofurans over oligothiophenes has been reported,[35] it appears that the ratio of furan to thiophene in mixed oligomers also impacts solubility.[36,37] As a control experiment, we attempted to synthesize the 2-ethylhexyl substituted derivative of the all-thiophene PDPP3T following the same polymerization procedure as that used for PDPP2FT and PDPP3T. However, the polymerization yielded only low molecular weight fractions minimally soluble in all common organic solvents (M_n = 2 kDa).

The onset of optical absorption of PDPP2FT in thin film was measured to be 880 nm (E_g = 1.41 eV) while the λ_{max} was observed at 789 nm (See Figure 5.1b), which is comparable to the optical properties of PDPP3T reported earlier by Janssen et al. (E_g = 1.3 eV)[34]. PDPP3F also possesses similar optical properties with E_g = 1.35 eV and λ_{max} at 767 nm. Figure 1c shows the cyclic voltammograms of the two polymers. The onsets of oxidation and reduction of PDPP2FT were observed at +0.28 and -1.34 V vs. Fc/Fc$^+$, corresponding to HOMO and LUMO levels at -5.4 eV and -3.8 eV vs. vacuum. For PDPP3F, the onsets were observed at +0.35 and -1.34 V, corresponding to HOMO and LUMO levels at -5.5 and -3.8 eV. These values are comparable to those obtained for the low molecular weight all-thiophene analog PDPP3T (Figure 5.2). These results confirm that substituting furans for thiophenes in the polymer backbone do not significantly affect the optical and electronic properties of the polymer.

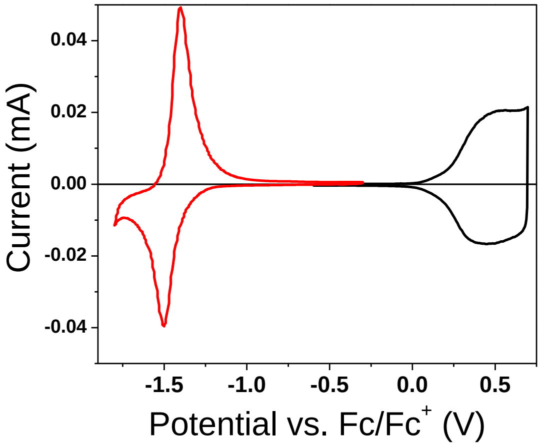

Figure 5.2. Cyclic voltammogram of PDPP3T. The onsets of oxidation and reduction were estimated to be 0.19 V and -1.39 V, corresponding to HOMO and LUMO levels of 5.3 eV and 3.7 eV respectively.

5.2.2 Solar Cell Performance

Solar cells were fabricated using PDPP2FT as the electron donor and [6,6]-phenyl-C_{61}-butyric acid methyl ester ($PC_{61}BM$) as the electron acceptor with the device structure ITO/ PEDOT:PSS/polymer:PCBM/LiF/Al. The active layers were spin-coated from chlorobenzene, and, in some cases, a small amount of the high boiling point additive 1-chloronaphthalene (CN) was added to optimize blend morphology for enhanced device performance. The *J-V* curves and external quantum efficiency (EQE) spectra of PDPP2FT:$PC_{61}BM$ devices are shown in Figure 5.3. Without any post-fabrication treatment, the PDPP2FT:$PC_{61}BM$ device spin-coated from pure chlorobenzene afforded 3.4% PCE under AM 1.5G, 100 mW cm^{-2} illumination. The use of chlorobenzene containing 1 vol% CN for spin-coating led to a slight improvement to 3.7% PCE, mostly through an increase in the photocurrent. The best device was obtained from a blend of PDPP2FT:$PC_{61}BM$ in a 1:3 weight ratio and gave a PCE of 3.8%, with an open circuit voltage (V_{oc}) of 0.76 V, a short-circuit current density (J_{sc}) of 9.0 mA cm^{-2}, and a fill factor (FF) of 55%. Table 5.1 shows the parameters of the average and best devices fabricated from PDPP2FT and $PC_{61}BM$ blend. The EQE showed a sharp onset at the optical band gap of the polymer and reached a maximum value of 33%.

Table 5.1 Device parameters of PDPP2FT:PC$_{61}$BM BHJ devices shown in Figure 5.3.

1:3 PDPP2FT:PC$_{61}$BM	**V_{oc}**	**J_{sc} (mA cm^{-2})**	**FF**	**PCE (%)**
No additive	0.76	7.8	0.57	3.4 (3.6)
1 vol% CN	0.76	8.9	0.54	3.7 (3.8)

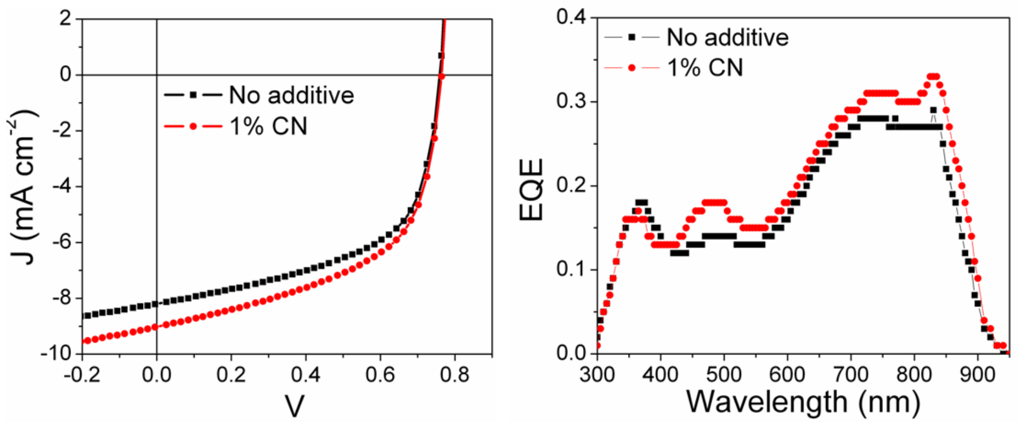

Figure 5.3. *J-V* curves and EQE spectra of optimized 1:3 PDPP2FT:PC$_{61}$BM BHJ devices fabricated without additive and with 1 vol% CN.

To increase the breadth of the photoactive spectrum and the overall photocurrent, we fabricated solar cells with the more light-absorbing fullerene derivative PC$_{71}$BM. Figure 5.4 shows the *J-V* curves and the EQE spectra of optimized devices fabricated from blends of PDPP2FT:PC$_{71}$BM at a 1:3 weight ratio in chlorobenzene. Interestingly, without any additive, the PC$_{71}$BM devices performed poorly with an average PCE of only 0.86%. However, with the addition of high boiling additive CN to the blend solution, device performance improved by more than fivefold with much higher J_{sc} and an average PCE of 4.7% (Table 5.2). The best device was obtained with the addition of 9% CN by volume relative to chlorobenzene, and it achieved a V_{oc} of 0.74 V, a J_{sc} of 11.2 mA cm^{-2}, a FF of 60%, and a PCE of 5.0%, a result comparable to that obtained by Janssen *et al.* with PDPP3T[34]. The J_{sc} value calculated from the integration of the EQE spectrum of the best device is 11.4 mA cm^{-2}, which closely matches the J_{sc} value obtained from the *J-V* measurement under white light illumination.

Table 5.2 Device parameters of PDPP2FT:PC$_{71}$BM BHJ devices shown in Figure 5.4.

1:3 PDPP2FT:PC$_{71}$BM	**V_{oc}**	**J_{sc} (mA cm^{-2})**	**FF**	**PCE (%)**
No additive	0.73	2.63	0.45	0.86 (0.96)
9 vol% CN	0.75	10.7	0.59	4.7 (5.0)

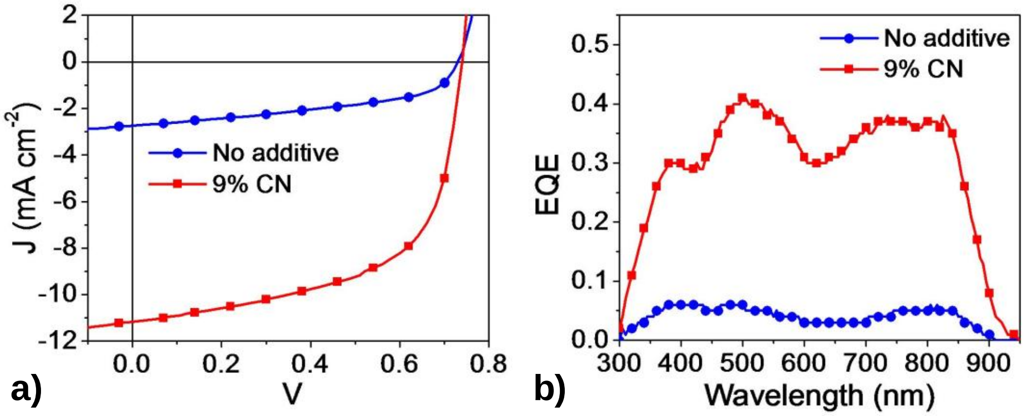

Figure 5.4. a) *J-V* curves of optimized PDPP2FT:PC$_{71}$BM devices spin-coated out of chlorobenzene (with no additive and with 9 vol% CN). b) External quantum efficiency spectra of optimized devices.

The all-furan PDPP3T derivative also showed promising OPV performance. For BHJ devices containing PDPP3F, chloroform was found to be a better solvent. Figure 5.5 and Table 5.3 summarize the results of solar cells containing PDPP3F blended with fullerene derivatives as the acceptor. Here again, the effect of adding a small amount of CN to the blend solution prior to spin coating is dramatic. With no additive, PDPP3F:PC$_{61}$BM solar cells achieved a low average PCE of 0.41%, whereas devices with 5 vol% CN show a much higher efficiency of 3% (max 3.4%). Similarly, the average efficiency of PDPP3F:PC$_{71}$BM devices was 0.36% with no additive but improved to 3.8% (max 4.1%) with 5 vol% CN. The high fill factors of these devices suggest that the furan polymers have a high charge carrier mobility and the optimized devices contain a favorable morphology containing interpenetrating pathways for efficient charge extraction. Overall, these device results strongly support the potential of furan-based polymeric materials in OPVs.

Table 5.3 Device parameters of PDPP3F solar cells shown in Figure 5.5.

	V$_{oc}$	**J$_{sc}$ (mA cm^{-2})**	**FF**	**PCE (%)**
1:3 PDPP3F:PC$_{61}$BM				
No additive	0.73	1.2	0.45	0.41 (0.47)
5 vol% CN	0.74	6.8	0.58	3.0 (3.4)
1:3 PDPP3F:PC$_{71}$BM				
No additive	0.73	0.93	0.53	0.36 (0.41)
5 vol% CN	0.73	9.1	0.58	3.8 (4.1)

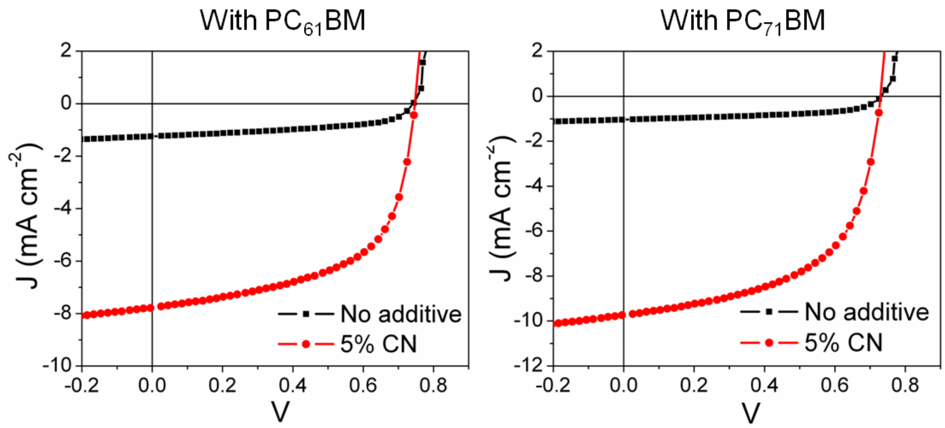

Figure 5.5. *J-V* curves of optimized 1:3 PDPP3F:$PC_{61}BM$ (left) and 1:3 PDPP3F:$PC_{71}BM$ (right) fabricated without additive and with 5 vol% CN.

To further investigate the potential of furan-containing low band gap polymers in OPVs, we optimized the structure of the solubilizing side chains on PDPP2FT. This is important because the choice of the solubilizing side group not only affects the solution processibility of the polymer, but also its miscibility with the fullerene acceptor and its solid state packing. In addition to the 2-ethylhexyl (EH) side chain, we explored the option of using a linear alkyl chain as well as a larger branched unit. A PDPP2FT derivative with a linear tetradecyl (C14) chain was synthesized. The long C14 chain was necessary to impart sufficient solubility to the polymer for device fabrication. We also explored a derivative with a 2-butyloctyl (BO) side group. Both polymers were synthesized using the same procedure as that of the original EH derivative. Figure 5.6 shows the structure of all three polymers.

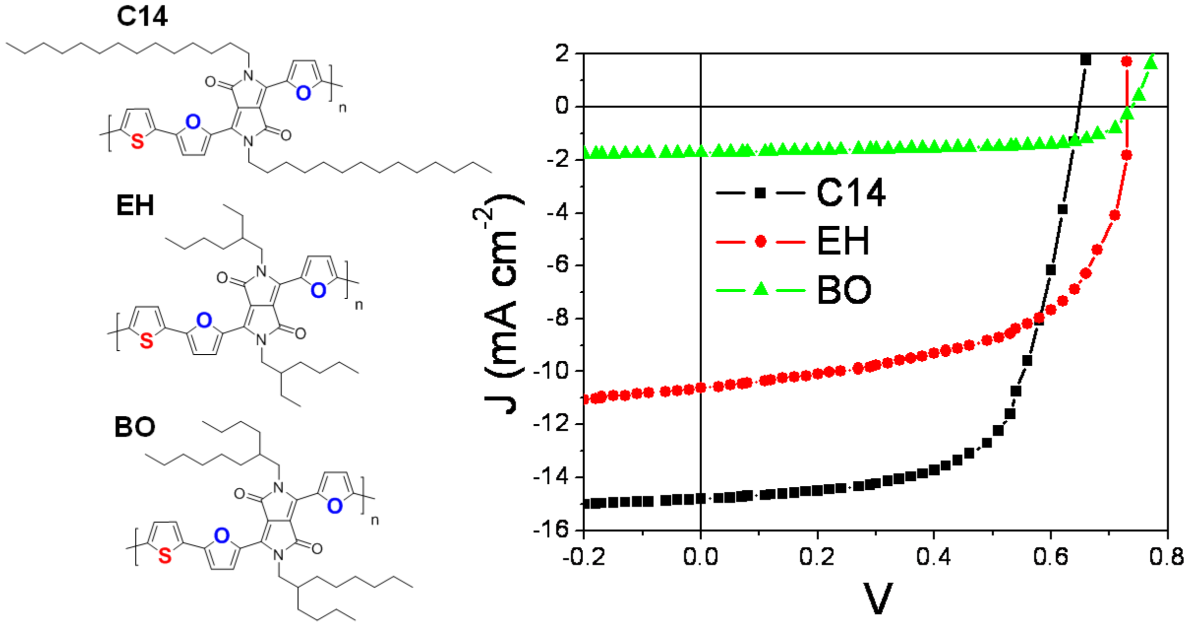

Figure 5.6. The molecular structure and optimized photovoltaic device performance of three PDPP2FT derivatives with different solubilizing side chains (C14 = tetradecyl, EH = 2-ethylhexyl, BO = 2-butyloctyl).

Table 5.4 Device parameters of PDPP2FT:$PC_{71}BM$ BHJ devices shown in Figure 5.6.

1:3 PDPP2FT:$PC_{71}BM$	**V_{oc}**	**J_{sc} (mA cm^{-2})**	**FF**	**PCE (%)**
Tetradecyl (C14)	0.65	14.8	0.64	6.2
2-ethylhexyl (EH)	0.75	10.7	0.59	4.7
2-butyloctyl (BO)	0.74	1.7	0.67	0.84

Figure 5.6 and Table 5.4 summarize the solar cell performance of the three PDPP2FT derivatives. The devices were independently optimized, and the best devices were achieved by using a small amount of CN additive during spin coating. Clearly, the choice of the solubilizing group significantly affects device performance. The C14 polymer generated 6% solar cells with a high J_{sc} of 13.6 mA cm^{-2}. The use of a linear chain allows tighter π-π stacking between polymer chains in the solid state and leads to better charge transport compared to the branched EH derivative. In contrast, the BO polymer displayed worse device performance with a low efficiency of only 0.84%. In this case, the more branched BO side group probably inhibits the extent of π-π stacking in the polymer and results in reduced device performance compared to both the EH and the C14 derivative.

5.2.3 Effect of Additives

In most of the devices shown here, adding a small amount of CN additive improves overall device efficiency. The dramatic difference in device performance with and without the CN additive is most likely due to the optimization of blend morphology. Figure 5.7 compares the atomic force microscopy (AFM) images of blend films of PDPP2FT(EH):$PC_{71}BM$ at the optimized ratio. The blend without additive exhibits coarse phase separation between the polymer and $PC_{71}BM$ with large micron-sized domains. In contrast, the addition of CN led to much finer phase separation between the two materials and the formation of fiber-like interpenetrating morphologies at the length scale of ~ 20 nm, which is close to the ideal domain size assuming an exciton diffusion length of 5-10 nm.[38-40] The thin film absorption of PDPP2FT also redshifts and displays more distinct vibronic structures when CN is added to the solution before spin-coating (see Figure 5.8). The redshift in absorption is indicative of increased intermolecular ordering and planarity in the polymer backbone and could be another reason for the improved performance of devices fabricated with CN.

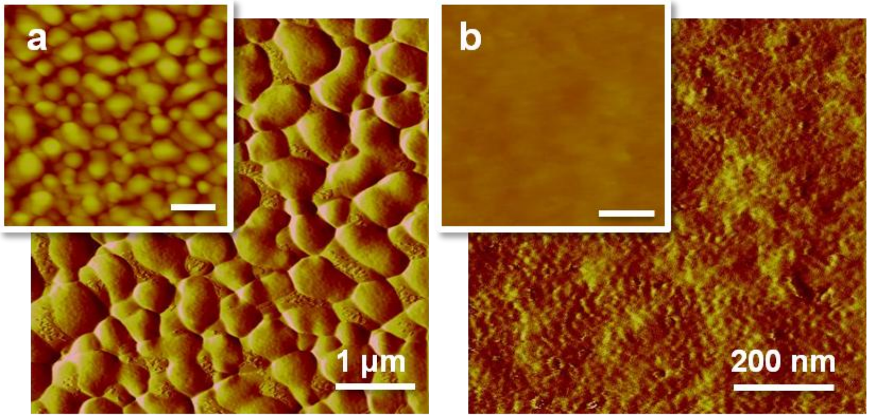

Figure 5.7. AFM phase images of 1:3 PDPP2FT:$PC_{71}BM$ blend films spin-coated (a) from chlorobenzene only and (b) from chlorobenzene + 9 vol% CN. (Inset: height images of the same films. The data scale is 0-60 nm.).

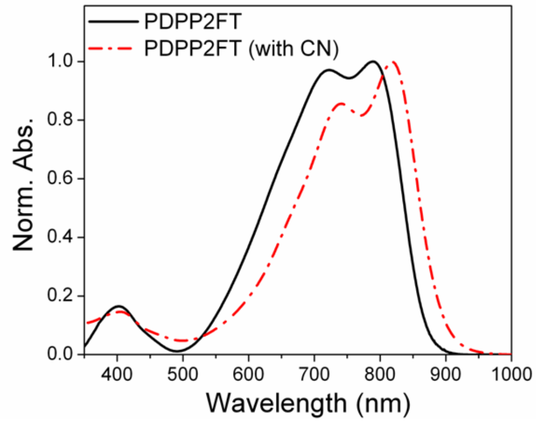

Figure 5.8. Absorption spectra of PDPP2FT thin films as spun from pure chlorobenzene and from chlorobenzene with 5 vol% CN added.

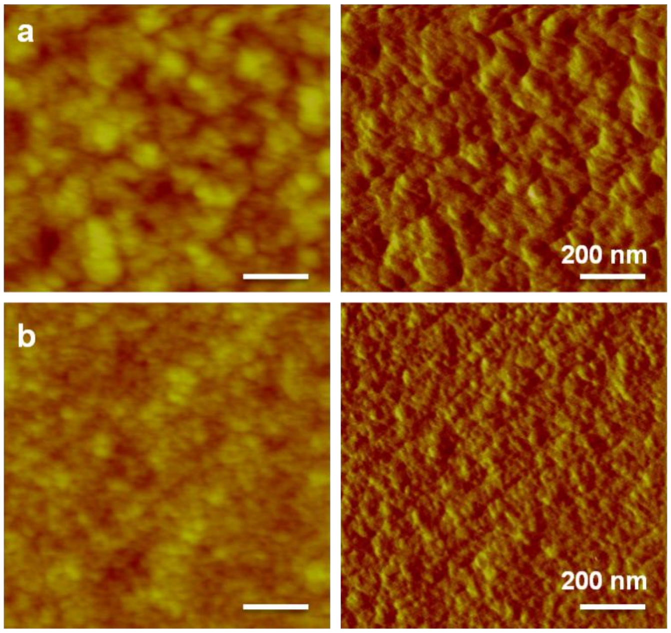

Figure 5.9. AFM height (left) and phase images (right) of PDPP2FT:PC$_{61}$BM blends at 1:3 ratio by weight. a) spun from chlorobenzene only. b) spun from chlorobenzene + 1 vol% CN.

5.3 Conclusion

Furans can be advantageously used as an alternative to thiophenes and thiophene-based building units in the design and synthesis of low band gap conjugated polymers with efficient solar cell performance. The polymers examined (PDPP2FT and PDPP3F) exhibit near-identical optical and electronic properties, and demonstrate power conversion efficiencies of 4-5% in BHJ devices with PC$_{71}$BM. The insertion of furan within the conjugated backbone allowed for shorter solubilizing alkyl chains to be used, compared to the large and bulky solubilizing groups required to solubilize the all-thiophene polymer PDPP3T. In particular, polymer solubility was found to improve substantially when a combination of thiophene and furan heterocycles is incorporated. In addition, by optimizing the choice of the solubilizing groups on the polymer, we were able to achieve over 6% power conversation efficiency in solar cells fabricated from a PDPP2FT derivative with a linear C14 side chain. These results clearly demonstrate the potential of furans as thiophene alternatives in the design of highly performing organic solar cell materials, paving the path for the design and production of organic electronic materials from sustainable synthetic resources.

5.4 Experimental

5.4.1 Synthetic Details

All reagents from commercial sources were used without further purification, unless otherwise noted. Flash chromatography was performed using Silicycle SiliaFlash ® P60 (particle size 40-63 µm, 230 – 400 mesh) silica gel. Dimethylformamide (DMF) and Tetrahydrofuran (THF) were purchased from Fisher Scientific, and each was purified by passing it under N_2 pressure through two packed columns of neutral alumina. All compounds were characterized by ^{1}H NMR (400 MHz) and ^{13}C NMR (100 MHz) on a Bruker AVB-400 or AVQ-400 instrument. All NMR spectra were acquired at room temperature unless otherwise noted. Data from high-resolution mass spectrometry (HRMS) using electron impact (EI) were obtained by the UC Berkeley mass spectrometry facility. Matrix assisted laser desorption/ionization mass spectrometry (MALDI-TOF MS) was performed on a PerSeptive Biosystems Voyager-DE using 2,2':5',2''-terthiophene as the matrix. Samples were prepared by diluting the monomers in chloroform with the matrix. For polymer molecular weight determination, polymer samples were dissolved in HPLC grade chloroform at a concentration of 1 mg/ml, briefly heated and then allowed to return to room temperature prior to filtering through a 0.2 µm PVDF filter. SEC was performed using HPLC grade chloroform at a flow rate of 1.0 mL/min on two 300 x 8 mm linear S SDV, 5 µm columns (Polymer Standards Services, USA Inc.) at 30 ºC using a Waters (Milford, MA) separation module and a Waters 486 Tunable Absorption Detector monitored at 254 nm. The instrument was calibrated vs. polystyrene standards (580 – 96,000 Da) and data was analyzed using Millenium 3.2 software.

Scheme 5.1

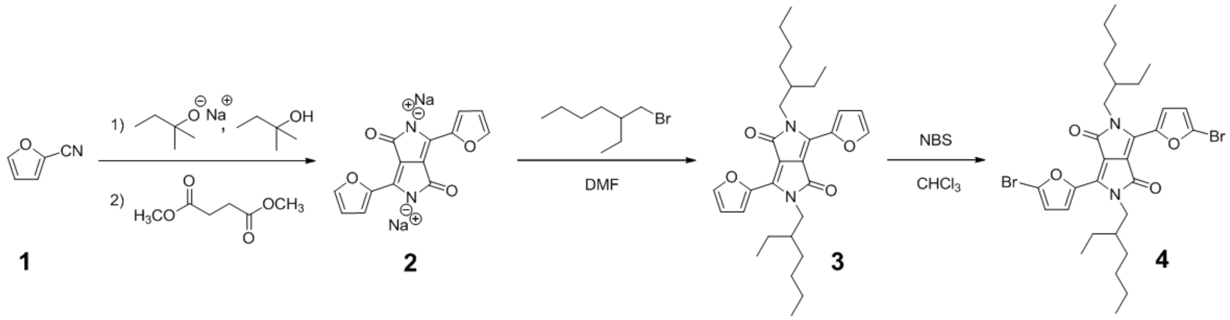

3,6-di(furan-2-yl)pyrrolo[3,4-c]pyrrole-1,4(2H,5H)-dione (2): A 500 mL three-neck round-bottom flask connected to a condenser and dry nitrogen flow was charged with a stir bar and *tert*-amyl alcohol (250 mL). Sodium metal pieces (2.47 g, 107 mmol) were progressively added to the warmed solution of *tert*-amyl alcohol (60-70 °C). After complete addition of the sodium, the temperature was progressively raised to 120 °C. The mixture was stirred overnight at 120 °C. Furan-2-carbonitrile (**1**) (10.0 g, 107 mmol) was subsequently added to the hot mixture of sodium alkoxide. Dimethyl succinate (5.23 g, 35.8 mmol) was then added dropwise over a period of 20 min (the reaction mixture turned dark orange-red), and the resulting mixture was stirred for 1.5 h. The reaction mixture was then cooled to room temperature, and the precipitated sodium salt **2** was filtered over a Buchner funnel for collection and dried under vacuum (14.7 g, 87% yield). Compound **2** was used without further purification.

2,5-bis(2-ethylhexyl)-3,6-di(furan-2-yl)pyrrolo[3,4-c]pyrrole-1,4(2H,5H)-dione (3): Compound **2** (3.36 g, 10.8 mmol) and 100 mL of dry DMF were added to a 250 mL two-neck round–bottom flask, equipped with a condenser and stir-bar and placed under N_2 atmosphere. The mixture was heated to 120 °C, stirred for 30 min, and 2-ethylhexylbromide (6.05 g, 31.3 mmol) was then added quickly (while at 120 °C). The reaction mixture was subsequently stirred at 140 °C for *ca.* 6 h, and cooled to room temperature. The organic phase was extracted with diethyl ether and washed with water. The diethyl ether was evaporated, and the resulting tacky solid (red) was purified by column chromatography using $CHCl_3$ as eluent. 1.30 g of **3** were isolated (25% yield). ^{1}H NMR (400 MHz, $CDCl_3$): δ (ppm) = 8.33 (d, *J* = 3.6 Hz, 2 H), 7.61 (d, *J* = 1.3 Hz, 2 H), 6.69 (dd, *J* = 1.7 Hz, 3.6 Hz, 2 H), 4.04 (d, *J* = 7.8 Hz, 4 H), 1.80 – 1.68 (m, 2 H), 1.39 – 1.26 (m, 16 H), 0.95 – 0.85 (m, 12 H). ^{13}C (100 MHz, $CDCl_3$): δ (ppm) = 161.4, 145.0, 144.8, 134.1, 120.4, 113.6, 106.6, 46.3, 40.1, 30.7, 28.8, 24.0, 23.2, 14.2, 10.9. MALDI-TOF MS (*m/z*): calc'd for $C_{30}H_{40}N_2O_4$ [M^+] = 492.3; found 492.9.

3,6-bis(5-bromofuran-2-yl)-2,5-bis(2-ethylhexyl)pyrrolo[3,4-c]pyrrole-1,4(2H,5H)-dione (4): Compound **3** (1.01 g, 2.05 mmol) was charged in a 100 mL single-neck round–bottom flask filled with 50 mL of $CHCl_3$. The mixture was cooled to 0 °C and stirred while *N*-bromosuccinimide (NBS) was added in small portions. The mixture was allowed to warm to room temperature and stirred for 2 h following complete addition of NBS. The organic phase was extracted with $CHCl_3$ and washed with water. The $CHCl_3$ was evaporated, and the resulting tacky solid (dark red) was purified by column chromatography using $CHCl_3$ as eluent. 0.95 g of **4** were isolated (71% yield). ^{1}H NMR (400 MHz, $CDCl_3$): δ (ppm) = 8.30 (d, *J* = 3.7 Hz, 2 H), 6.62 (d, *J* = 3.7 Hz, 2 H), 3.99 (add, *J* = 2.7 Hz, 7.4 Hz, 4 H), 1.78 – 1.68 (m, 2 H), 1.39 – 1.24 (m, 16 H), 0.92 (t, *J* = 7.5 Hz, 6 H), 0.88 (t, *J* = 7.0 Hz, 6 H). ^{13}C (100 MHz, $CDCl_3$): δ (ppm) = 161.1, 146.4, 132.9, 126.4, 122.4, 115.7, 106.4, 46.4, 40.2, 30.7, 28.9, 23.9, 23.3, 14.2, 10.8. MALDI-TOF MS (*m/z*): calc'd for $C_{30}H_{38}Br_2N_2O_4$ [M^+] = 648.1; found 648.3.

Scheme 5.2

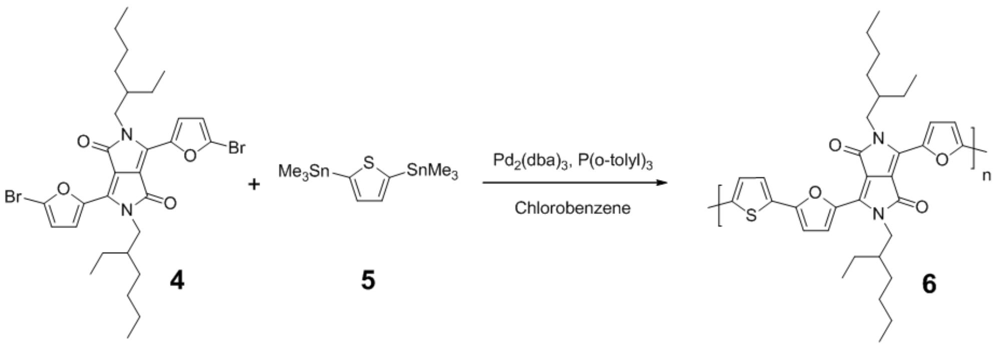

PDPP2FT (6): **4** (200 mg, 0.307 mmol), 2,5-bis(trimethylstannyl)-thiophene (**5**) (126 mg, 0.307 mmol), $Pd_2(dba)_3$ (2 mol %) and $P(o\text{-}tol)_3$ (8 mol %) were charged with a 50 mL Schlenk tube, cycled with N_2 and subsequently dissolved in 6 mL of degassed chlorobenzene. The mixture was stirred for 24 h at 110 °C. The reaction mixture was allowed to cool to 55 °C, 15 mL of $CHCl_3$ was added, and the strongly complexing ligand *N,N*-diethylphenylazothioformamide (CAS# 39484-81-6) was subsequently added (as a palladium scavenger). The resulting mixture was stirred for 1 h at 55°C, and precipitated into methanol (200 mL). The precipitate was filtered through a Soxhlet thimble and purified via Soxhlet extraction for 12 h with methanol and 1 h with hexanes, followed by collection in chloroform. The chloroform solution was then passed through a plug of silica, neutral alumina, and celite (1:1:1), concentrated by evaporation and precipitated into methanol (200 mL). The polymer **6** was filtered off as a dark solid (162 mg). SEC analysis: M_n = 66 kDa, PDI = 2.05.

Scheme 5.3

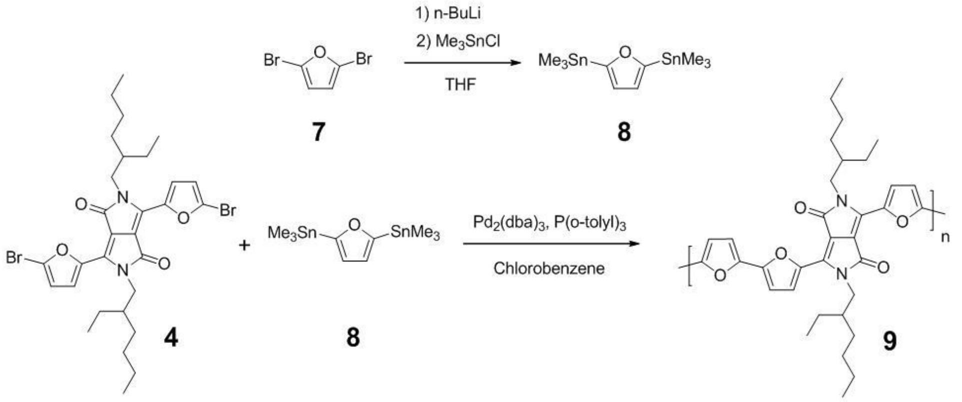

2,5-bis(trimethylstannyl)furan (8): Compound **7** (2.0 g, 8.85 mmol) and 30 mL of dry THF were added to a 100 mL two-neck round–bottom flask with stir bar, and placed under N_2 atmosphere. The mixture was cooled to -78 °C, and *n*-BuLi (2.5 M in hexanes) (18.2 mmol, 7.4 mL) was added dropwise over 30 min (while at -78 °C). Following complete addition of *n*-BuLi, the reaction mixture was stirred for an additional 15 min at -78 °C. It was subsequently allowed to reach room temperature and stirred for 1 h. The reaction mixture was cooled down to -78 °C, Me_3SnCl (18.6 mmol, 3.70 g) was charged all at once, and the mixture was stirred at -78 °C for 15 min. It was then allowed to reach room temperature and stirred for 12 h. The organic phase was extracted with diethyl ether and washed with water. Diethyl ether was evaporated, and the resulting oil (yellow) was passed through a plug of basic alumina using hexanes as eluent. Hexanes were evaporated, and the resulting oil (colorless) was distilled under reduced pressure (68-72 °C at 180 mTorr) and 0.74 g of **8** were isolated (21% yield). ^1H NMR (400 MHz, $CDCl_3$): δ (ppm) = 6.71 (s, 2 H), 0.40 (m, 18 H). ^{13}C (100 MHz, $CDCl_3$): δ (ppm) = 165.2, 120.3, -9.0.

PDPP3F (9): The same polymerization and purification protocols as those described for **PDPP2FT (6)** were followed. Polymer **9** was collected as a dark and brittle solid (58 mg). SEC analysis: M_n = 29 kDa, PDI = 2.02.

Scheme 5.4

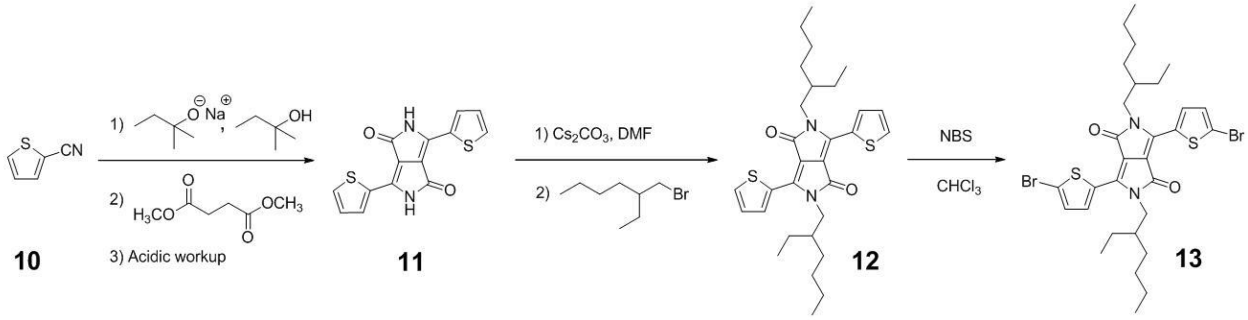

3,6-di(thien-2-yl)pyrrolo[3,4-c]pyrrole-1,4(2H,5H)-dione (11). A 500 mL three-neck flask connected to a condenser was charged with a stir bar and *tert*-amyl alcohol (250 mL). Sodium metal (2.56 g, 108 mmol) immersed in mineral oil was thoroughly washed with hexanes and cut into small pieces. The sodium metal pieces were slowly added to the reaction mixture over a 1.5 h period while the temperature was slowly increased to 120 °C over the same amount of time. After all the sodium metal pieces were dissolved, compound **10** (11.9 g, 108 mmol) was added to the reaction. As dimethyl succinate (5.29 g, 36.2 mmol) was added dropwise to the reaction mixture over 1 h, the solution turned dark red. The reaction contents were stirred at 120 °C for 2 h, and then precipitated into acidic MeOH (400 mL MeOH and 20 mL conc. HCl). Filtration of the suspension through a Buchner funnel yielded **11** as a dark red solid (9.10 g), which was used in subsequent reactions without further purification (83 % yield).

2,5-bis(2-ethylhexyl)-3,6-di(thien-2-yl)pyrrolo[3,4-c]pyrrole-1,4(2H,5H)-dione (12). A 250 mL of round bottom flask was charged with **11** (4.50 g, 15.0 mmol), cesium carbonate (14.6 g, 45.0 mmol) and dry DMF (150 mL). The reaction contents were stirred at 120 °C for 3 h before 2-ethylhexyl bromide (7.24 g, 37.5 mmol) was added to the mixture. After the reaction mixture was heated at 130 °C for 20 h, it was filtered through qualitative filter paper into a 500 mL round-bottom flask to remove salt byproducts. The solvent was removed from the crude product under reduced pressure. The crude material was purified by flash chromatography ($CHCl_3$) to yield 1.24 g of **12** as a dark red-purple tacky solid (16 % yield). ^{1}H NMR (400 MHz, $CDCl_3$): δ = 8.89 (d, *J* = 3.9 Hz, 2 H), 7.61 (d, *J* = 5.0 Hz, 2 H), 7.25 (at, *J* = 4.5 Hz, 1 H), 4.01 (m, 4 H), 1.92 – 1.78 (m, 2 H), 1.40 – 1.18 (m, 16 H), 0.89 – 0.83 (adt, *J* = 7.3 Hz, 8.8 Hz, 12 H). ^{13}C (100 MHz, $CDCl_3$): δ = 161.8, 140.5, 135.4, 130.6, 130.0, 128.5, 108.0, 45.9, 39.2, 30.3, 28.4, 23.6, 23.2, 14.1, 10.6. HRMS (EI, *m/z*) calc'd for $C_{30}H_{40}N_2O_2S_2$ $[M]^+$: 524.2531; found: 524.2535.

3,6-bis(5-bromothien-2-yl)-2,5-bis(2-ethylhexyl)pyrrolo[3,4-c]pyrrole-1,4(2H,5H)-dione (13). A 100 mL single-neck round-bottom flask was charged with a stir bar, **8** (1.21 g, 2.31 mmol) and chloroform (23 mL) under ambient conditions. After the reaction mixture was stirred in an ice bath at 0 °C for 20 min, NBS (821 mg, 4.61 mmol) was added in small portions over 30 min. After stirring for another 20 min, the reaction mixture was washed with water. The organic extract was dried over $MgSO_4$, and solvent was removed under reduced pressure. Purification by flash chromatography (20 % hexanes in $CHCl_3$) yielded 1.30 g of a purple solid (83 %). ^{1}H NMR (400 MHz, $CDCl_3$): δ = 8.64 (d, *J* = 4.2 Hz, 2 H), 7.22 (d, *J* = 4.2 Hz, 2 H), 3.92 (m, 4 H), 1.88 – 1.78 (m, 2 H), 1.39 – 1.19 (m, 16 H), 0.90 – 0.84 (aq, *J* = 7.3 Hz, 12 H). ^{13}C (100 MHz, $CDCl_3$): δ = 161.5, 139.5, 135.5, 131.6, 131.3, 119.2, 108.1, 46.1, 39.2, 30.3, 28.4, 23.7, 23.2, 14.2, 10.6. HRMS (EI, *m/z*) calc'd for $C_{30}H_{38}Br_2N_2O_2S_2$ $[M]^+$: 682.0721; found: 682.0733.

Scheme 5.5

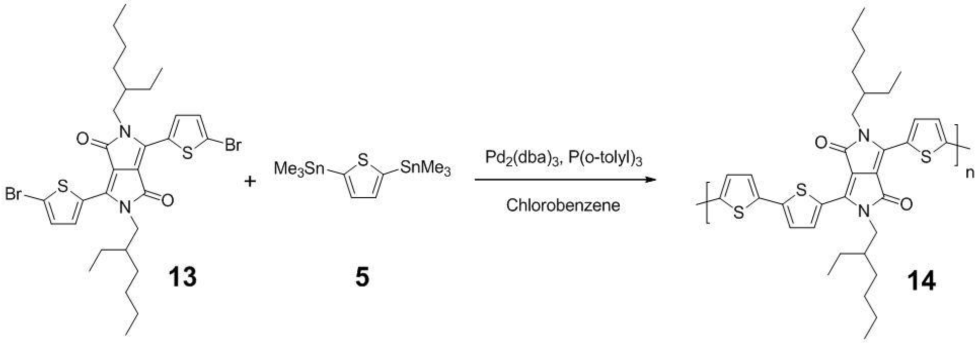

PDPP3T (14): The same polymerization protocol as that described for **PDPP2FT** (**6**) was followed. The substantial solubility limitations encountered with **14** during the purification process (initially attempted as described for **PDPP2FT** (**6**)) led us to establish the following modified protocol for the basic characterization of **14**: on a second polymerization, after 24 h, the reaction was cooled to room temperature and aliquots were taken for SEC and CV analysis (~1 mL was extracted from the reaction mixture and precipitated into ~3 mL of methanol). The crude polymer **14** was collected and dried under nitrogen flow before further use. SEC analysis of the soluble fraction of **14**: M_n = 2 kDa, PDI = 2.71.

Table 5.3. Molecular weight and PDI of P3HT measured by SEC

	M_n (g/mol)	PDI
PDPP2FT	66,000	2.05
PDPP3F	29,000	2.02
PDPP3T	2,000	2.71

5.4.2 Photovoltaic Device Fabrication

All photovoltaic devices have a layered structure with the photoactive layer sandwiched between the two electrodes, ITO and LiF/Al. Glass substrates coated with a 150 nm sputtered ITO pattern of 20 $\Omega\ \square^{-1}$ resistivity were obtained from Thin Film Devices Inc. The ITO-coated glass substrates were ultrasonicated for 20 min each in 2% Hellmanex soap water, DI water, acetone, and then isopropanol. The substrates were dried under a stream of dry nitrogen and then underwent UV-ozone treatment for 5 min. A dispersion of PEDOT:PSS (Baytron PH) in water was filtered (0.45 μm PVDF) and spin coated at 4000 RPM for 60 s, affording a *ca.* 40 nm layer. The substrates were dried for 10 min at 140°C in air and then transferred into a nitrogen glove box for subsequent procedures. PDPP2FT solutions were prepared in chlorobenzene at a concentration of 15 mg/ml and were heated to 100°C and stirred overnight for complete dissolution. PDPP2FT solutions were mixed with 30 mg/ml filtered $PC_{61}BM$ or $PC_{71}BM$ (Nano-C) solutions to yield blend solutions of different concentrations and weight ratios of polymer to PCBM. PDPP3F solutions were prepared in chloroform at a concentration of 10 mg/ml and were heated to 50°C and stirred overnight for complete dissolution. PDPP3F solutions were mixed with 20 mg/ml filtered $PC_{61}BM$ or $PC_{71}BM$ solutions in chloroform to yield blend solutions of different concentrations and weight ratios of polymer to PCBM. Varying amounts of additive CN were added to the blend solutions before spin coating. The active layers of all devices were spin coated at 2000 RPM for 50 s on top of the PEDOT:PSS layer. The substrates were then placed in an evaporation chamber and pumped down to a pressure of ~ 6 x 10^{-7} Torr before evaporating a 1 nm LiF layer and subsequently a 100 nm Al layer through a shadow mask on top of the photoactive layer to yield devices with active areas of 0.03 cm^2. The mechanical removal of part of the organic layer allowed contact with the ITO and adding conductive Ag paste to the removed area to ensure electrical contact completed the device. Testing of the devices was performed under a nitrogen atmosphere with an Oriel Xenon arc lamp having an AM 1.5G solar filter to yield 100 mW cm^{-2} light intensity as calibrated by an NREL certified silicon photocell. Current–voltage behavior was measured with a Keithley 2400 SMU. During the device optimization process, various parameters (solution concentration, blends ratio, spin speed, additive percentage) were tested and more than 200 devices were tested and optimized conditions were repeated to ensure reproducibility. The external quantum efficiency (EQE) was determined at zero bias by illuminating the device with monochromatic light supplied by a Xenon lamp in combination with a monochromator (Spectra Pro 150, Acton Research Corporation). The number of photons incident on the sample was calculated for each wavelength by using a Si photodiode calibrated by the manufacturer (Hamamatsu).

5.4.3 Optical, Electronic, and Morphological Characterization

Cyclic voltammograms were collected using a Solartron 1285 potentiostat under the control of CorrWare II software. A standard three electrode cell based on a Pt wire working electrode, a silver wire pseudo reference electrode (calibrated vs. Fc/Fc^+), and a Pt wire counter electrode was purged with nitrogen and maintained under a nitrogen atmosphere during all measurements. Acetonitrile was purchased anhydrous from Aldrich and tetrabutylammonium hexafluorophosphate (0.1 M) was used as the supporting electrolyte. Polymer films were drop cast onto a Pt wire working electrode from a chloroform, tetrahydrofuran, toluene, or chlorobenzene solution and dried under nitrogen prior to measurement.

UV-Visible absorption spectra were obtained using a Cary 5000 Conc UV-Visible spectrophotometer in transmission geometry. For thin film measurements polymers were spin coated from chlorobenzene or chloroform solutions onto cleaned glass slides. Polymer film thickness was measured by a Veeco Dektak profilometer.

Atomic force microscopy (AFM) was performed to study the surface morphology of the polymer:PCBM blends. Topographical and phase images were obtained concurrently using a Veeco Multimode V AFM in tapping mode using RTESP tips.

5.5 References

(1) Dennler, G.; Scharber, M. C.; Brabec, C. J. *Adv. Mater.* **2009**, *21*, 1323-1338.
(2) Thompson, B. C.; Fréchet, J. M. J. *Angew. Chem., Int. Ed.* **2008**, *47*, 58-77.
(3) Scharber, M. C.; Wuhlbacher, D.; Koppe, M.; Denk, P.; Waldauf, C.; Heeger, A. J.; Brabec, C. L. *Adv. Mater.* **2006**, *18*, 789-794.
(4) Chen, J. W.; Cao, Y. *Acct. Chem. Res.* **2009**, *42*, 1709-1718.
(5) Cheng, Y. J.; Yang, S. H.; Hsu, C. S. *Chem. Rev.* **2009**, *109*, 5868-5923.
(6) Roncali, J. *Macromol.Rapid Comm.* **2007**, *28*, 1761-1775.

(7) Heremans, P.; Cheyns, D.; Rand, B. P. *Acct. Chem. Res.* **2009**, *42*, 1740-1747.

(8) Vandewal, K.; Tvingstedt, K.; Gadisa, A.; Inganas, O.; Manca, J. V. *Nat. Mater.* **2009**, *8*, 904-909.

(9) Veldman, D.; Meskers, S. C. J.; Janssen, R. A. J. *Adv. Funct. Mater.* **2009**, *19*, 1939-1948.

(10) Nguyen, L. H.; Hoppe, H.; Erb, T.; Gunes, S.; Gobsch, G.; Sariciftci, N. S. *Adv. Funct. Mater.* **2007**, *17*, 1071-1078.

(11) Gadisa, A.; Oosterbaan, W. D.; Vandewal, K.; Bolsee, J. C.; Bertho, S.; D'Haen, J.; Lutsen, L.; Vanderzande, D.; Manca, J. V. *Adv. Funct. Mater.* **2009**, *19*, 3300-3306.

(12) Wu, P. T.; Ren, G.; Jenekhe, S. A. *Macromolecules* **2010**, *43*, 3306-3313.

(13) Zoombelt, A. P.; Leenen, M. A. M.; Fonrodona, M.; Nicolas, Y.; Wienk, M. M.; Janssen, R. A. J. *Polymer* **2009**, *50*, 4564-4570.

(14) Huo, L. J.; Hou, J. H.; Chen, H. Y.; Zhang, S. Q.; Jiang, Y.; Chen, T. L.; Yang, Y. *Macromolecules* **2009**, *42*, 6564-6571.

(15) Piliego, C.; Holcombe, T. W.; Douglas, J. D.; Woo, C. H.; Beaujuge, P. M.; Fréchet, J. M. J. *J. Am. Chem. Soc.* **2010**, *132*, 7595-7596.

(16) Chen, M. H.; Hou, J.; Hong, Z.; Yang, G.; Sista, S.; Chen, L. M.; Yang, Y. *Adv. Mater.* **2009**, *21*, 4238-4242.

(17) Hou, J.; Chen, H. Y.; Zhang, S.; Li, G.; Yang, Y. *J. Am. Chem. Soc.* **2008**, *130*, 16144-16145.

(18) Park, S. H.; Roy, A.; Beaupre, S.; Cho, S.; Coates, N.; Moon, J. S.; Moses, D.; Leclerc, M.; Lee, K.; Heeger, A. J. *Nat. Photon.* **2009**, *3*, 297-302.

(19) Peet, J.; Kim, J. Y.; Coates, N. E.; Ma, W. L.; Moses, D.; Heeger, A. J.; Bazan, G. C. *Nat. Mater.* **2007**, *6*, 497-500.

(20) Liang, Y.; Feng, D.; Wu, Y.; Tsai, S. T.; Li, G.; Ray, C.; Yu, L. *J. Am. Chem. Soc.* **2009**, *131*, 7792-7799.

(21) Qin, R. P.; Li, W. W.; Li, C. H.; Du, C.; Veit, C.; Schleiermacher, H. F.; Andersson, M.; Bo, Z. S.; Liu, Z. P.; Inganas, O.; Wuerfel, U.; Zhang, F. L. *J. Am. Chem. Soc.* **2009**, *131*, 14612-14613.

(22) Zou, Y. P.; Najari, A.; Berrouard, P.; Beaupre, S.; Reda Aich, B.; Tao, Y.; Leclerc, M. *J. Am. Chem. Soc.* **2010**, *132*, 5330-5331.

(23) Huo, L. J.; Hou, J. H.; Zhang, S. Q.; Chen, H. Y.; Yang, Y. *Angew. Chem., Int. Ed.* **2010**, *49*, 1500-1503.

(24) Bunz, U. H. F. *Angew. Chem., Int. Ed.* **2010**, *49*, 5037-5040.

(25) Umeyama, T.; Takamatsu, T.; Tezuka, N.; Matano, Y.; Araki, Y.; Wada, T.; Yoshikawa, O.; Sagawa, T.; Yoshikawa, S.; Imahori, H. *J. Phys. Chem. C* **2009**, *113*, 10798-10806.

(26) Yamamoto, T.; Zhou, Z. H.; Kanbara, T.; Shimura, M.; Kizu, K.; Maruyama, T.; Nakamura, Y.; Fukuda, T.; Lee, B. L.; Ooba, N.; Tomaru, S.; Kurihara, T.; Kaino, T.; Kubota, K.; Sasaki, S. *J. Am. Chem. Soc.* **1996**, *118*, 10389-10399.

(27) Li, R. Z.; Lv, X. J.; Shi, D.; Zhou, D. F.; Cheng, Y. M.; Zhang, G. L.; Wang, P. *J. Phys. Chem. C* **2009**, *113*, 7469-7479.

(28) Lin, J. T.; Chen, P. C.; Yen, Y. S.; Hsu, Y. C.; Chou, H. H.; Yeh, M. C. P. *Org.Lett.* **2009**, *11*, 97-100.

(29) Walker, B.; Tomayo, A. B.; Dang, X. D.; Zalar, P.; Seo, J. H.; Garcia, A.; Tantiwiwat, M.; Nguyen, T. Q. *Adv. Funct. Mater.* **2009**, *19*, 3063-3069.

(30) Chen, Z. F.; Wannere, C. S.; Corminboeuf, C.; Puchta, R.; Schleyer, P. V. *Chem. Rev.* **2005**, *105*, 3842-3888.

(31) Zou, Y. P.; Gendron, D.; Neagu-Plesu, R.; Leclerc, M. *Macromolecules* **2009**, *42*, 6361-6365.

(32) Zou, Y. P.; Gendron, D.; Reda Aich, B.; Najari, A.; Tao, Y.; Leclerc, M. *Macromolecules* **2009**, *42*, 2891-2894.

(33) Zou, Y.; Najari, A.; Berrouard, P.; Beaupre, S.; Reda Aich, B.; Tao, Y.; Leclerc, M. *J. Am. Chem. Soc.* **2010**, *132*, 5330-5331.

(34) Bijleveld, J. C.; Zoombelt, A. P.; Mathijssen, S. G. J.; Wienk, M. M.; Turbiez, M.; de Leeuw, D. M.; Janssen, R. A. J. *J. Am. Chem. Soc.* **2009**, *131*, 16616-16617.

(35) Gidron, O.; Diskin-Posner, Y.; Bendikov, M. *J. Am. Chem. Soc.* **2010**, *132*, 2148-2149.

(36) Miyata, Y.; Nishinaga, T.; Komatsu, K. *J. Org. Chem.* **2005**, *70*, 1147-1153.

(37) Hucke, A.; Cava, M. P. *J. Org. Chem.* **1998**, *63*, 7413-7417.

(38) Scully, S. R.; McGehee, M. D. *J. Appl. Phys.* **2006**, *100*, 034907.

(39) Shaw, P. E.; Ruseckas, A.; Samuel, I. D. W. *Adv. Mater.* **2008**, *20*, 3516-3520.

(40) Markov, D. E.; Amsterdam, E.; Blom, P. W. M.; Sieval, A. B.; Hummelen, J. C. *J. Phys. Chem. A* **2005**, *109*, 5266-5274.

Chapter 6

Solution Processing of a Small Molecule Subnaphthalocyanine for Efficient OPVs[4]

Abstract

Solution processing of the small molecule subnaphthalocyanine (SubNc) is carried out to form an electron-donor layer in efficient planar heterojunction OPV devices. Due to their unique properties, including high solubility, low tendency to aggregate, and strong light absorption in the visible light region, we are able to prepare amorphous SubNc films with high charge-transporting and light-harvesting properties via simple solution casting. By using SubNc as the donor and C_{60} as the acceptor, we have demonstrated a planar heterojunction OPV with a power conversion efficiency of 1.5%, which represents one of the highest efficiencies for planar heterojunction OPVs based on solution processable small molecules to date. This work demonstrates that solution processing of light-harvesting small molecules has great potential in low-cost thin-film photovoltaic cells. Importantly, SubNc and its derivatives are promising new-generation materials for OPVs.

---

[4] Reproduced in part with permission from Ma, B.; Woo, C. H.; Miyamoto, Y. , J. M. J. *Chemistry of Materials,* **2009**, *21*, 1413-1417. Copyright 2009 American Chemical Society.

6.1 Introduction

The state-of-the-art efficiency of OPVs has steadily improved over the last decade from about 1% to over 5%, with considerable efforts directed towards the development of new materials and device structures.[1-8] In previous chapters, we have focused much attention on polymer-based organic photovoltaics. Small molecules are an alternative material family that has also received considerable interest. In the area of device fabrication, there are two primary thin film preparation methods: one is solution processing, and the other involves high vacuum vapor deposition of thermally stable molecules. Solution processing is generally believed to be more cost efficient than vapor deposition, as it does not involve expensive high vacuum systems and is feasible for large scale roll-to-roll production. Unfortunately, the use of solution processing in OPVs has so far been limited to soluble conjugated polymers because of their favorable film formation properties during spin coating.[9,10] Uniform surface morphology is desirable for better charge transport and charge extraction in a solar cell.

On the other hand, there has been little success in the solution processing of small molecules for OPVs despite their advantages over polymeric semiconductors, which include monodispersity, high charge carrier mobility, and relatively simple synthesis.[11] To our best knowledge, the state-of-the-art efficiency in solution processed small molecule OPVs has reached only modest values of *ca.* 1 % so far.[11] Factors such as limited solubility and tendency to aggregate in most organic solvents are responsible for the difficulty in solution processing of small molecules. For example, Copper phthalocyanine (CuPc), a commonly used small molecule donor material, is poorly soluble in most organic solvents, thus thin films can only be prepared by vapor deposition.[1] In addition, crystallization of solution-cast small molecules on a substrate often results in poor film formation with polycrystalline domains, which are characterized by unfavorable grain connectivity and sub-optimal crystalline ordering.[11]

In this Chapter, we demonstrate efficient solar cells based on a solution processed electron donor material, the small molecule subnaphthalocyanine (SubNc). Similar to its related analogue subphthalocyanine (SubPc), SubNc has a nonplanar pyramid-shaped structure, in which a boron is surrounded by three coupled benzo-isoindole units to give a 14-π-electron aromatic macrocycle.[12-14] The unique cone-shaped geometry of SubPc and SubNc, contrasts with the flat or nearly flat structure of most phthalocyanines and provides them with distinctive physical properties, such as high solubility and low tendency of aggregation. In addition, their outstanding electronic and optical properties make them of interest for a variety of applications, such as non-linear optics and photodynamic therapy.[14-17] The strong absorption in the visible light region with extinction coefficients of *ca.* 5×10^4 $M^{-1}cm^{-1}$ enables them to be used as effective light harvesting materials in solar energy conversion applications.[14] Indeed, the concept of artificial photosynthetic systems with SubPcs as light harvesting donor units has been demonstrated in SubPc-C_{60} dyads.[18,19] More recently, two research groups have reported efficient organic photovoltaic cells with power conversion efficiencies over 2% by using vacuum deposited SubPc films as the electron donor and fullerene (C_{60}) as the electron acceptor.[20,21] In this study, we investigate for the first time the use of solution processable SubNc in OPV devices. The addition of a ring system to the isoindole units increases the solubility of the SubNc while reducing their tendency to aggregate and broadening their absorption as compared to SubPc.[13] These factors enable the solution processing of high quality SubNc thin films for OPVs.

6.2 Results and Discussion

The usefulness of solution deposited SubNc films in organic photovoltaic cells was evaluated in planar heterojunction devices. Figure 6.1 shows the chemical structures of the materials, the device structure and a schematic energy level diagram. The energy levels of each layer have been reported in the literature.[10,20-23] The device fabrication process involves spin coating chlorobenzene solutions of the donor materials on top of ITO glass substrates pre-coated with PEDOT:PSS, followed by vapor deposition of a 325 Å thick film of C_{60} as acceptor, a 100 Å thick film of 2,9-dimethyl-4,7- diphenyl-l,10-phenanthroline (BCP) used as an exciton blocking layer, and a 1000 Å thick silver cathode. The detailed device structure and thickness are ITO/PEDOT:PSS/Donor Layer/C_{60} (325 Å)/BCP(100 Å)/Ag(1000 Å) as shown in Figure 1b. The thickness of the SubNc donor layer was controlled by the concentration of the solution used for spin coating and was varied from 75 Å (SubNc1) to 320 Å (SubNc5). For valid comparisons, the thicknesses of the C_{60} and BCP layers were fixed to values comparable to those reported elsewhere.[20,21] The control device consisted of a 400 Å thick film of *P3HT*, the most common solution processable polymer donor material.

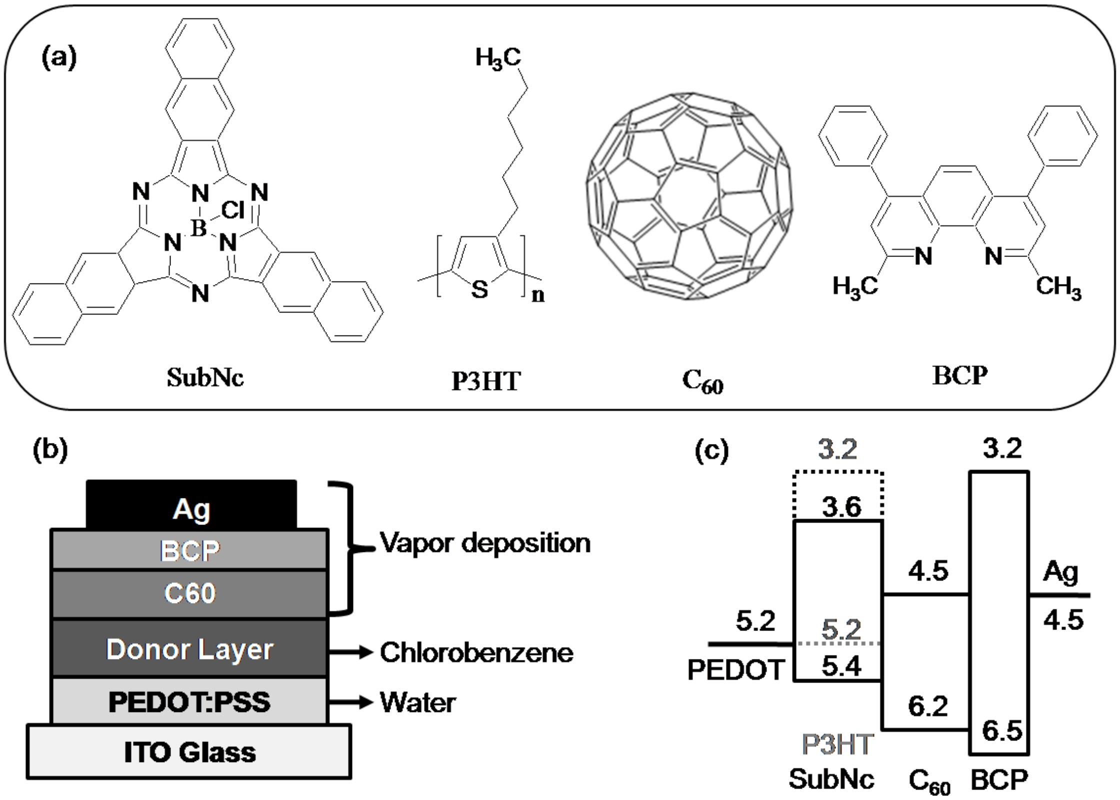

Figure 6.1. (a) Structures of the materials used in this study, (b) device architecture and processing methods, and (c) schematic device energy level (HOMO and LUMO) diagram.

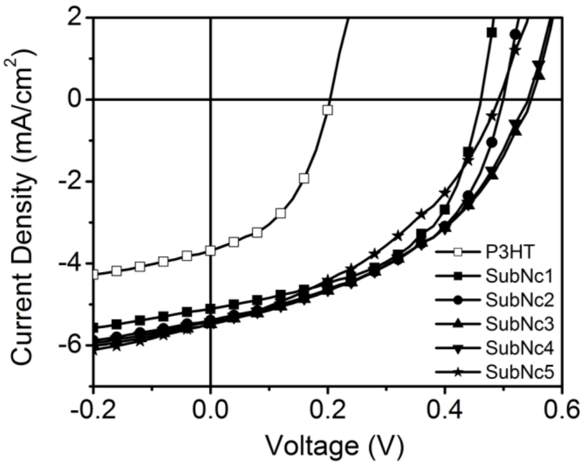

Figure 6.2. Current density *vs.* voltage (*J-V*) characteristics of organic photovoltaic cells with the structure ITO/PEDOT/Donor Layer/C_{60} (325 Å)/BCP(100 Å)/Ag(1000 Å) under 1 sun AM 1.5 G simulated illumination.

Table 6.1. Average device parameters of SubPc/C_{60} and P3HT/C_{60} planar heterojunction solar cells

Device	Donor (Å)	J_{sc} (mA cm^{-2})	V_{oc} (V)	FF	PCE (%)
P3HT[a]	400	3.57 (3.71)	0.20 (0.25)	0.45 (0.50)	0.33 (0.47)
SubNc1	75	5.03	0.46	0.51	1.19
SubNc2	110	5.39	0.50	0.47	1.25
SubNc3[a]	200	5.39 (5.59)	0.55 (0.55)	0.42 (0.49)	1.25 (1.47)
SubNc4	285	5.30	0.55	0.43	1.23
SubNc5	320	5.30	0.49	0.40	1.04

[a] Devices were measured before and after annealing at120°C for 40 min; data in brackets are for annealed devices.

Figure 6.2 shows the device performance for the SubNc devices and P3HT control device under 100 mW cm^{-2} AM 1.5G solar illumination, and Table 6.1 summarizes the performance parameter for the devices. All the SubNc devices show better performance than the P3HT control device, with higher open-circuit voltages (V_{oc}) of ~ 0.5 V, higher short-circuit current density (J_{sc}) of ~ 5.4 mA cm^{-2} and comparable fill factor (FF) of ~ 0.45. The higher V_{oc} and J_{sc} lead to power conversion efficiencies (η_p) of about 1.25 % for the SubNc devices *vs.* 0.3 % for the P3HT device. The V_{oc} is usually limited by the energy difference between the lowest unoccupied molecular orbital (LUMO) of the electron acceptor and the highest occupied molecular orbital (HOMO) of the electron donor in planar heterojunction cells.[20] Therefore, in this case, the increased V_{oc} is attributed to the higher HOMO-LUMO gap for SubNc/C_{60} compared to P3HT/C_{60}, as illustrated in Figure 6.1c. For the same reason, the V_{oc} of our SubNc/C_{60} device is lower than that of previously reported SubPc/C_{60} device with V_{oc} approaching to 1.0 V,[20,21] as a result of the higher HOMO of SubNc *vs.* SubPc, which is caused by the increased conjugation with the addition of benzo rings on SubNc.[13]

In these planar heterojunction devices, the short-circuit current density (J_{sc}) is determined primarily by the absorption of the active materials, the exciton diffusion length and the charge transport properties. From absorption and thickness measurements, we calculated that SubNc films have an absorption coefficient of 5×10^4 cm^{-1}, which is similar to that of P3HT. Thus, the spectral overlap of the absorption of the two materials (SubNc and C_{60}) with the solar spectrum may play a larger role in determining the photocurrent of the devices. As shown in Figure 6.3, SubNc has a much broader absorption than P3HT, peaking at $\lambda_{max} = 688$ nm *vs.* 556 nm for P3HT, leading to a better overlap with the solar spectrum, which has a maximum photon flux around 670 nm.[24] This is confirmed by comparing the external quantum efficiencies (EQEs) for the SubNc device and the P3HT device. As shown in Figure 6.4, the SubNc2 device has strong photo-response generated in the region from 650 nm to 730 nm with EQEs over 10%. The photocurrent at short wavelengths (400 nm - 500 nm) is mainly contributed by C_{60}. Also, due to the extended conjugation and absorption of SubNc, the SubNc/C_{60} device has a much higher current density (~ 5.4 $mAcm^{-2}$) than the SubPc/ C_{60} cell (~ 3.4 $mAcm^{-2}$).[20]

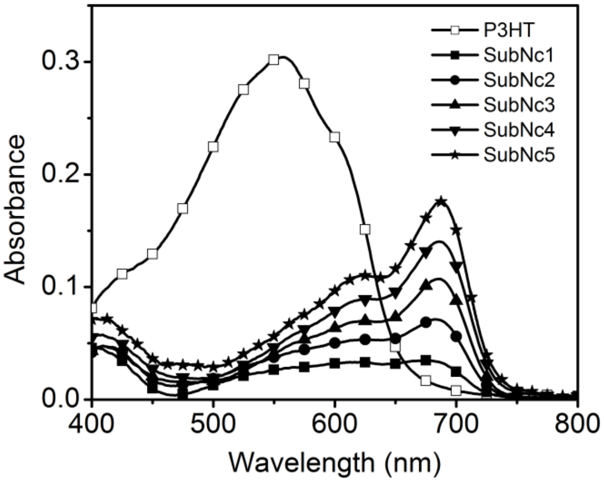

Figure 6.3. Absorption spectra for the films of P3HT (400 Å) and SubNc (75 Å-320 Å).

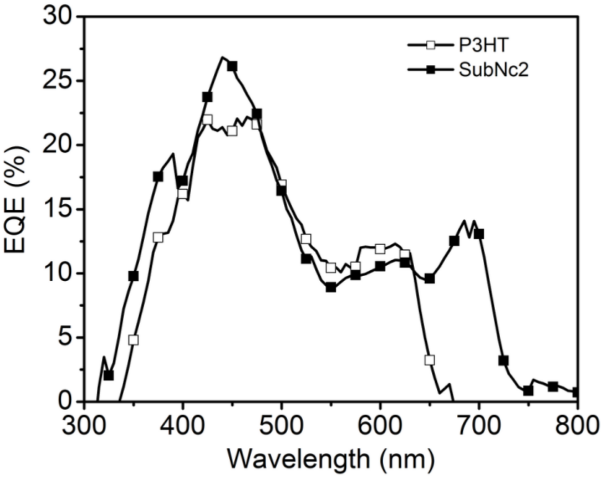

Figure 6.4. External quantum efficiencies for the P3HT control device and SubNc2 device

Unlike many vapor deposited metal phthalocyanine (MPc)/C_{60} devices that display a strong performance dependence on the thickness of the MPc layer,[20,25] our devices with solution processed SubNc film displayed a near thickness-independent behavior up to 300 Å (see Figure 6.2). This result suggests that the solution processed SubNc film has a relatively high charge carrier mobility and/or a longer exciton diffusion length (L_{ex}) than vapor deposited MPc films.[20,25] To investigated this further, the hole mobility of SubNc was measured in the device structure of ITO/PEDOT:PSS/SubNc(360 Å)/Au based on the field independent space-charge-limited mobility model. Gold electrode was used to ensure a hole-only device. The measurement was conducted on devices before and after thermal annealing at 120°C for 40 min, and no significant change in the *I-V* characteristics was observed. Assuming a relative dielectric constant of 3.9 for SubNc,[21] the analysis gives a hole mobility of $\sim 2\times10^{-5}$ cm^2 V^{-1} s^{-1}, which is much higher than that of many other MPc films, such as SnPc that has a hole mobility of 2×10^{-10} cm^2 V^{-1} s^{-1}.[25] In addition, the hole mobility value that we measured is close to the theoretical optimum charge carrier mobility for organic solar cells for minimizing recombination losses as well as ensuring efficient charge extraction.[26]

The relatively high mobility of solution processed small molecule thin film is not surprising when considering the molecular packing and film surface morphology of SubNc. First, the additional aromatic rings increase the extent of conjugation and better overlap between the isoindole units, leading to better charge hopping between molecules in the SubNc film than in the SubPc film.[18] Second, SubNc forms a smooth and continuous film upon solution casting on a substrate, which is beneficial for charge migration without trap sites or shunt currents caused by defects. AFM was used to characterize the topology of SubNc thin film on top of PEDOT:PSS pre-coated ITO substrate. Figure 6.5 shows the AFM images of films before and after thermal annealing. It was found that a featureless continuous film was obtained after spin coating a chlorobenzene solution of SubNc on the substrate. The surface has a root-mean-square (rms) roughness of 16 Å, which is lower than that of vapor deposited SubPc thin film on ITO substrates,[21] confirming that high quality thin films are achievable through solution processing. Thermal annealing at 120°C for 40 minutes further reduced the rms roughness to a value of 7 Å. The formation of smooth SubNc films without aggregation can be predicted by comparing the absorption spectra of SubNc in thin films with different thickness and in solution.[13,17] As shown in Figure 6.3, the thin film spectra is almost identical to that in solution with little peak shift or change in shape upon changing the thickness, suggesting that molecular aggregation is not prevalent in the spin coated SubNc films.

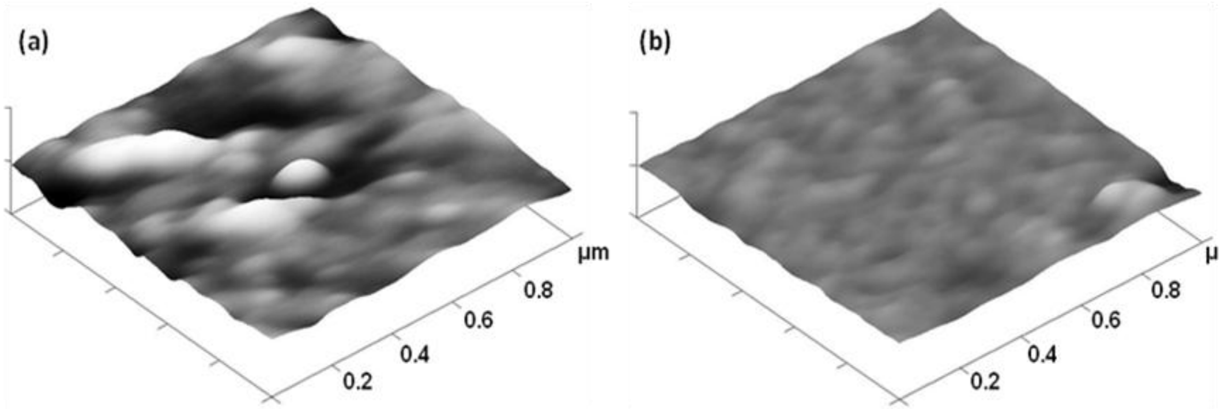

Figure 6.5. AFM height images of 200 Å thick film of SubNc on top of PEDOT:PSS pre-coated ITO substrates (vertical axis is on a scale of 20 nm/division, horizontal axes are 0.2 μm/division): (a) before annealing with rms roughness of 16 Å, (b) after thermal annealing at 120 °C for 40minutes with rms roughness of 7 Å.

For many organic semiconductor materials, exciton diffusion length is primarily determined by the combination of carrier mobility and exciton lifetime. The value of the product (mobility × lifetime) for high-performance photovoltaic materials with L_{ex} > 100 Å is usually of the order of 10^{-10} or 10^{-9} cm^2 V^{-1}.[22,27] Given that the hole mobility of SubNc is in the order of 10^{-5} cm^2 V^{-1} s^{-1}, the exciton lifetime for SubNc would be expected to be of the order of microseconds. Since SubNc possesses a singlet lifetime of about 3 ns and a triplet lifetime of about 90 μs in solution,[14,17] it is likely that the triplet states of SubNc participate in the charge separation process.[28] Such involvement of triplet excitons in SubNc would be expected given its efficient intersystem crossing ($k_{\mathrm{isc}} \sim 3\times10^8$ s^{-1}) and high triplet quantum yield ($\Phi_{\mathrm{T}} \sim 0.7$).[14,17] Based on these considerations, we believe that SubNc in OPVs behaves very similarly to the typical triplet material PtOEP, which has an almost identical hole mobility of about 10^{-5} cm^2 V^{-1} s^{-1}, a triplet lifetime of 91 μs in a doped thin film, and an exciton diffusion length of around 300 Å.[22] The fundamental study of triplet excitons behavior in OPVs based on SubNc and its related materials is in process.

We further investigated the effect of thermal annealing on device performance. Thermal treatment has been shown to improve device performance by reducing the series resistance in many OPV devices.[5,22] In our study, the finished devices were treated at 120°C in an argon filled glove box for 40 minutes. Figure 6.6 shows the device performance for the SubNc3 cell and the P3HT control cell before and after thermal treatment. It is found that thermal annealing significantly improved the P3HT device efficiency from 0.34 % to 0.48 %, with a concomitant increase in all the important device characteristics (V_{oc}, J_{sc} and FF). This improvement can be ascribed to the enhanced charge carrier mobility of P3HT thin film caused by thermally induced crystallization.[29] Although not as pronounced as in the P3HT control device, an improvement in performance is also observed in the SubNc device upon thermal annealing treatment. The increase in PCE value from 1.28 % to 1.49 % upon annealing is mainly due to the increase in fill factor (FF) from 0.43 to 0.49. Since there was almost no change in film morphology or carrier mobility for the SubNc layer upon thermal annealing as described above, the slight improvement is most probably caused by the increase of donor/acceptor interfacial area as a result of the inter-diffusion of SubNc and C_{60} layers during thermal annealing.

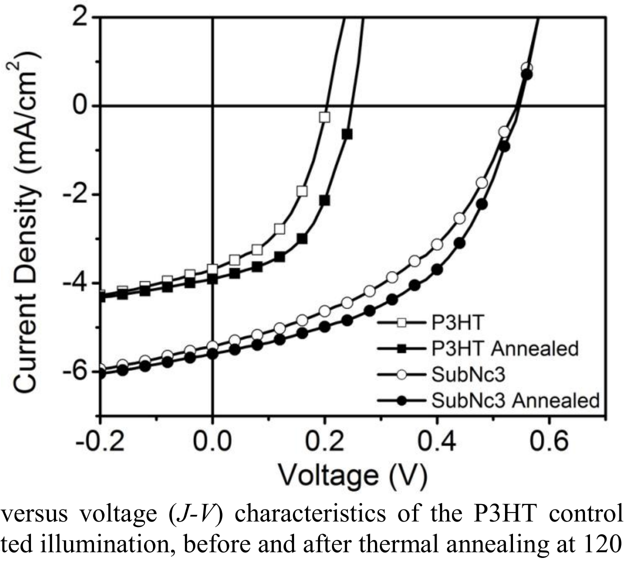

Figure 6.6. Current density versus voltage (*J-V*) characteristics of the P3HT control device and SubNc3 device under 1 sun AM 1.5 G simulated illumination, before and after thermal annealing at 120 °C for 40 minutes.

6.3 Conclusions

In this Chapter, we have demonstrated efficient OPV devices based on solution processable small molecule Subphthalocyanine (SubNc). The unique structural and photophysical properties of SubNc, including its high solubility, low tendency to aggregate, and strong light absorption, enable the solution processing of thin films with favorable light absorbing and charge transporting properties. By using SubNc as the donor and C_{60} as the acceptor, power conversion efficiency of 1.5 % was achieved in a simple planar heterojunction structure with open circuit voltage of 0.55 V, short circuit current density of 5.6 mA cm^{-2}, and fill factor of 0.49, which represents one of the highest performing devices reported to date based on solution processable small molecules. The participation of triplet excitons of SubNc is likely a contributing factor to the high device performance. The use of solution processed small molecules is promising in the search for low-cost and efficient devices and that SubNc and its derivatives are promising as new-generation materials for OPVs.

6.4 Experimental

Patterned Indium tin oxide (ITO) coated glass substrates were purchased from Thin Film Devices Inc. Poly(3,4-ethylenedioxythiophene) poly(styrenesulfonate) (PEDOT:PSS) (Baytron-PH500) was purchased from H. C. Starck. Poly(3-hexylthiophene)(*P3HT*) used was house-made with a number average molecular weight (M_n) of 35 kDa. Subnaphthalocyanine(SubNc), 2,9-Dimethyl-4,7-diphenyl-1,10-phenanthroline(BCP) (96 %), C60 (99.9 %, sublimed), silver shot(1-3 mm, 99.99+ %) and chlorobenzene (anhydrous, 99.8 %) were purchased from Aldrich. BCP was purified in a home-built thermal gradient sublimator before its use for vapor evaporation.

ITO glass substrates were cleaned using the following sequential steps: sonication in soap solution; rinsing with deionized water; boiling in trichloroethylene, acetone, and ethanol for 5 min each; and drying with nitrogen. Finally, the substrates were treated with UV ozone for 10 min. A filtered dispersion of PEDOT:PSS in water (Baytron-PH500) was spun cast at 4000 rpm for 40 s to produce a 32 nm thick layer, followed by baking at 140 ºC for 10 min in ambient. Solution processing of the films was performed in an inert-atmosphere (Argon) glove box. One solution of SubNc (10 mg/ml in chlorobenzene) and one solution of P3HT (10 mg/ml in chlorobenzene) were prepared and stirred at 110 ºC overnight to ensure complete dissolution. Prior to use in the fabrication of devices the solutions were passed through a 0.45 μm polytetrafluoroethylene syringe filter. Diluting a 10 mg/ml solution of SubNc with pure chlorobenzene afforded the more dilute solutions (from 2 mg/ml to 8 mg/ml) used to prepare SubNc films of different thicknesses. Thin films of SubNc and P3HT were prepared by spin casting their solutions on the PEDOT pre-coated ITO substrates at 2000 rpm for 40 s. After solution processing, high vacuum thermal vapor evaporation was applied to deposit the C_{60}, BCP and Ag cathode. The deposition rates for C_{60}, BCP, and Ag were controlled at 1.5 $Ås^{-1}$, 1.5 $Ås^{-1}$, and 5$Ås^{-1}$ respectively. The Ag cathode was evaporated through a shadow mask to produce an active area of 0.03 cm^2. After evaporation, a part of the organic layer was removed to allow contact with the ITO, and then conductive silver paste was painted to the area in order to produce the electrical contact. Thermal annealing was performed on a temperature-controlled hotplate at 120 ºC in the glove box.

All devices properties were measured at room temperature in an Argon atmosphere under AM 1.5 G solar illumination at 100 mWcm^{-2} (1 sun) using a Thermal-Oriel 300W solar simulator with filter. External quantum efficiency (EQE) values were obtained with a monochromator and calibrated with a silicon photodiode. The Current density-voltage (*J*-*V*) characteristics were recorded in a Keithly 236 SMU. Absorption spectra were recorded in a Cary 50 UV-vis spectrometer. Film thickness measurements were performed using a Dektak 150 surface profiler. Topographical images were obtained using a Veeco Multimode V Atomic Force Microscope (AFM).

6.5 References

(1) Tang, C. W. *Applied Physics Letters* **1986**, *48*, 183-185.
(2) Yu, G.; Gao, J.; Hummelen, J. C.; Wudl, F.; Heeger, A. J. *Science* **1995**, *270*, 1789-1791.
(3) Xue, J. G.; Uchida, S.; Rand, B. P.; Forrest, S. R. *Applied Physics Letters* **2004**, *85*, 5757-5759.
(4) Kim, J. Y.; Lee, K.; Coates, N. E.; Moses, D.; Nguyen, T. Q.; Dante, M.; Heeger, A. J. *Science* **2007**, *317*, 222-225.
(5) Peumans, P.; Uchida, S.; Forrest, S. R. *Nature* **2003**, *425*, 158-162.
(6) Rand, B. P.; Genoe, J.; Heremans, P.; Poortmans, J. *Progress in Photovoltaics* **2007**, *15*, 659-676.
(7) Kroon, R.; Lenes, M.; Hummelen, J. C.; Blom, P. W. M.; De Boer, B. *Polymer Reviews* **2008**, *48*, 531-582.
(8) Bundgaard, E.; Krebs, F. C. *Solar Energy Materials and Solar Cells* **2007**, *91*, 954-985.
(9) Gunes, S.; Neugebauer, H.; Sariciftci, N. S. *Chemical Reviews* **2007**, *107*, 1324-1338.
(10) Thompson, B. C.; Fréchet, J. M. J. *Angewandte Chemie-International Edition* **2008**, *47*, 58-77.
(11) Lloyd, M. T.; Anthony, J. E.; Malliaras, G. G. *Materials Today* **2007**, *10*, 34-41.
(12) Kobayashi, N.; Ishizaki, T.; Ishii, K.; Konami, H. *Journal of the American Chemical Society* **1999**, *121*, 9096-9110.
(13) Martin, G.; Rojo, G.; Agullo-Lopez, F.; Ferro, V. R.; de la Vega, J. M. G.; Martinez-Diaz, M. V.; Torres, T.; Ledoux, I.; Zyss, J. *Journal of Physical Chemistry B* **2002**, *106*, 13139-13145.
(14) Claessens, C. G.; Gonzalez-Rodriguez, D.; Torres, T. *Chemical Reviews* **2002**, *102*, 835-853.
(15) Sastre, A.; Torres, T.; DiazGarcia, M. A.; AgulloLopez, F.; Dhenaut, C.; Brasselet, S.; Ledoux, I.; Zyss, J. *Journal of the American Chemical Society* **1996**, *118*, 2746-2747.
(16) del Rey, B.; Keller, U.; Torres, T.; Rojo, G.; Agullo-Lopez, F.; Nonell, S.; Marti, C.; Brasselet, S.; Ledoux, I.; Zyss, J. *Journal of the American Chemical Society* **1998**, *120*, 12808-12817.
(17) Nonell, S.; Rubio, N.; del Rey, B.; Torres, T. *Journal of the Chemical Society-Perkin Transactions 2* **2000**, *6*, 1091-1094.
(18) Rodriguez, D.; Torres, T.; Guldi, D. M.; Rivera, J.; Herranz, M. A.; Echegoyen, L. *Journal of the American Chemical Society* **2004**, *126*, 6301-6313.
(19) Gonzalez-Rodriguez, D.; Torres, T.; Herranz, M. A.; Echegoyen, L.; Carbonell, E.; Guldi, D. M. *Chemistry-A European Journal* **2008**, *14*, 7670-7679.

(20) Mutolo, K. L.; Mayo, E. I.; Rand, B. P.; Forrest, S. R.; Thompson, M. E. *Journal of the American Chemical Society* **2006**, *128*, 8108-8109.

(21) Gommans, H.; Cheyns, D.; Aernouts, T.; Girotto, C.; Poortmans, J.; Heremans, P. *Advanced Functional Materials* **2007**, *17*, 2653-2658.

(22) Shao, Y.; Yang, Y. *Advanced Materials* **2005**, *17*, 2841.

(23) Adamovich, V. I.; Cordero, S. R.; Djurovich, P. I.; Tamayo, A.; Thompson, M. E.; D'Andrade, B. W.; Forrest, S. R. *Organic Electronics* **2003**, *4*, 77-87.

(24) Muhlbacher, D.; Scharber, M.; Morana, M.; Zhu, Z. G.; Waller, D.; Gaudiana, R.; Brabec, C. *Advanced Materials* **2006**, *18*, 2884.

(25) Rand, B. P.; Xue, J. G.; Yang, F.; Forrest, S. R. *Applied Physics Letters* **2005**, *87*.

(26) Mandoc, M. M.; Koster, L. J. A.; Blom, P. W. M. *Applied Physics Letters* **2007**, *90*.

(27) Terao, Y.; Sasabe, H.; Adachi, C. *Applied Physics Letters* **2007**, *90*.

(28) Wrobel, D.; Boguta, A.; Mazurkiewicz, P. *Spectrochimica Acta Part A-Molecular and Biomolecular Spectroscopy* **2003**, *59*, 2841-2854.

(29) Cho, S.; Lee, K.; Yuen, J.; Wang, G. M.; Moses, D.; Heeger, A. J.; Surin, M.; Lazzaroni, R. *Journal of Applied Physics* **2006**, *100*.

Chapter 7

Correlating Mobility and Crystallinity for Photocrosslinkable Bromine-Functionalized Poly(3-hexylthiophene)

7.1 Introduction

With the performance and reliability of solution-processed organic electronics rapidly advancing, organic field-effect transistors (OFETs) are fast becoming a reality in emerging commercial applications such as printable electronics and flexible optical displays.[1,2] In the past decade, research efforts have focused on developing new organic semiconductors for better charge carrier mobility. For the design of materials for OFETs, a critical parameter is the microstructural order of the semiconductor.[3,4] Among the best polymeric semiconductors reported to date, such as PBTTT[5,6], PDBT-co-TT[7] and P3HT[8] for p-channel and N2200[9,10] for n-channel FETs, their high performance has been attributed to the ability of the polymer chains to π-stack regularly in a thin film. Similarly, the best small molecule semiconductors for OFETS have a high propensity to organize into regular crystal structures.[11,12] While it is important to develop materials that inherently possess a high tendency to self-organize (for example, by having a rigid backbone or by choosing the right side chain), an additional challenge is the dependence of charge transport properties on processing conditions. For instance, the charge carrier mobility of a solution-processed polymer-based transistor can vary by orders of magnitude by applying different processing techniques such as post-deposition treatments, solvent choice, or substrate engineering. However, there are gaps in our understanding of how processing conditions affect the microstructure of a polymer thin film and ultimately its electronic performance. One of the previous limitations in advancing our knowledge in this field had been the lack of appropriate and sensitive characterization methods for probing thin film microstructure. However, with recent advances in molecular and x-ray characterization techniques,[13-15] it is now possible to draw clear correlations between the microstructural order and charge transport properties of a polymer thin film.

While thermal annealing is commonly performed to enhance polymer crystallinity, there are other processing conditions that may be of interest. For example, crosslinking is a useful technique that allows the fabrication of complex multilayer devices.[16-18] Bilayer FETs are also desirable for achieving ambipolar transport useful for simplifying the electronic circuit design.[19,20] However, the effect of crosslinking on the microstructural order of a conjugated polymer has not been well studied (REF?). Recently, our group has developed a photo-crosslinkable derivative of the semiconducting polymer P3HT.[21] Using bromine as the crosslinkable moiety tethered to the end of the alkyl side chain of the polymer, bromine functionalized conjugated polymers can be easily crosslinked by UV irradiation.[21,22] Here, we use the photocrosslinkable P3HT-Br10 as a model system to illustrate the effect of crosslinking and thermal annealing on FET performance and correlate charge mobility with thin film crystallinity. We chose the P3HT-Br10 derivative, which contains 10% of the bromine functionalized monomer unit in its backbone, to ensure sufficient bromine content for complete crosslinking while minimizing the disruption of the semicrystalline nature of the P3HT polymer.[21] This study highlights the use of crosslinking to tune the microstructural order of the polymer thin film. In addition, we have developed a process for achieving both a high degree of crystallinity (DOC) and high mobility.

7.2 Results and Discussion

The P3HT-Br10 polymer (Figure 7.7) was synthesized by the same procedure as reported.[21] The polymer used in this study had a M_n of 19,000 g/mol and a PDI of 1.2. OFETs were fabricated in a bottom-gate, bottom-contact configuration with highly doped p-type (100) silicon wafers as the gate electrode and 300 nm of SiO_2 as the gate dielectric. Patterned Au electrodes were deposited onto the substrate by lithography. The polymer layer was spun cast from chloroform on octadecyltrichlorosilane (OTS) treated Si/SiO_2 substrates. Devices were fabricated with typical channel lengths of 20 μm and channel width of 800 μm. I-V plots of device performance were measured under vacuum, and transfer and output plots were recorded for each device. For each condition, the reported data are averaged over 3-5 devices to ensure reproducibility and consistency. Key device performance parameters, including field-effect mobility (μ), threshold voltage (V_{TH}), and on/off current ratio (I_{ON}/I_{OFF}) were extracted under standard procedures. The results are summarized in Table 7.1. Figure 7.8 shows two examples of the characteristic output and transfer plots of devices under two of the processing conditions we examined. The rest of the I-V plots are shown in the supporting information.

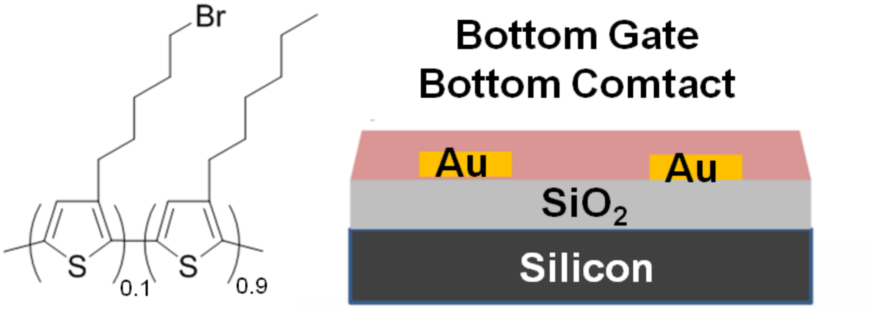

Figure 7.7 The structure of P3HT-Br10 and the BG-BC FET configuration used.

Table 7.1 Summary of OFET performance of Br-P3HT films processed under different conditions

Processing condition	μ **(cm^2 V^{-1} s^{-1})**	I_{ON}/I_{OFF}	V_{TH} **(V)**
As cast	1.2×10^{-3}	10^2	47
Annealed (1 hr)	2.7×10^{-2}	10^3	-10
Crosslinked (1 hr)	Not active?	Not active?	Not active?
Crosslinked (1 hr) and then annealed (1 hr)	2.5×10^{-4}	7×10^3	-5
Crosslinked and annealed simultaneously (1 hr)	8.5×10^{-3}	10^3	-10

First of all, it is clear that the OFET performance is highly dependent on processing conditions. Under five different processing conditions with various combinations of crosslinking and annealing sequence, the mobility of P3HT-Br10 FET devices varied over two orders of magnitude. For as cast P3HT-Br10 films (see Figure 7.8a and b for I-V plots), the p-channel FET mobility was measured to be 1.2×10^{-3} cm^2 V^{-1} s^{-1}, which is comparable to as cast devices of P3HT from chloroform.[23] However, the positive threshold voltage and high I_{OFF} are unfavorable parameters that are indicative of doping and impurities in the device (REF). This behavior may be caused by the Br moiety acting as charge traps.

A common way to improve the performance of P3HT-based FETs is by thermal annealing.[23,24] After annealing at 150°C for 1 hr, the mobility of the P3HT-Br10 device improved by over an order of magnitude to 2.7×10^{-2} cm^2 V^{-1} s^{-1}. The threshold voltage became negative, and the on/off current ratio was at a reasonable value. Annealing of the P3HT-Br10 at an elevated temperature of 150°C allowed the polymer chains to become mobile and thus induced the lamellar ordering and π-stacking of the polymer.

We were interested to probe the effect of crosslinking on the polymer FET performance. The P3HT-Br10 film was photocrosslinked by illuminating the sample with UV light (λ = 254 nm) from a low power hand-held lamp (1.9 mW cm^{-2}). After 1 hr of photocrosslinking, the FET performance of the P3HT-Br10 was tested and found to be not active. This suggests that crosslinking is disrupting the electronic and/or the structural properties of the P3HT-Br10, leading to poor FET performance. Interestingly though, we were able to recover some transistor activity by subsequently annealing the crosslinked sample. The P3HT-Br10 device that was first photocrosslinked for 1 hr and then annealed at 150°C for 1 hr showed a mobility of 2.5 x 10^{-4} cm^2 V^{-1} s^{-1}, a threshold voltage of -5V and an on/off current ratio of 7 x 10^3. However, this performance is still lower than that of the annealed device as well as the as cast device.

To study the combined effect of photocrosslinking and thermal annealing, we also tested a P3HT-Br10 device that was crosslinked and annealed at the same time. In this case, the sample was placed on a hot plate at 150°C while under UV illumination to achieve simultaneous crosslinking and annealing treatments. Figure 7.8c and d show the I-V characteristics of this device, which achieved an FET mobility of 8.5 x 10^{-3} cm^2 V^{-1} s^{-1}. It is clear that crosslinking and annealing at the same time preserved the favorable electronic and structural properties of the polymer to achieve favorable device performance.

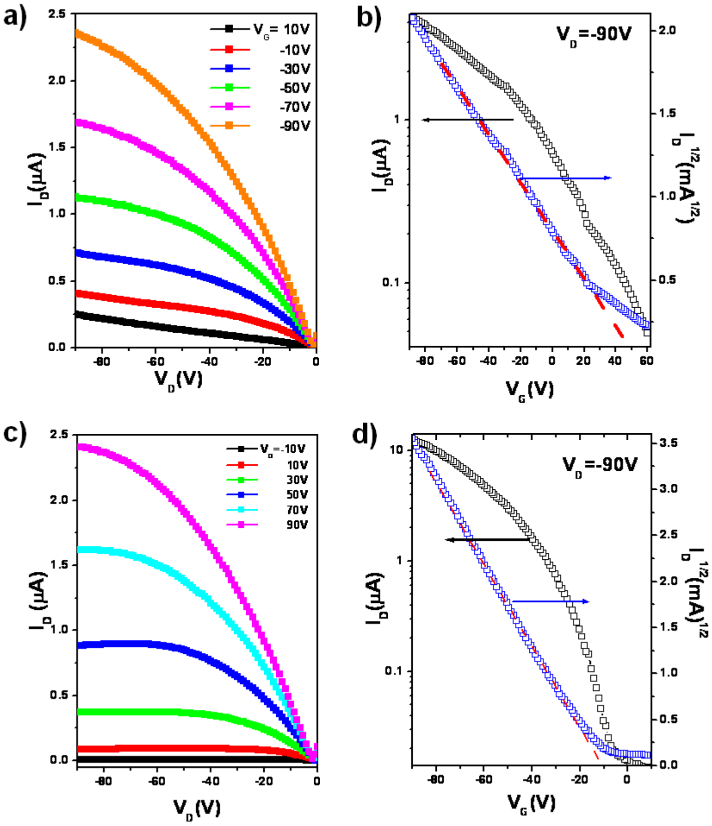

Figure 7.8 a) Output and b) transfer curves of an as cast P3HT-Br10 FET device. c) Output and d) transfer curves of a P3HT-Br10 FET device that has been crosslinked and annealed simultaneously for 1 hr.

To investigate the correlation between charge mobility and microstructural order in the polymer thin films, we performed in-depth X-ray diffraction analysis to quantitatively compare the degree of crystallinity of the P3HT-Br10 samples processed under different conditions. We followed the method developed by Baker et al.[14] for quantifying crystallographic information for textured polymer thin films using a synchrotron radiation light source and an area detector. Due to the anisotropic distribution of crystallite orientation in these semicrystalline polymer thin films, we need to use pole figures to fully capture all the crystallite orientations in order to perform valid quantitative comparisons.[25,26] A pole figure is a plot that shows the orientation distribution of a particular Bragg reflection and provides information on the texture of the thin film.

The X-ray diffraction samples were prepared under identical conditions as the FET devices. Thin films of P3HT-Br10 (~100 nm) were spun coat from chloroform onto OTS-treated Si/SiO$_2$ substrates and subjected to the same five processing conditions mentioned above: 1. As cast, 2. Crosslinked (XL), 3. Crosslinked and then annealed (XL and then AN), 4. Crosslinked and annealed at the same time (XL and AN together), 5. Annealed (AN). To obtain the complete pole figure, we had to collect two sets of data, one in the grazing incidence geometry (where the sample is horizontal) and the other in the local-specular geometry (where the sample is tilted to satisfy the specular geometry for that particular Bragg reflection).[14] For quantitative comparisons among all the samples, the data was corrected for the distortion by the area detector, polarization, X-ray absorption, beam intensity, scan duration and sample thickness.

For the grazing incidence measurement, the angle of incidence (~0.12^o) was carefully chosen to allow for complete penetration of the X-rays into the polymer film but not into the Si substrate. Figure 7.9 shows the 2D grazing incidence X-ray scattering (GIXS) patterns of the as cast P3HT-Br10 film and the sample that was crosslinked and annealed simultaneously. The 2D image map can be divided into a component in the plane of the substrate (q_x) and a component perpendicular to the substrate (q_z). Similar to P3HT,[27] P3HT-Br10 samples displayed three strong (*h*00) peaks, and they exhibited obvious anisotropic orientation with the strongest peak intensity in the out-of-plane (q_z) direction. The (010) peak at q = 1.7 Å^{-1} (d = 3.8 Å) is also present in both samples and corresponds to the π-stacking distance between polymer chains. Qualitatively speaking, the two samples essentially showed the same GIXS pattern. In fact, this was true for all five samples, which showed almost identical GIXS patterns despite being subjected to different processing conditions (see SI). This means that neither crosslinking nor annealing changed the overall crystallite orientation and lattice spacings of the P3HT-Br10 thin film.

However, simply comparing the grazing incidence patterns did not allow us to draw any conclusions regarding the relative crystallinity of the P3HT-Br10 samples processed under the five different conditions. This was because of the large beam footprint as well as the inaccuracy of the grazing incidence measurement near the pole (where $q_x \sim 0$ Å^{-1}).[14] It was necessary to collect additional diffraction data at the local-specular geometry, where the sample is tilted so that the incidence angle satisfies the Bragg condition of a specific diffraction peak. The specular diffraction measurement was performed at both the (100) Bragg reflection and the (200) Bragg reflection for each sample. The original rectangular detector coordinates (x, z) were converted to polar coordinates (r, χ) so that we could extract the signal from an annular region for a selected Bragg ring. For the (100) reflection, the region selected was from r = 0.2 Å^{-1} to r = 0.5 Å^{-1}. For the (200) reflection, we integrated from r = 0.7 Å^{-1} to r = 0.85 Å^{-1}. For each Bragg peak, we had two I(χ) plots, one from the grazing incidence measurement and one from the local-specular measurement. The two I(χ) figures were scaled and merged at χ ~10°, giving the final pole figure as shown in

. The intensity near the pole (χ < 10°, i.e. in the out-of-plane direction) came from data collected at the local-specular geometry whereas the intensity at χ > 10° corresponded to data from the grazing incidence measurement.

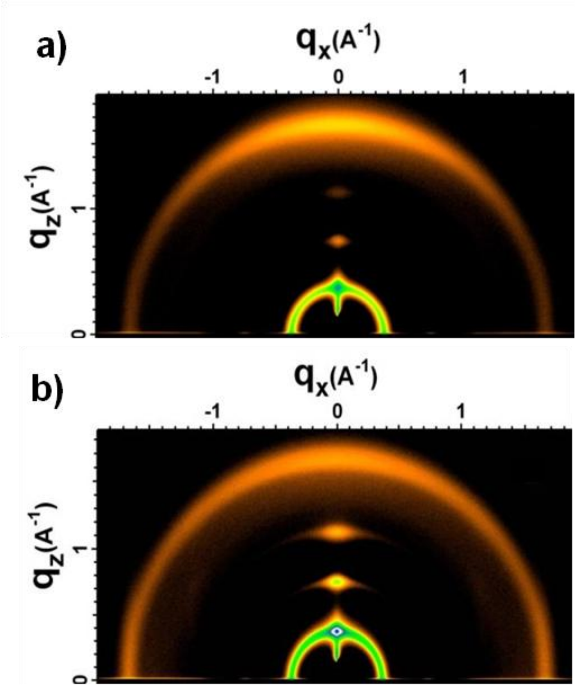

Figure 7.9 2D grazing incidence X-ray scattering patterns of a) as cast and b) crosslinked and annealed P3HT-Br10 films.

shows the pole figures for the (100) and (200) Bragg reflections of the as cast sample and the sample that was crosslinked and annealed simultaneously. The intensity of the x-ray diffraction signal was plotted in a semi-log scale against χ, which was the degree of orientation of the crystallite. First, we observed that the χ dependence of the two samples were very similar. The χ dependence was also consistent across the (100) and the (200) Bragg reflections. For both samples and for both Bragg reflections examined, the signal was strongest near the pole where χ was small, which indicated that most of the crystalline polymer chains were oriented out-of-plane, perpendicular to the substrate. In the region where χ > 15°, the signal became exponentially smaller and the χ dependence was much weaker. Second, comparing

a and 7.4b, it is clear that the signal-to-noise ratio was higher for the (100) Bragg reflection. However, we note that the pole figure of the (200) Bragg reflection is generally more accurate because of its distance from the direct beam. The intensity of the (100) Bragg peak was distorted by reflection from the beam stop (see Figure 7.9), which was difficult to subtract. For this reason, we chose to use the pole figures from the (200) Bragg reflections of the five samples for quantitative comparison. Nonetheless, the data from the (100) Bragg peak showed a similar trend in all the samples, and the comparison using the (100) reflection is included in the supporting information.

The intensity of the pole figures in

had been corrected for sample thickness, beam intensity, and other distortions. Therefore, we could directly compare the intensity of the signals of the two plots. The crosslinked and annealed sample had much higher diffraction intensity across all χ, which meant that this sample had a higher degree of crystallinity than the as cast sample. To obtain the relative degree of crystallinity for each sample, we integrated the area under the curve of the pole figure from $\chi = 0^\circ$ to $\chi = 90^\circ$. Figure 7.11 shows the results of the integration of the pole figures from the five samples. For comparative reasons, we also illustrate in Figure 7.11 the corresponding FET mobility of each sample. This master graph shows a clear correlation between the charge mobility and relative crystallinity of the samples, where a higher degree of crystallinity led to better FET performance. Processing conditions had a huge effect on the microstructural order of the thin film, which in turn determined the charge carrier mobility of the sample.

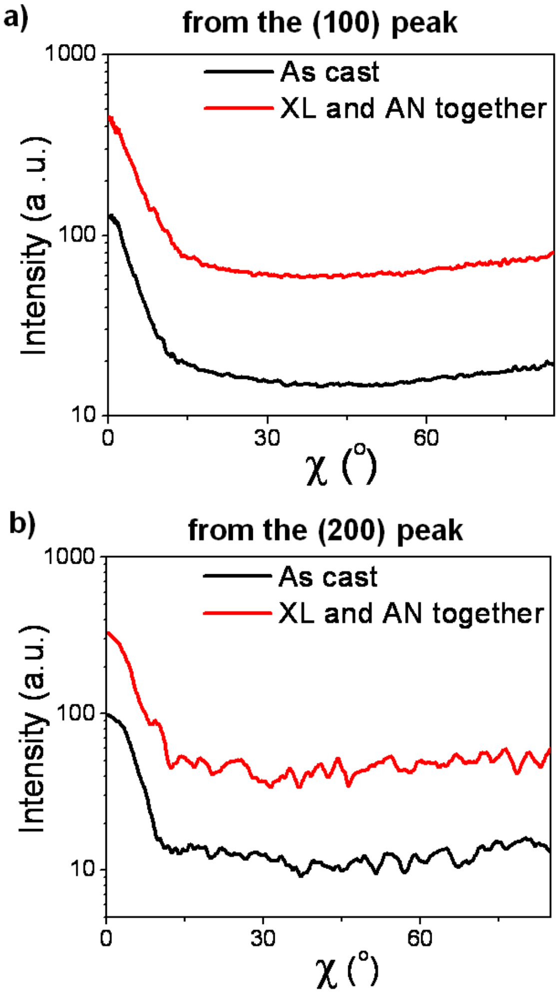

Figure 7.10 Comparing pole figures of the as cast P3HT-Br10 sample and the sample that was crosslinked and annealed at the same time (XL = crosslinked, AN = annealed). a) Pole figure from the (100) peak. b) Pole figure from the (200) peak.

These results suggest that crosslinking did not disrupt the overall degree of crystallinity of the polymer film, as the crosslinked sample had a similar DOC to the as cast sample. The lack of FET activity may be due to the generation of Br radicals during crosslinking which could have damaged the electronic property of the polymer. As mentioned above, some FET activity could be recovered by subsequent thermal annealing of the crosslinked sample. However, there was little change in crystallinity upon annealing a crosslinked sample. This was most likely because the 3D structure of the P3HT-Br10 was locked in during crosslinking, and annealing the sample above the glass transition temperature of the polymer did not induce the formation of crystalline domains. We also attempted to first anneal the sample and then photo-crosslink. However, this procedure did not lead to effective crosslinking of polymer chains. In other words, crosslinking had to be performed before the polymer chains were organized into regular crystal structures. This finding has implications on the crosslinking mechanism of this material, which is currently under investigation.

To circumvent the problem of locking in the 3D morphology too early and to achieve effective crosslinking, we attempted to simultaneously crosslink and anneal the P3HT-Br10 film. This processing condition led to effective crosslinking of the polymer film and afforded FET devices that were better than as cast devices but not as good as annealed devices. More importantly, this trend was correlated well with our crystallinity measurements, where the sample that was crosslinked and annealed together possessed a degree of crystallinity that was in between that of the as cast sample and the annealed sample. Therefore, this new processing condition preserved a high degree of crystallinity in the thin film and was an effective way to achieve high FET mobility.

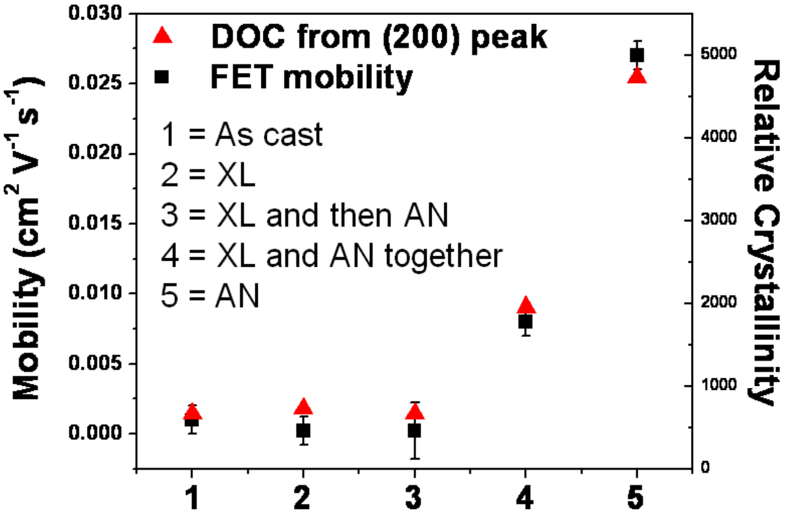

Figure 7.11 FET mobility of P3HT-Br10 thin films processed under five different conditions and their relative degree of crystallinity (DOC) obtained from integrating their corresponding pole figures from their (200) Bragg peak.

7.3 Conclusions

In conclusion, we investigated the effect of thermal annealing and UV-initiated photocrosslinking on the FET performance and microstructural order of the photocrosslinkable P3HT-Br10 material. Crosslinking did not disrupt the overall crystallinity of the polymer thin film, but the photocrosslinking process likely damaged the electronic integrity of the material, leading to an inactive FET device. Annealing after crosslinking partially recovered some FET activity but did not affect the microstructural order of the polymer film since the 3D morphology had been locked in during the first crosslinking step. In addition, we discovered that annealing and crosslinking simultaneously was a successful method to preserve polymer crystallinity while also achieving effective crosslinking. Using a newly developed quantitative X-ray analysis technique, our study established a clear correlation between FET charge mobility and thin film crystallinity.

7.4 Experimental

7.4.1 Synthetic Details

All chemicals were purchased from Aldrich and used without further purification unless stated otherwise. All reactions were performed under nitrogen in glassware that had been flame dried under vacuum. All compounds were characterized by ^{1}H NMR (400 MHz) and ^{13}C NMR (75 MHz) on a Bruker AVB 400 or AVQ 400. High-resolution mass spectra and elemental analysis (CHNS) was performed at the University of California, Berkeley Department of chemistry analytical services. Polymer ^{1}H NMR (500 MHz) were obtained on Bruker DRX 500. For polymer molecular weight determination, polymer samples were dissolved in HPLC grade dichlorobenzene at a concentration of 1 mg/ml and stirred overnight at room temperature prior to filtering through a 0.2 μm PVDF filter and SEC was performed using HPLC grade dichlorobenzene at a flow rate of 0.8 μL/min on two 300 x 8 mm linear S SDV, 5 micron columns (Polymer Standards Services, USA Inc.) at 70 ºC using a Waters (Milford, MA) 2690 separation module and a Waters 486 Tunable Absorption Detector monitored at 350 nm. The instrument was calibrated vs. polystyrene standards (1,050 – 135,000 g/mol) and data was analyzed using Millenium 3.2 software.

7.4.2 Thin Film Characterization

Grazing-Incidence X-ray Scattering (GIXS): GIXS experiments were conducted at the Stanford Synchrotron Radiation Laboratory on beamline 11-3. The sample is irradiated at a fixed incident angle on the order of a tenth of a degree and the GIXS patterns are recorded with a 2-D image detector (MAR345 image plate detector). GIXS patterns were recorded with an X-ray energy of 12.72 keV (λ=0.975Å). To maximize the intensity from polymer sample, the incident angle (0.1^o - 0.12^o) was carefully chosen so that the X-ray beam penetrates the polymer sample completely but not the silicon substrate. Typical exposure times were 90-180 sec. To produce identical surface condition as samples for FET device fabrication, the SiO_2/Si substrate was treated with OTS before spin coating the polymer. The GIXS samples were prepared by spin-coating the same solutions used for making FET devices onto silicon substrates at 1200RPM for 60s. The substrates were placed directly on top of a hot plate under Nitrogen for thermal annealing and they were placed under a hand-held UV lamp for photocrosslinking.

Atomic force microscopy (AFM): AFM was performed to study the surface morphology of the P3HT-Br10 films. Topographical and phase images were obtained concurrently using a Veeco Multimode V AFM in tapping mode using RTESP tips.

7.4.3 Additional Figures

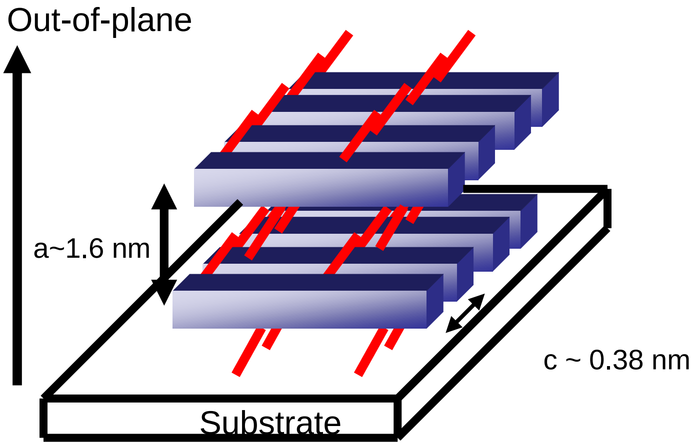

Figure 7.6. Schematic of the organization of P3HT-Br10 chains relative to the substrate and domain spacing.

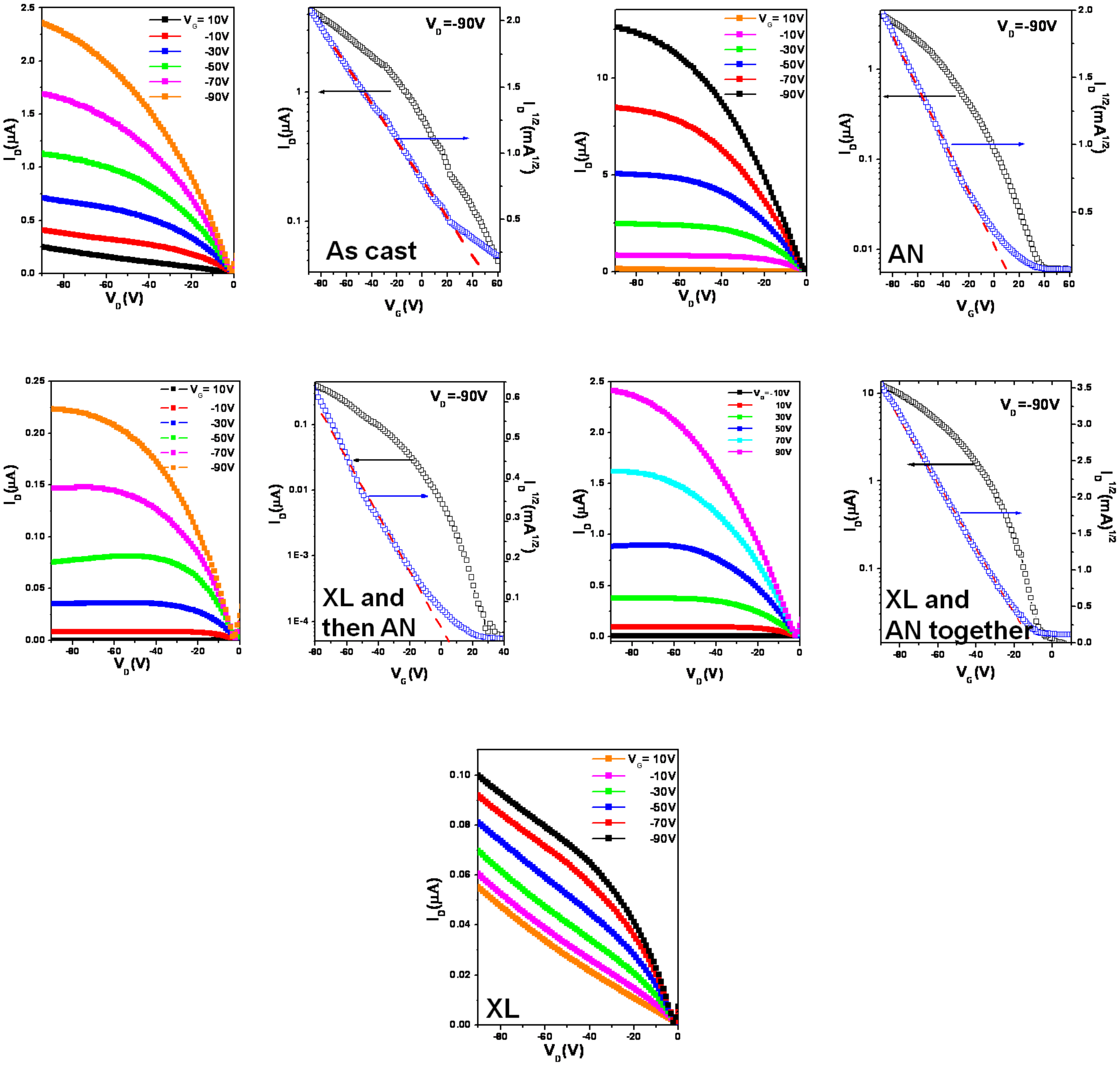

Figure 7.7. Output and transfer curves of P3HT-Br10 FET devices processed under 5 different conditions (XL = crosslinked, AN = annealed).

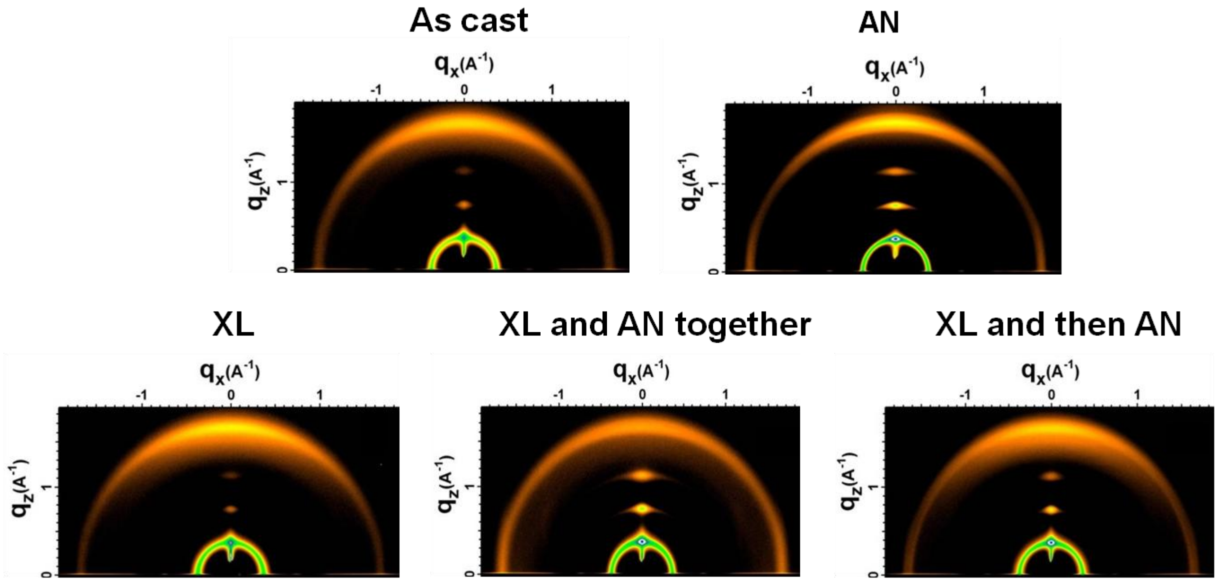

Figure 7.8. 2D GIXS patterns of P3HT-Br10 samples processed under 5 different conditions. (XL = crosslinked, and AN = annealed)

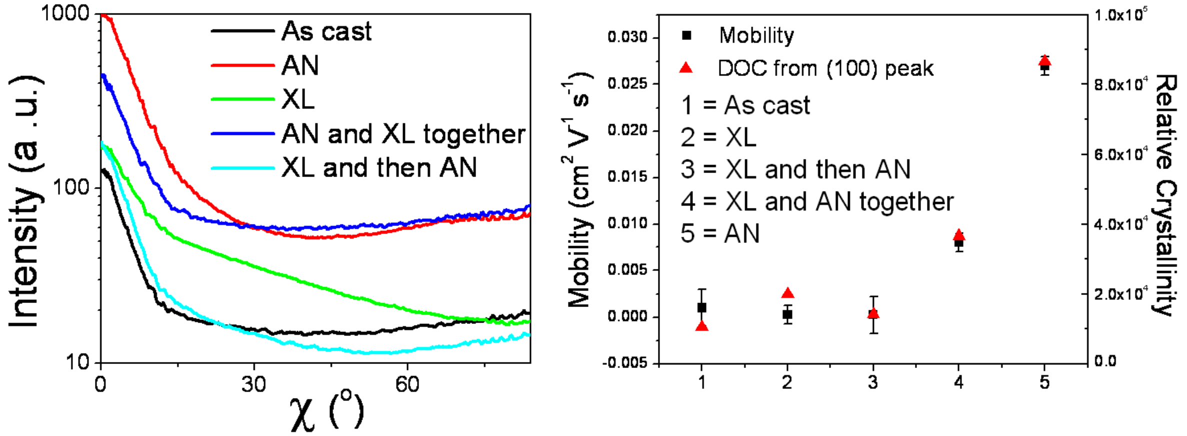

Figure 7.9. (left) Pole figures from the (100) Bragg reflection of P3HT-Br10 thin films processed under 5 different conditions ((XL = crosslinked, and AN = annealed). (right) Correlation of FET mobility and relative degree of crystallinity (DOC) estimated from integration of the pole figures on the left.

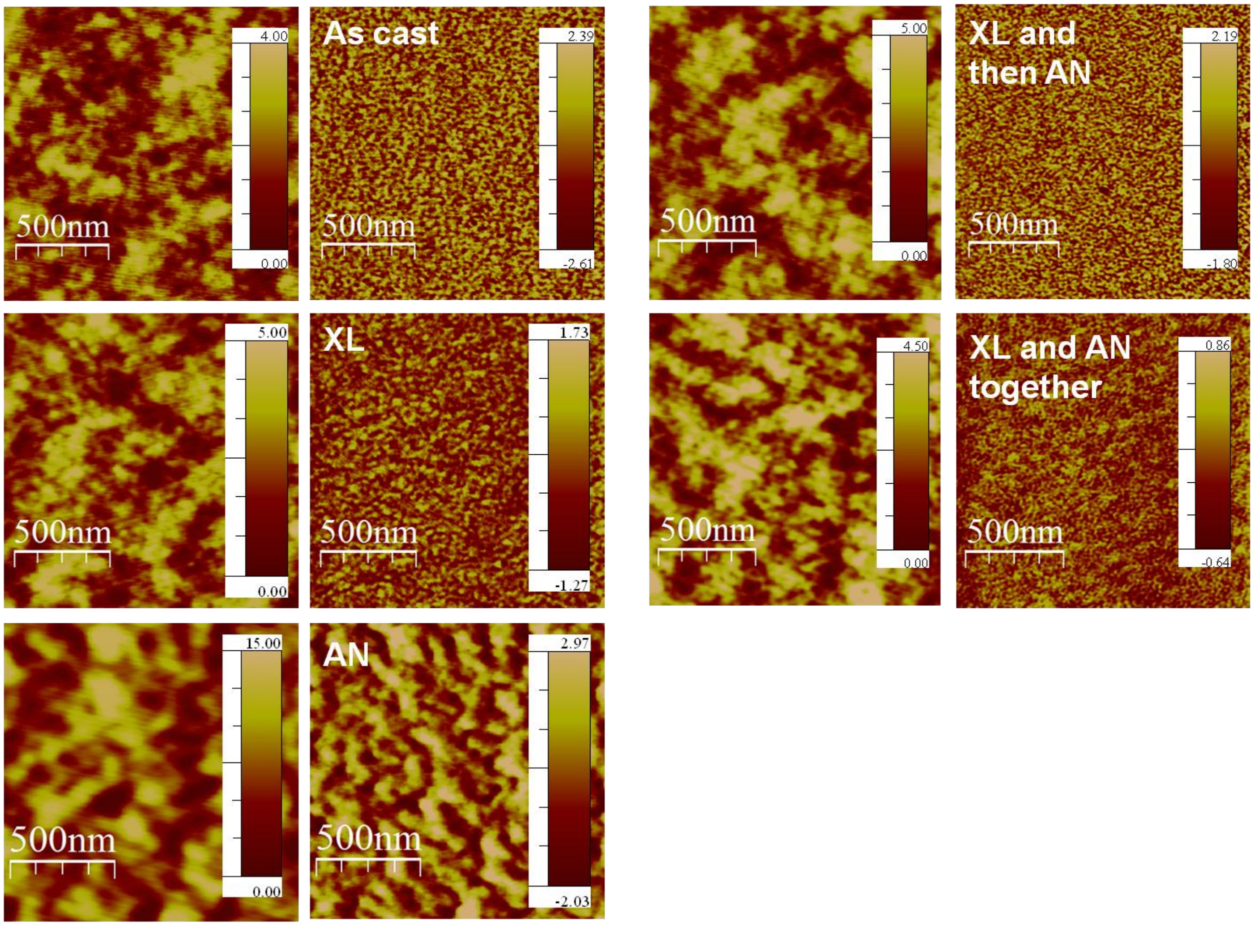

Figure 7.10. AFM images of P3HT-Br10 thin films processed under 5 different conditions. (XL = crosslinked, and AN = annealed)

7.5 References

(1) Arias, A. C.; MacKenzie, J. D.; McCulloch, I.; Rivnay, J.; Salleo, A. *Chem. Rev.* **2010**, *110*, 3-24.
(2) Gelinck, G.; Heremans, P.; Nomoto, K.; Anthopoulos, T. D. *Adv. Mater.* **2010**, *22*, 3778-3798.
(3) Salleo, A.; Kline, R. J.; DeLongchamp, D. M.; Chabinyc, M. L. *Adv. Mater.* **2010**, *22*, 3812-3838.
(4) Zhang, W. M.; Smith, J.; Watkins, S. E.; Gysel, R.; McGehee, M.; Salleo, A.; Kirkpatrick, J.; Ashraf, S.; Anthopoulos, T.; Heeney, M.; McCulloch, I. *J. Am. Chem. Soc.* **2010**, *132*, 11437-11439.
(5) McCulloch, I.; Heeney, M.; Bailey, C.; Genevicius, K.; MacDonald, I.; Shkunov, M.; Sparrowe, D.; Tierney, S.; Wagner, R.; Zhang, W.; Chabinyc, M. L.; Kline, R. J.; McGehee, M. D.; Toney, M. F. *Nat. Mater.* **2006**, *5*, 328-333.

(6) Chabinyc, M. L.; Toney, M. F.; Kline, R. J.; McCulloch, I.; Heeney, M. *J. Am. Chem. Soc.* **2007**, *129*, 3226-3237.
(7) Li, Y. N.; Singh, S. P.; Sonar, P. *Adv. Mater.* **2010**, *22*, 4862-4866.
(8) Chang, J. F.; Sun, B.; Breiby, D. W.; Nielsen, M. M.; Solling, T. I.; Giles, M.; McCulloch, I.; Sirringhaus, H. *Chem. Mat.* **2004**, *16*, 4772-4776.
(9) Rivnay, J.; Toney, M. F.; Zheng, Y.; Kauvar, I. V.; Chen, Z. H.; Wagner, V.; Facchetti, A.; Salleo, A. *Adv. Mater.* **2010**, *22*, 4359-4363.
(10) Rivnay, J.; Jimison, L. H.; Northrup, J. E.; Toney, M. F.; Noriega, R.; Lu, S. F.; Marks, T. J.; Facchetti, A.; Salleo, A. *Nat. Mater.* **2009**, *8*, 952-958.
(11) Kitamura, M.; Arakawa, Y. *Journal of Physics: Condensed Matter* **2008**, *20*, 184011.
(12) Kline, R. J.; Hudson, S. D.; Zhang, X. R.; Gundlach, D. J.; Moad, A. J.; Jurchescu, O. D.; Jackson, T. N.; Subramanian, S.; Anthony, J. E.; Toney, M. F.; Richter, L. J. *Chem. Mat.* **2011**, *23*, 1194-1203.
(13) DeLongchamp, D. M.; Kline, R. J.; Fischer, D. A.; Richter, L. J.; Toney, M. F. *Adv. Mater.* **2011**, *23*, 319-337.
(14) Baker, J. L.; Jimison, L. H.; Mannsfeld, S.; Volkman, S.; Yin, S.; Subramanian, V.; Salleo, A.; Alivisatos, A. P.; Toney, M. F. *Langmuir* **2010**, *26*, 9146-9151.
(15) Verploegen, E.; Mondal, R.; Bettinger, C. J.; Sok, S.; Toney, M. F.; Bao, Z. A. *Adv. Funct. Mater.* **2010**, *20*, 3519-3529.
(16) Kim, C.; Wang, Z. M.; Choi, H. J.; Ha, Y. G.; Facchetti, A.; Marks, T. J. *J. Am. Chem. Soc.* **2008**, *130*, 6867-6878.
(17) Cao, Q.; Xia, M. G.; Shim, M.; Rogers, J. A. *Adv. Funct. Mater.* **2006**, *16*, 2355-2362.
(18) Yoon, M. H.; Facchetti, A.; Marks, T. J. *Proc. Natl. Acad. Sci.* **2005**, *102*, 4678-4682.
(19) Liu, C.; Sirringhaus, H. *J. Appl. Phys.* **2010**, *107*.
(20) Wei, Q.; Tajima, K.; Hashimoto, K. *ACS Appl. Mater. & Interfaces* **2009**, *1*, 1865-1868.
(21) Kim, B. J.; Miyamoto, Y.; Ma, B. W.; Fréchet, J. M. J. *Adv. Funct. Mater.* **2009**, *19*, 2273-2281.
(22) Griffini, G.; Douglas, J. D.; Piliego, C.; Holcombe, T. W.; Turri, S.; Fréchet, J. M. J.; Mynar, J. L. *Adv. Mater.* **2011**, *23*, 1660-1664.
(23) Kline, R. J.; McGehee, M. D.; Kadnikova, E. N.; Liu, J.; Fréchet, J. M. J.; Toney, M. F. *Macromolecules* **2005**, *38*, 3312-3319.
(24) Zen, A.; Pflaum, J.; Hirschmann, S.; Zhuang, W.; Jaiser, F.; Asawapirom, U.; Rabe, J. P.; Scherf, U.; Neher, D. *Adv. Funct. Mater.* **2004**, *14*, 757-764.
(25) Schwartz, M. *J. Appl. Phys.* **1955**, *26*, 1507-1513.
(26) Norton, J. T. *J. Appl. Phys.* **1948**, *19*, 1176-1178.
(27) Woo, C. H.; Thompson, B. C.; Kim, B. J.; Toney, M. F.; Fréchet, J. M. J. *J. Am. Chem. Soc.* **2008**, *130*, 16324-16329.